Influence of Thermodynamic Property Perturbations on Nozzle Design and Non-Ideal Compressible Flow Phenomena

Siddharth Iyer

Master of Science Thesis
Report Number: 2694

Delft University of Technology

Mechanical, Maritime and Materials Engineering

Influence of Thermodynamic Property Perturbations on Nozzle Design and Non-Ideal Compressible Flow Phenomena

Master of Science Thesis

For the degree of Master of Science in Mechanical Engineering: Sustainable Process and Energy Technology at Delft University of Technology

Siddharth Iyer

September 23, 2015

Faculty of Mechanical, Maritime and Maritime Engineering (3ME) · Delft University of Technology

The work in this thesis was supported by the Propulsion and Power group at the TU Delft Aerospace Department. Their cooperation is hereby gratefully acknowledged.

Delft University of Technology
Department of
Energy Technology

The undersigned hereby certify that they have read and recommend to the Faculty of Mechanical, Maritime and Maritime Engineering (3ME) for acceptance a thesis entitled

Influence of Thermodynamic Property Perturbations on Nozzle Design and Non-Ideal Compressible Flow Phenomena

by

Siddharth Iyer

in partial fulfillment of the requirements for the degree of

Master of Science Mechanical Engineering: Sustainable Process and Energy Technology

Dated: September 23, 2015

Supervisor(s):

Dr. Matteo Pini

Ir. Adam Joseph Head

Ir. Salvatore Vitale

Reader(s):

Prof. Dr. Bendiks Jan Boersma

Dr. Rene Pecnik

Abstract

In recent years, the scientific community has shown increased interest in the use of uncertainty quantification techniques for complex thermodynamic systems. One such complex system is the Organic Rankine Cycle (ORC) power system for which a turbine is often the prime mover. These systems operate in a region close to the critical conditions of the fluid which makes their thermodynamic behaviour complex. Additionally, the organic fluids are commonly characterized by low speed of sound which induces compressibility effects such as shock waves as the fluids expand through a turbine. In order to design optimum turbine blades and to accurately estimate the performance of these machines, it is imperative to gain a better understanding of these compressible flow effects. The flow through a de-Laval nozzle is a simple representation of flow through a turbine. Thus the objective of this research is to gain an improved understanding of the influence of uncertainty in the thermodynamic properties on nozzle design and compressible flow phenomena. The study is realized by performing an uncertainty quantification analysis using DAKOTA which is coupled with Matlab.

Quite often a model such as a wedge can be placed in the nozzle to induce the required fluid dynamic phenomena. In this study, these phenomena are characterized in terms of the angle and intensity of the shock waves generated. An Euler shock wave simulator code is used to determine the shock wave angle and shock wave intensity. Two set of simulations are performed depending on the position of the wedge in the de-Laval nozzle. In the first set of simulations, the wedge is placed at the exit of the nozzle in a region which predominantly shows ideal gas behaviour. In the second set of simulations, the wedge is placed at 7.8 mm from the nozzle throat to capture the influence of real gas effects on the computed flow dynamic quantities. In addition, the deviation in the nozzle profile due to the uncertainties in the input parameters is also estimated. The two sets are further subdivided into two cases depending on the choice of the uncertain input variables. In the first case the fluid dependant parameters and the geometric parameters are considered to be uncertain. The fluid dependant parameters are the critical temperature, critical pressure, acentric factor, κ_1 parameter used in the iPRSV equation of state and the four coefficients of the ideal gas isobaric heat capacity of MM (hexamethyldisiloxane) while the geometric parameter considered is the wedge angle of the geometry. In the second case the total pressure and total temperature which are the operating conditions are also uncertain in addition to the fluid dependant and geometric

parameters.

The results of the two set of simulations are presented in terms of deviation in the shock wave properties from the nominal. For both the cases with the wedge placed at the exit of the nozzle, the shock wave angle and the intensity is found to vary by 0.17% and 0.06% respectively. With the wedge near the throat, for the first case the deviations are computed as 2.2% and 2.7% in the angle and intensity of the shock waves respectively while for the second case the properties of the shock wave vary by 2.6% and 3.1% respectively. In addition the average deviation in the nozzle profile for the both the cases is found to be 0.29 mm. These results indicate that in the real gas region, the effect of the uncertainty in the input parameters is amplified which causes a large deviation in the compressibility effects.

The deviation in the shock wave angle is verified by performing CFD simulations in SU2 for the cases that yield maximum deviation. The results are found to be in good agreement with an average deviation of 0.33% with the wedge at the exit and 1.2% for the wedge at 7.8 mm from the throat.

Finally the analysis performed on the nozzle is extended to a radial outflow turbine. Nine cases are simulated by varying the critical temperature and pressure of MM to estimate the deviation in the static enthalpy loss. The simulation results indicate a large deviation in the loss which denotes that the critical point values have a significant effect on the losses in an ORC turbine. The results obtained from this study thus provide a deeper insight into the thermodynamic properties that influence the behaviour of shock waves and nozzle design.

Acknowledgments

During the past nine months, I had the opportunity to work with a lot of people who have been instrumental in shaping this work. I would like to take this opportunity to thank all of them.

First of all, I owe my deepest gratitude to my daily supervisor Ir. Adam Joseph Head for giving me the opportunity to work on this thesis topic. I sincerely appreciate your enthusiasm and the time you devoted to discuss all my doubts throughout this study even though you were busy with your Ph.D. duties. Your constant support, help and evaluation of my work and this report have greatly helped me throughout this study.

I would also like to thank my supervisor Dr. Matteo Pini for his guidance. I am grateful to have you as my supervisor. Your critical feedback and constant encouragement was a driving force in the successful completion of this work.

Furthermore, I try appreciate the help of Ir. Salvatore Vitale, Ir. Sebastian Bahamonde Noriega, Ir. Lucia Azzini , Ir. Antonio Rubino, Dr. Carlo De Servi, Ir. Teunis van der Stelt and Tony Chew for their help throughout my master thesis. I am also grateful to my examination committee for their time devoted in reviewing and evaluating this content.

Special thanks to all my friends here in Delft for their constant support, enthusiasm and help during this study. Finally, I would like to thank my parents and my brother for their selfless love and motivation during this long and hard final phase of my master's degree.

Delft, University of Technology
September 23, 2015

Siddharth Iyer

Table of Contents

List of Figures

List of Tables

"Science is founded on uncertainty. Each time we learn something new and surprising, the astonishment comes with the realization that we were wrong before. " — *Lewis Thomas*

Nomenclature

Latin Symbols	**Description**	**Units**
a	Speed of sound	m/s
A	Area	m^2
B	Body force per unit mass	N/kg
C_{P}	Specific heat of gas at constant pressure	J/kg.K
C_{V}	Specific heat of gas at constant volume	J/kg.K
F	Force	N
G	Gibbs energy	J
H	Enthalpy	J
h	Specific enthalpy	J/kg
$\dot{m}$	Mass flow rate	kg/s
M	Mach number	-
p	Pressure	N/m^2
r	Radius	m
R	Specific gas constant	J/kg.K
T	Temperature	K
S	Entropy	J/K
s	Specific entropy	J/kg.K
U	Internal energy	J
u	Velocity	m/s
v	Specific volume	m^3/kg
$\dot{W}$	Work	Nm/s
$\mathscr{V}$	Volume	m^3
W	Relative velocity	m/s
z	Height	m
Z	Compressibility factor	-

Greek Symbols		
β	Shock wave angle	$^\circ$
γ	Ratio of specific heats	-
δ	Shock wave intensity	-
θ	Flow turning angle	$^\circ$
ρ	Density	kg/m^3

ζ	Static enthalpy loss	-
μ	Mach angle	$^{\circ}$
μ_{dyn}	Dynamic viscosity	$N.s/m^2$
μ_{tur}	Turbulent viscosity	$N.s/m^2$
Ω	Rotational speed	rad/s
ω	Acentric factor	-

Subscripts

1	Upstream of shock wave
2	Downstream of shock wave
d	Departure function
CR	Critical point value
N	Normal
s	Isentropic
T	Tangential
dyn	Dynamic
tur	Turbulent

Superscripts

r	Reduced quantity
ig	Ideal gas

Acronyms

ANOVA	Analysis of Variance
CFL	Courant-Friedrichs-Lewy
D_4	Octamethylcyclotetrasiloxane
iPRSV	Improved Peng Robinson Stryjek Vera
MM	Hexamethyldisiloxane
MDM	Octamethyltrisiloxane
PP2	Perfluoromethylcyclohexane
PP80	Perfluoro-2-methyl-3-ethylpentane
PP90	Perfluoro-2,4-dimethyl-3-ethylpentane
ORC	Organic Rankine Cycle
ORCHID	Organic Rankine Cycle Hybrid Integrated Device
EoS	Equation of State
CFD	Computational Fluid Dynamics
MoC	Method of Characteristics
DAKOTA	Design Analysis Kit for Optimization and Terascale Applications
NICF	Non-Ideal Compressible Flows
PDE	Partial Differential Equation
PIV	Particle Image Velocimetry
RANS	Reynolds Averaged Navier Stokes
SU2	Stanford University Unstructured
UQ	Uncertainty Quantification
UMG2	Unstructured Mesh Generator 2-dimensional
VBD	Variance-based Decomposition

Chapter 1

Introduction

1-1 Background

In recent years, the scientific community has shown increased interest in the application of uncertainty analysis for complex thermodynamic systems [9]. Input parameters in engineering systems are always subject to some uncertainty. Until a few years ago, these uncertainties were neglected, which resulted in single deterministic simulations considering the parameters to be fixed and unmodifiable. Given the number of uncertainties affecting engineering systems, such deterministic analysis may lead to good approximations of the system behaviour at nominal conditions but poor approximation at other conditions. However the recent development of advanced computers with high computing power has led to an increase in the application of stochastic approaches in complex systems. Such approaches yield a better representation of the behaviour of a system that is closer to reality.

One such complex system is the Organic Rankine Cycle (ORC) technology. ORC power systems are a viable technology for the conversion of waste heat and other energy sources (solar, geothermal) in the small-to-medium power range (100 kWe to a few MWe) [11], [12]. The design of highly efficient ORC turbines is of paramount importance for the further development of this technology. These turbines typically operate in a complex thermodynamic region where the properties of the fluid show non-ideal behaviour [13]. In addition, the fluids undergo supersonic expansion which induces compressible effects such as shock waves. This makes the design and performance estimation of these machines challenging. To model such complex non-ideal compressible flow phenomena where the properties of the fluids are uncertain, stochastic approaches are needed. Such analyses could be first used in designing a robust nozzle as the flow through a nozzle depicts the flow through a turbine. Consequently, the analyses could be extended to designing complex geometries such as turbine blades.

To study such compressible flow affects, a robust nozzle is designed shown in Figure 1-1 for use in an experimental facility being constructed at the Delft University of Technology [1]. Figure 1-2 shows shock waves generated at the tip of a wedge placed in a nozzle.

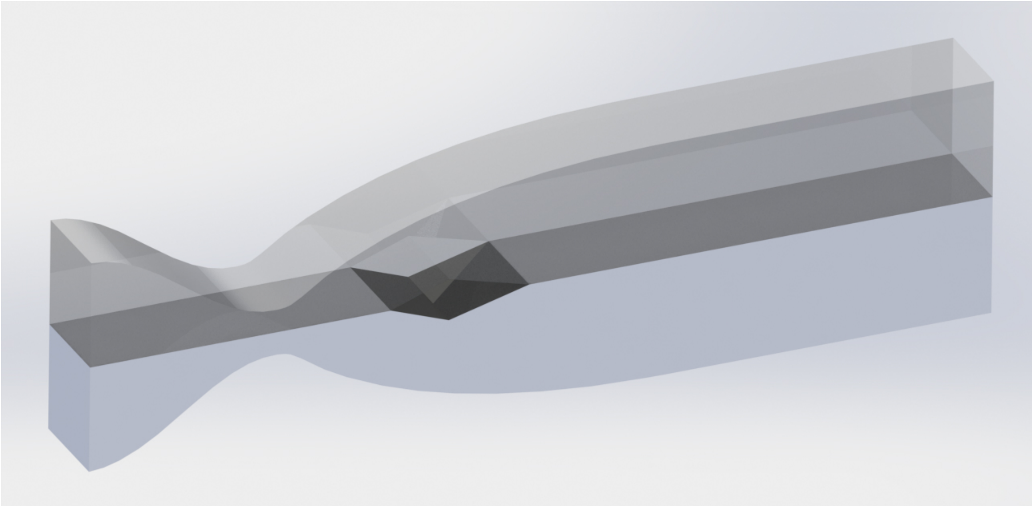

Figure 1-1: Robust nozzle designed for use in the ORCHID test facility [1].

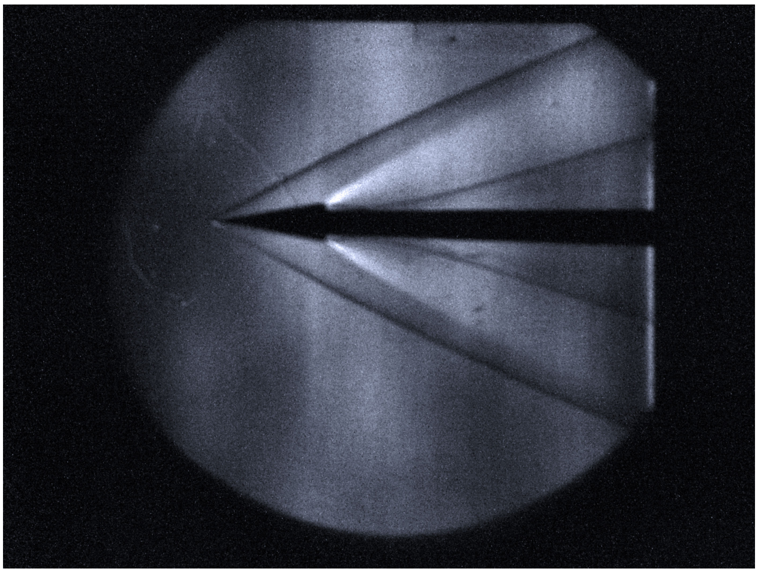

Figure 1-2: Schlieren image of shock wave formed at the tip of a wedge in a supersonic wind tunnel.

1-2 Motivation

The need for small scale power generation has led to the development of mini and micro gas turbines. Though they have potential advantages, particularly for distributed power generation, there are certain technical barriers in the use of this technology. Scaling down of gas turbines causes large changes in Reynolds number and the geometrical restrictions related to manufacturing of the miniaturized components becomes a concern [14]. The use of organic fluids instead of a mixture of air and fuel in turbines adds to the challenge. The foremost difficulty in miniaturization of ORC power generation systems is the design of the turbine. The turbine is the prime mover in an ORC system and hence an efficient design with minimal losses is imperative. Efficient designs are hindered primarily because of a lack of knowledge in the behaviour of non ideal organic fluids. The use of these fluids leads to unique turbine configurations which are characterized by supersonic flows which consequently lead to strong shocks [11]. Shock waves generate entropy and hence cause a reduction in the efficiency. Though shock waves are unavoidable due to the highly supersonic nature of flow, a better understanding of its fundamental behaviour can lead to optimum design of blades and thus accurate estimation of the performance of these turbines.

A major difficulty in the improvement of ORC turbines is due to their operation close to the critical conditions in the so called dense gas regime, where the prediction of the flow behaviour requires complex thermodynamic models [15]. The properties of the fluid undergo rapid changes in this region which makes it complicated to estimate the performance of these machines. In addition, the thermodynamic models used to estimate their performance are based on set critical point values obtained from experiments. However, experiments are always associated with uncertainties. Thus to provide an accurate estimation of the performance of ORC systems, it is necessary to take these uncertainties into account. Keeping this in mind the primary focus of the current work is to provide a better understanding of the effect of thermodynamic parameters on the behaviour of shock waves and nozzle design.

The flow in a turbine blade passage can be effectively represented by flow through a converging-diverging nozzle. Thus, the design of a nozzle would be the first step in designing an optimum blade shape for a turbine. Nozzle designs are commonly based on analytical methods, such as the Method of Characteristics (MoC) which is coupled to a thermodynamic model. Therefore, in designing a nozzle, the uncertainties in the parameters of the thermodynamic model have to be taken into account. Thus this study aims at quantifying the deviations in the nozzle profile due to uncertain thermodynamic parameters which would lead to a robust nozzle design. This nozzle design could be a basis for the design of turbine blades having minimum losses due to shock waves thus ensuring maximum efficiency of ORC systems.

An uncertainty quantification study on the behaviour of organic fluids due to thermodynamic property perturbations provides an estimate of the deviation in the flow dynamic quantities. Additionally, a sensitivity analysis study presents the dominant parameters that influence these quantities. This information could be useful in suggesting improvements to the existing thermodynamic models. Moreover, the results from this study could be used in conjunction with the results obtained from experiments which would provide useful information on Non-Ideal Compressible Flow (NICF) effects to the scientific community.

1-3 Scope and Objectives

As introduced in Section 1-2, the performance of a turbine is affected by the generation of shock waves. An effective way of studying the fluid dynamic behaviour of these waves is to generate them in a nozzle as the flow through a converging-diverging nozzle is a simple representation of the flow in a turbine passage. Therefore, this study deals with the inviscid flow of fluid in a nozzle and characterizes the compressible flow phenomena in terms of the angle and intensity of the shock waves generated.

The thermodynamic properties used to calculate the extent of these compressible flow phenomena are obtained from a software for the computation of thermodynamic properties of fluids [16]. The software is a thermodynamic library that employs different equation of states (EoS) to compute the thermodynamic and transport properties of fluids. The StanMix model which uses the improved Peng-Robison Stryjek Vera (iPRSV) EoS is chosen as the preferred library to compute the thermodynamic properties. To study the influence of thermodynamic property perturbations on nozzle design and NICF Phenomena, an *Uncertainty Quantification (UQ)* study is performed using DAKOTA (see Ref. [17]). The chosen uncertain input parameters for this study are classified into three categories: *fluid dependant parameters*, *geometric parameter* and the *operating conditions*. The *fluid dependant parameters* are the critical temperature and critical pressure, the acentric factor, κ_1 term used in the iPRSV EoS and the coefficients of the ideal gas isobaric heat capacity. The *geometric parameter* considered is the wedge angle of the geometry and the *operating conditions* include the inlet total pressure and temperature of the test set-up. Samples of these parameters are generated using the Monte-Carlo and Latin Hypercube sampling approaches. The analysis is performed at two locations in a nozzle: at the exit and at a distance of 7.8 mm from the throat. Moreover, the Mach number in front of the shock wave is maintained constant to effectively simulate the deviations in the shock wave characteristics with varying input parameters. A detailed description of the analysis performed is provided in Chapter 3.

The StanMix model is coupled with a Computational Fluid Dynamic (CFD) software tool SU2 to verify results from the UQ analysis and to estimate the range of fluid dynamic losses in a turbine due to uncertainties in the critical point parameters of the chosen organic fluid. The CFD analysis for the turbine is performed using the $k - \omega - SST$ turbulence model. This high fidelity analysis is limited to only the cases which yield maximum and minimum uncertainties in the shock wave angle. Performing a detailed UQ analysis with CFD is out of scope of this work.

Within this scope of this study, the following research questions will be addressed:

- How do the uncertainties in the fluid dependant thermodynamic parameters, geometric parameter and operating conditions affect the compressible flow phenomena in a de-Laval nozzle?
- What are the profile variations in the de-Laval nozzle due to uncertainties in the fluid dependant thermodynamic parameters and operating conditions?
- Does the uncertainty in the critical properties of the fluid affect the flow dynamic losses in a radial outflow turbine?

1-4 Literature Review

This section reviews the research that has been conducted on quantifying thermodynamic perturbations and their influence on compressible flows and nozzle design.

Guardone et al. [15] studied the influence of molecular complexity on the design of the diverging portion of a supersonic nozzle operating in the dense gas region. The study was part of the Test Rig for Organic Vapours (TROVA) facility which was built at Politecnico di Milano, Italy to investigate the effects of different organic fluids on the performance of ORC turbines [15]. The TROVA test set-up is a batch vapour tunnel facility with a de-Laval nozzle as the primary test section. The nozzle profiles were generated using a standard method of characteristics approach. Profiles developed using several fluids at the same operating conditions, belonging to the class of linear and cyclic siloxanes such as: MM, MDM, D_4, D_5, D_6, and refrigerant R245fa, toulene and ammonia were studied. The first part of the study focused on the effect of the chosen EoS on the nozzle design. Profiles were generated for the fluid MDM using a multi-parameter thermodynamic model and using a perfect ideal gas model. The results showed that the ideal gas model significantly under-estimated the dimensions of the nozzle. This is because the ideal gas model predicts a higher value of the pressure and Mach number gradient. Thus a smaller nozzle length is sufficient to obtain the desired Mach number at the exit. The second part of the study dealt with the influence of molecular complexity on the nozzle profile. The molecular complexity is associated with the fundamental derivative of gas dynamics which relates the speed of sound and density in isentropic conditions. Fluids with lower value of fundamental derivative of gas dynamics have higher molecular complexity. Results from the study indicate that molecular complexity is directly proportional to the length and the exit area of the nozzle.

Cinnella et al. [9] performed an UQ study of compressible flows with complex thermodynamic behaviour. A chaos collocation method was used to study the effect of uncertainties in the parameters of the thermodynamic models on the results obtained from CFD simulations of organic fluids in the dense gas region. Three thermodynamic models, namely: the Redlich-Kwong-Soave (RKS) EoS, Peng-Robinson-Stryjek-Vera (PRSV) cubic EoS and five virial expansion term Martin-Hou (MAH) equation were considered for the study. The accentric factor, reduced ideal-gas constant volume specific heat at the critical temperature and an exponent used in calculating the ideal gas specific heat at constant volume are considered to be the uncertain input parameters for the RKS and PRSV EoS. For the MAH EoS, six material dependant parameters were selected as the inputs. All the parameters were assumed to have a Gaussian distribution with a standard deviation of 3% of the mean. The first part of the study involved analysing the influence of the uncertainty in input parameters on the shape and the location of the fundamental derivative of gas dynamics isolines. An analysis of the results indicate that more complex models implementing the MAH EoS are affected more by the uncertainties as they require more input parameters as compared to simpler models employing the PRSV and RKS EoS. Thus as the complexity of the model increases, the uncertainty in the output also increases. The second part of the study analysed the flow of dense gases over an airfoil by computing the pressure coefficients along the airfoil surface. Again the results indicate that the complex models are affected more by the input uncertainties. Also in the shock region, the computed pressure coefficients vary by as much as 40%. This indicates that in regions of strong non-linear behaviour, the effect of the uncertainties is magnified. From the results documented it was concluded that simple models like PRSV are a suitable for the analysis of dense gas regions in terms of balancing accuracy and computational cost.

Vitale et al. [11] performed a study on the fluid dynamic design and analysed the losses in a highly loaded centrifugal rotor for mini ORC power systems. Multi-stage centrifugal turbines are a viable option for power production in ORC systems. However the first stage in these turbines are highly loaded. Thus a careful design of the first stage is necessary and is critical to the overall performance of the turbine. A preliminary design methodology for the generation of centrifugal blade profiles is provided in this study. This can act as a basis for further improvement in the performance of turbines by performing shape optimization. A 2-D computational fluid dynamic (CFD) simulation of the generated rotor blade and a 3-D CFD simulation of the first stage rotor cascade was performed to estimate the losses. The contours of the relative Mach number show the shock waves generated at the trailing edge of the blade. From the CFD results it was concluded that the shock waves have a significant effect on the losses in a turbine.

1-5 Outline

The report is structured as follows:
Chapter 2 presents a theoretical background on the thermodynamic and gas dynamic concepts used in this study. This includes the fundamentals of compressible flows with a focus on shock waves, thermodynamic models, details of the ORCHID facility and a brief review of the method of characteristics employed for nozzle design. Thereafter, **Chapter 3** provides an introduction to uncertainty quantification (UQ) and discusses two sampling approaches and a sensitivity analysis method. The chapter proceeds by describing the UQ analysis performed in this study and presents the results obtained. **Chapter 4** provides a short introduction to RANS modelling. Thereafter, the results of the verification of the UQ analysis performed is presented. The chapter concludes by providing an application of the study and presents the results of the CFD simulations performed on quantifying the losses in a radial outflow turbine. Finally, conclusions are drawn in **Chapter 5** and recommendations for future work are provided in **Chapter 6**.

Chapter 2

Theoretical Background

This chapter provides a theoretical review of the gas dynamic and thermodynamic concepts applied in this study. A brief discussion of normal and oblique shock waves is presented with the equations denoting the variation of thermodynamic properties across the shock waves. Section 2-2 describes the supersonic flow of vapour over a wedge and discusses the Euler shock wave simulator code used in this study. Furthermore, the ideal gas and the iPRSV EoS which represent the thermodynamic properties of the ideal gas and the real gas regions respectively together with the departure functions are described in Section 2-3. A thorough description of the ORCHID set-up is presented in Section 2-4. The chapter concludes with the explanation of the method of characteristics in Section 2-5.

2-1 Compressible Flow Phenomena

At supersonic speeds, the density changes in the fluid are too large to be ignored. Such flows with variable density are termed as compressible flows. The compressibility, τ of a fluid with specific volume v is given as

$$\tau = -\frac{1}{v}\frac{dv}{dp} \tag{2-1}$$

In terms of density ρ and pressure p of the fluid, Equation 2-1 becomes

$$\tau = \frac{1}{\rho}\frac{d\rho}{dp} \tag{2-2}$$

Fluids moving at high velocities are accompanied by high pressure gradients. For such fluids, the change in density is also large, as seen from Equation 2-2. In general, if the density of a fluid varies by more than 5 percent it is considered as compressible [2].

The conservation equations for compressible fluid flowing through a control volume $\mathscr{V}$ and over a control surface area A is given as,

$$\int_{\mathscr{V}} \frac{\partial \rho}{\partial t} d\mathscr{V} + \int_A \rho \boldsymbol{V} \cdot dA = 0 \tag{2-3}$$

$$F_{surface} + \int_{\mathcal{V}} \boldsymbol{B}\rho d\mathcal{V} = \int_{\mathcal{V}} \frac{\partial}{\partial t}(\rho \boldsymbol{V})d\mathcal{V} + \int_{A} \boldsymbol{V}(\rho \boldsymbol{V} \cdot d\boldsymbol{A}) \tag{2-4}$$

$$\dot{W}_{shaft} + \dot{W}_{shear} - \dot{Q} + \int_{\mathcal{V}} \frac{\partial}{\partial t}\left[\rho\left(u + \frac{V^2}{2} + gz\right)\right]d\mathcal{V} + \int_{A}\left(h + \frac{V^2}{2} + gz\right)(\rho \boldsymbol{V} \cdot d\boldsymbol{A}) = 0 \tag{2-5}$$

Equations 2-3 - 2-5 denote the mass, momentum and energy conservation equations respectively. In Equation 2-4, $F_{surface}$ is the sum of all external forces acting on the surface of the control volume and $\boldsymbol{B}$ is the body force per unit mass. In the energy conservation equation, $\dot{W}_{shaft}$ represents the work done by a rotating shaft such as the work done by a compressor or any other machine while $\dot{W}_{shear}$ denotes the work done by the shear stresses. The conservation equations described above are general and valid for steady and unsteady flows in constant area as well as varying area ducts.

The common compressible flow phenomena prevalent in a varying area ducts like converging diverging nozzles are expansion waves and shock waves. Figure 2-1 illustrates shock waves and expansion fans formed in varying area ducts. Expansion fans are generated when the streamlines of a flow are deflected downward away from the main flow. In contrast shock waves are formed when the streamlines are deflected into the main flow. Both these compressible flow phenomena lead to compression of the fluid, but the major difference between them in that the compression process in an expansion wave is isentropic while shock waves generate entropy. In the ORCHID set-up, a model (wedge, needle, diamond) is placed in the test section which generates shock waves. Expansion waves are out of the scope of this work hence are not discussed further. The following section discusses the shock wave theory in detail.

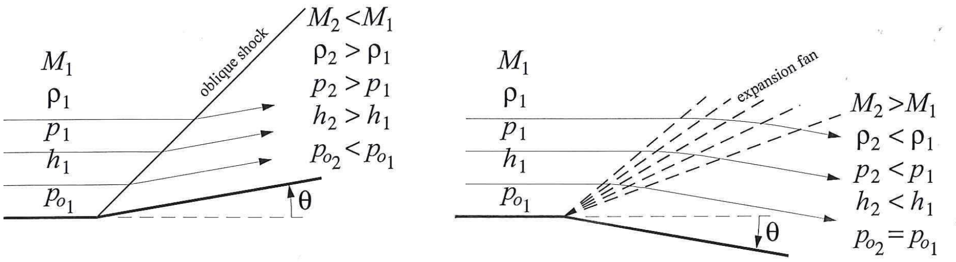

Figure 2-1: Shock wave and expansion fan generated in varying area ducts with the change in properties across them.

2-1-1 Shock Waves

A shock wave is an instantaneous compression of a fluid formed due to the supersonic movement of the fluid over an object. Due to the high speeds, a zone of disturbance is created in the vicinity of the object which causes an increase in the pressure. This abrupt increase in pressure gives rise to shock waves. The formation of shock waves is an irreversible process. A part of the kinetic energy possessed by the fluid is used to compress the fluid as it flows through the shock wave. The decrease in the kinetic energy leads to heating of the fluid and an increase in its temperature. As compared to an isentropic compression process between the same pressure limits, the reduction in kinetic energy and the rise in the temperature of the fluid is larger for flow through a shock wave. Thus a fluid flowing through a shock wave experiences a loss in energy and consequently an increase in its entropy.

Two types of shock waves having different characteristics along with their conservation equations are discussed in the following subsections.

2-1-1-1 Normal shock waves

Shock waves perpendicular to the flow direction are termed as normal shock waves. These waves are detached and occur at a short distance in front of the body. Figure 2-2(a) shows a normal shock wave formed in front of a cylinder. Due to the flow being supersonic, sound waves coalesce in front of the cylinder and cause the formation of a normal shock wave. As the flow passes through the shock wave the streamlines are deflected and the flow downstream of the shock wave moves around the cylinder. Figure 2-2(b) illustrates the variation of properties across the normal shock. The flow upstream of the shock is supersonic while the flow downstream of a normal shock is subsonic. Across a normal shock wave, the Mach number decreases, while the pressure, density and temperature increases. The relations for normal shock waves for steady, adiabatic flows with the body forces neglected, obtained from the conservation equations are given below.

$$\rho_1 V_1 = \rho_2 V_2 \tag{2-6}$$

$$p_1 + \rho_1 V_1^2 = p_2 + \rho_2 V_2^2 \tag{2-7}$$

$$h_1 + \frac{V_1^2}{2} = h_2 + \frac{V_2^2}{2} \tag{2-8}$$

where, p, V, ρ and h denote the pressure, velocity, density and enthalpy respectively. The subscript 1 refers to flow conditions upstream of the shock wave while subscript 2 denotes the conditions downstream of the shock. Using the above equations and given the properties upstream of the normal shock wave, all the properties downstream of the shock wave can be computed.

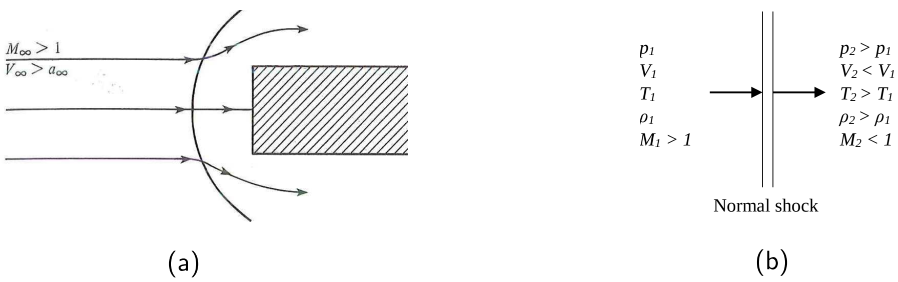

Figure 2-2: Normal shock wave (a) Normal shock formed in front of a cylinder [2] (b) Variation of pressure, enthalpy, velocity, density and Mach number across a shock wave.

2-1-1-2 Oblique shock waves

Shock waves inclined to the flow direction are termed as oblique shock waves. Oblique shock waves are two dimensional in nature as opposed to normal shock waves and can be generated by placing a wedge or a cone in a supersonic flow [2]. Figure 2-3 shows the geometry of an oblique shock wave generated due to an obstruction in the flow field having a flow turning angle of θ. The shock wave angle is denoted by β while V_T and V_N denote the tangential and normal component of the velocities and M_T and M_N represent the tangential and normal component of the Mach number respectively. The relations for an oblique shock wave for a steady, adiabatic flow with no body forces are given below.

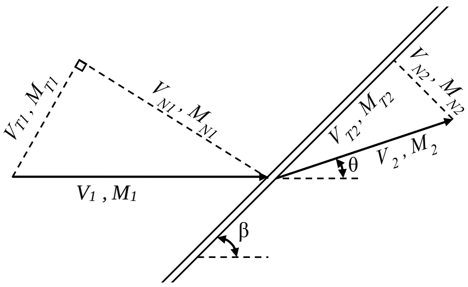

Figure 2-3: Oblique shock wave geometry.

$$V_{T1} = V_{T2} \tag{2-9}$$

$$\rho_1 V_{N1} = \rho_2 V_{N2} \tag{2-10}$$

$$p_1 + \rho_1 V_{N1}^2 = p_2 + \rho_2 V_{N2}^2 \tag{2-11}$$

$$h_1 + \frac{V_{N1}^2}{2} = h_2 + \frac{V_{N2}^2}{2} \tag{2-12}$$

The tangential component of the velocity across an oblique shock wave remains constant. Equations 2-10 - 2-12 are similar to the relations obtained for a normal shock wave (Equations 2-6 - 2-8)with the velocity V_1 and V_2 replaced by the normal component of the velocities in front and behind the shock wave. From the above conservation equations, the ratio of the densities, pressures and temperatures across the shock wave can be expressed in terms of the normal component of the upstream Mach number M_{N1} and the ratio of specific heat γ, for an ideal gas as:

$$\frac{\rho_2}{\rho_1} = \frac{(\gamma+1)M_{N1}^2}{2+(\gamma-1)M_{N1}^2} \tag{2-13}$$

$$\frac{p_2}{p_1} = 1 + \frac{2\gamma}{\gamma+1}(M_{N1}^2 - 1) \tag{2-14}$$

$$\frac{T_2}{T_1} = \frac{p_2}{p_1}\frac{\rho_1}{\rho_2} \tag{2-15}$$

The entropy generated by the oblique shock wave can be expressed in terms of the pressure ratio according the the following equation:

$$s_2 - s_1 = C_V ln\left[\frac{p_2}{p_1}\left(\frac{\rho_1}{\rho_2}\right)^{\gamma}\right] \tag{2-16}$$

The strength or the intensity of a shock wave is frequently expressed in terms of a shock wave intensity δ as,

$$\delta = \frac{p_2 - p_1}{p_2} \tag{2-17}$$

Substituting Equations 2-13, 2-14 and 2-17 into Equation 2-16, the entropy generated can be written in terms of the shock wave intensity parameter, δ.

$$\frac{s_2 - s_1}{C_V} = \frac{1}{1-\delta}\left[\frac{(1-\delta)(\gamma+1)+(\gamma-1)}{(1-\delta)(\gamma-1)+(\gamma+1)}\right]^{\gamma}$$

Equations 2-13 - 2-15 combined with the relation for the speed of sound in an ideal gas i.e $a = \sqrt{\gamma p/\rho}$ and the geometry of an oblique shock wave yields a relation to compute the downstream Mach number given below.

$$M_{N2}^2 = \frac{M_{N1}^2 + [2/(\gamma-1)]}{[2\gamma/(\gamma-1)]M_{N1}^2 - 1} \tag{2-18}$$

$$M_2 = \frac{M_{N2}}{sin(\beta - \theta)} \tag{2-19}$$

From the geometry of the oblique shock wave and the mass conservation equation, a relation between the shock wave angle, the flow turning angle and the velocities is obtained.

$$\frac{\tan(\beta-\theta)}{\tan\beta} = \frac{V_{N2}}{V_{N1}} \tag{2-20}$$

From Equations 2-13 and 2-20, and using trigonometric identities, the $\theta - \beta - M$ relation is obtained which is given as,

$$\tan\theta = 2\cot\beta\left[\frac{M_1^2 sin^2\beta - 1}{M_1^2(\gamma + cos2\beta) + 2}\right] \tag{2-21}$$

Equation 2-20 can be written in the form of a quadratic equation in terms of ν, where $\nu = \frac{\rho_1}{\rho_2}$ and is given below.

$$\tan\beta = \frac{(1-\nu) \pm [(1-\nu)^2 - 4\nu\tan^2\theta]^{1/2}}{2\nu\tan\theta} \tag{2-22}$$

The $\theta - \beta - M$ relation along with the above equation are used in developing the Euler shock wave simulator code which is detailed in Section 2-2-1.

Equation 2-18 is valid only for an ideal gas. For any fluid, the downstream Mach number can be expressed as a function of thermodynamic quantities namely, the velocity, pressure ratio and the speed of sound and the geometric parameters namely, the shock wave angle and the flow turning angle according to Equation 2-23. Thus the thermodynamic properties have a direct influence on the Mach number downstream of a shock wave.

$$M_2 = f(V_2(\beta(\theta, \frac{p_2}{p_1})\theta), a_2(p_2, h_2)) \tag{2-23}$$

A special case of an oblique shock wave is a Mach wave. A Mach wave is a weak oblique shock wave propagated at an angle of

$$\mu = \sin^{-1} \frac{1}{M_1} \tag{2-24}$$

where M_1 is the Mach number in front of the Mach wave. Mach waves are useful in determining the Mach number of the flow at any point in a wind tunnel. In a supersonic wind tunnel Mach waves can be generated by placing a slender pin having a small flow turning angle in the flow path. The Mach waves thus generated can be viewed using techniques such as PIV or Schlieren to determine the Mach angle. From this angle, the Mach number at a point in the flow can be determined as the Mach number is a function of the Mach angle only as seen in Equation 2-25.

$$M_{tip} = f(\mu) \tag{2-25}$$

2-2 Supersonic Flow over a Wedge

Figure 2-4 shows the oblique shock waves generated due to a wedge placed in a supersonic flow. Whether the shock wave remains attached to the wedge or detaches depends on the value of the flow turning angle and the upstream Mach number M_1. A maximum value of flow turning angle θ_{max} exists corresponding to M_1. If $\theta < \theta_{max}$, then the oblique shock wave is attached to the tip of the apex of the wedge as shown in Figure 2-4(a). As the flow passes through the shock wave, the streamlines are deflected by an angle equal to the flow turning angle. Since the flow is compressed in a shock wave, the streamlines immediately behind the shock wave are spaced closer to each other than they are in front of the shock wave [4]. If θ $> \theta_{max}$, then the shock wave detaches from the wedge as shown in Figure 2-4(b). A normal shock wave is formed immediately in front of the wedge at its tip. The flow immediately behind the shock wave is subsonic. As θ is increased further beyond θ_{max}, the normal shock wave moves away from the wedge.

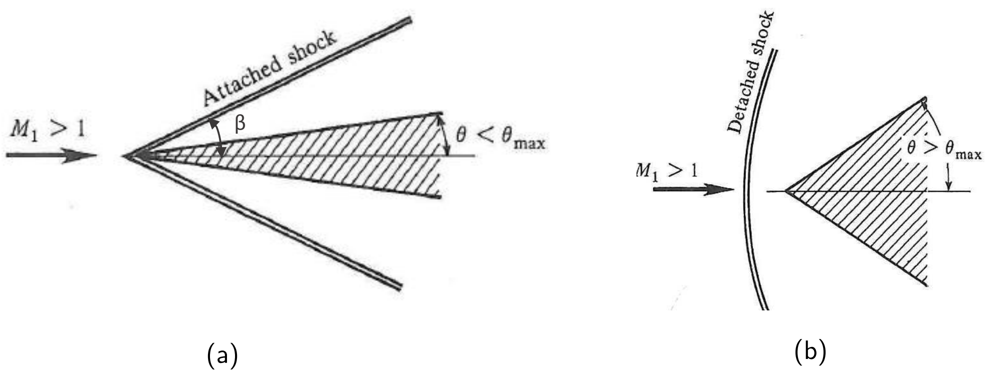

Figure 2-4: Flow over a symmetrical wedge (a) Attached shock wave (b) Detached shock wave [2].

The relation between the flow turning angle, the oblique shock wave angle and the upstream Mach number for an ideal gas can be shown in the form of a diagram plotted using Equation 2-21. The resulting figure is called as the $\theta - \beta - M$ diagram and is shown in Figure 2-5. Given a value of the flow turning angle and the upstream Mach number which are generally known, the oblique shock wave angle can be estimated from the diagram.

Interpretation of the $\theta - \beta - M$ diagram:

- As explained above, there is a maximum value of θ corresponding to a given value of M_1. If $\theta > \theta_{max}$, no solution exists for an oblique shock wave and the shock wave is detached as shown in Figure 2-4(b). As M_1 decreases, the value of θ_{max} also decreases.
- If $\theta < \theta_{max}$, then the shock wave is attached to the tip of the wedge. Two values of the shock wave angle can be determined from Equation 2-21. The lower value corresponds to a weak oblique shock wave while the larger value corresponds to a strong shock. Generally the weak shock occurs most frequently (see Ref. [2]) and hence the lower of the two values is considered. In Figure 2-5, the red curve represents the weak shock which corresponds to lower values of β whereas the blue curve represents the strong shock solutions.
- If $\theta = 0$, then β is either 90° corresponding to a normal shock or equal to μ corresponding to a Mach wave. The red and blue asterisk in Figure 2-5 represent the Mach angle and the normal shock wave angle respectively.

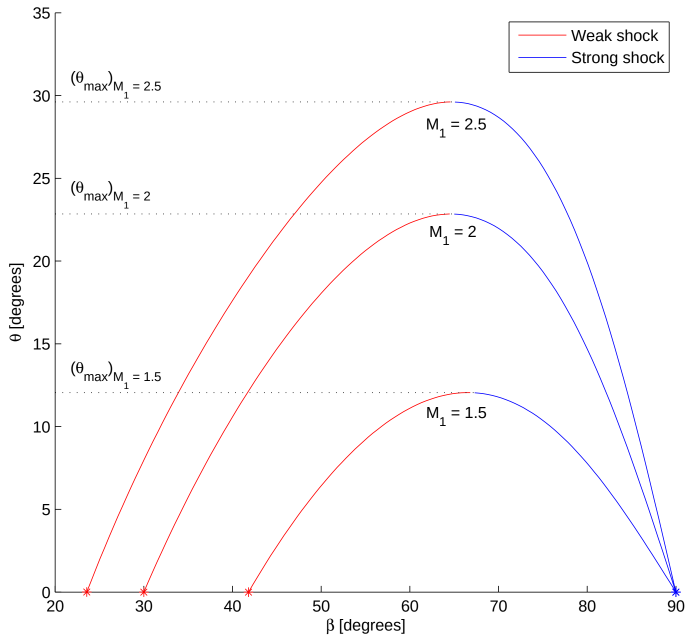

Figure 2-5: $\theta - \beta - M$ diagram of air plotted at three arbitrary Mach numbers of 1.5, 2 and 2.5. The red curve and blue curve correspond to weak shocks and strong shocks respectively. The red asterix and the blue asterix represent the Mach angle and the normal shock wave angle respectively.

2-2-1 Euler Shock Wave Simulator

The $\theta - \beta - M$ diagram plotted using Equation 2-21 is valid only for an ideal gas. For plotting the diagram for fluids in the real gas region in addition to ideal gas region, an integral based Euler shock wave simulator code is used in this study. The code employs an iterative procedure to solve Equation 2-22 and computes the shock wave angle from the given input values of the Mach number, pressure and density in front of the shock wave. For convenience of the reader the equation is given here again. The iterative procedure followed is documented in Appendix A.

$$\tan\beta = \frac{(1-\nu) \pm [(1-\nu)^2 - 4\nu\tan^2\theta]^{1/2}}{2\nu\tan\theta}$$

Before using the code in the simulations, it is verified by comparing the results obtained with the $\theta - \beta - M$ relation for air. Figure 2-6 shows the θ-β-M diagram plotted using the Euler shock wave simulator code and Equation 2-21 for flow through a de-Laval nozzle such that Mach numbers of 1.5, 2 and 2.5 are achieved at the exit which are characteristic of supersonic ORC turbines [18]. The inlet temperature and pressure are 525.15 K and 18.4 bar respectively which is the design operating conditions of the ORCHID set-up [1]. The plots for the three different Mach numbers and the values of the deviation reported in Table 2-1 show that the results from the Euler shock wave simulator code compare well with the $\theta - \beta - M$ relation.

Table 2-1: Average deviation of the Euler shock wave simulator from the $\theta - \beta - M$ diagram for Mach numbers of 1.5, 2 and 2.5 respectively.

Mach number	**Average deviation from the $\theta - \beta - M$ diagram [%]**
1.5	0.54
2	0.67
2.5	0.78

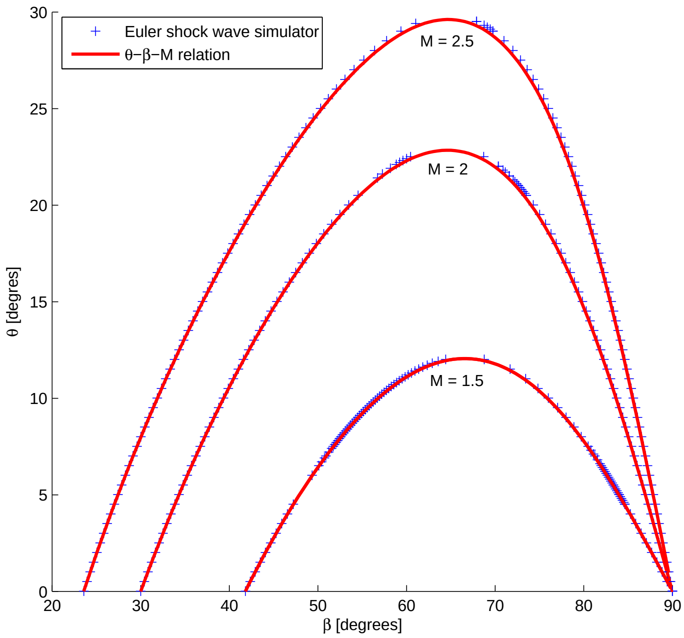

Figure 2-6: Verification of the Euler shock wave simulator code for air.

2-3 Thermodynamic models

The properties of fluids can be defined using a thermodynamic model implementing an EoS (eg. ideal gas model) or tabulated data (eg. steam tables). However, for complex numerical simulations such as those considered in this study, thermodynamic models are preferred since they can predict the properties of the fluid with thermodynamic consistency and high degree of accuracy [19]. Several models have been proposed to predict the behaviour of fluids. In the following subsections two of these models namely, the ideal gas model and the iPRSV model are discussed.

2-3-1 Ideal Gas Model

A gas is a collection of molecules which are in constant random motion. The motion of a molecule in a gas depends on the forces exerted on it by neighbouring molecules. This force is termed as intermolecular force. The internal energy of a gas depends on this intermolecular force and is a function of temperature and pressure. The intermolecular force is large in a system maintained at a high pressure where the particles are close to each other while it is small in case of a system in which the particles are at large distances from each other. Thus the pressure dependency of the internal energy arises from the forces between the molecules. If the intermolecular forces are negligible, then the internal energy of the system depends solely on the temperature of the gas. The behaviour of such a gas in which the intermolecular forces are negligible and the internal energy is a function of temperature only can be described by the ideal gas model. The EoS governing the ideal gas model is given as,

$$pv = RT \tag{2-26}$$

where, R is the specific gas constant in $J/(kg.K)$.

The concept of an ideal gas is hypothetical but is commonly used for many compressible flow applications [2]. In practice, gases are never ideal and for accurate estimation of their properties, a more comprehensive thermodynamic model is needed.

2-3-2 Improved Peng Robinson Strjyek Vera (iPRSV) Model

The iPRSV model is a modified version of the PRSV model. ORC turbines generally operate in the dense gas region due to the high expansion ratio of the fluids [20]. The behaviour of fluids are complex in this region and can no longer be described by simple models like the ideal gas model. To accurately predict the behaviour of such fluids, the iPRSV EoS was proposed. The iPRSV EoS is similar to the PRSV EoS except for the κ term which is calculated using a modified equation such that it is continuous with temperature. The iPRSV EoS is given as,

$$P = \frac{RT}{v-b} - \frac{a}{v^2 + 2bv - b^2} \tag{2-27}$$

where,

$$a = \left(\frac{0.457235R^2T_c^2}{P_c}\right)\alpha \tag{2-28}$$

$$b = \frac{0.077796RT_c}{P_c} \tag{2-29}$$

The α function in Equation 2-28, proposed by Soave [21] is given by

$$\alpha = [1 + \kappa(1 - \sqrt{T_r})]^2 \tag{2-30}$$

where κ is a function of the reduced temperature and is given by the relation

$$\kappa = \kappa_0 + \kappa_1\Big\{\sqrt{[A - D(T_r + B)]^2 + E} + A - D(T_r + B)\Big\}\sqrt{T_r + C} \tag{2-31}$$

where κ_1 is an adjustable parameter specific to each pure compound. The value of the coefficients of the κ function are given in Table 2-2.

In Equation 2-31, κ_0 is given by

$$\kappa_0 = 0.378893 + 1.4897153\omega - 0.17131848\omega^2 + 0.0196554\omega^3 \quad (2\text{-}32)$$

and the acentric factor ω is defined at a reduced temperature of 0.7 in terms of the reduced pressure as,

$$\omega = -log_{10}(p_r^{sat}) - 1 \quad (2\text{-}33)$$

The ideal gas specific heat at constant pressure is approximated using a polynomial function [8].

$$C_p^{ig} = Cp_{01} + (Cp_{02} * 10^{-3})T + (Cp_{03} * 10^{-6})T^2 + (Cp_{04} * 10^{-9})T^3 \quad (2\text{-}34)$$

The iPRSV EoS provides a better representation of the properties of a fluid in the real gas region as compared to the ideal gas model. A fluid is said to be in the real gas region when its caloric properties i.e. the specific heats ($\mathrm{C_P}$ and $\mathrm{C_V}$) vary with temperature and pressure. In addition, the compressibility factor, Z given by Equation 2-35 deviates from 1. Thus, the iPRSV EoS is preferred for the analysis as it is suitable for fluids in the thermodynamic region in which ORC systems operate and at the same time this model is relatively simpler having less input parameters in contrast to available multi parameter EoS.

$$Z = \frac{pv}{RT} \quad (2\text{-}35)$$

Table 2-2: Coefficients of the κ - function of the iPRSV EoS [8].

Coefficient	Value
A	1.1
B	0.25
C	0.2
D	1.2
E	0.01

2-3-3 Departure Functions

The extent of deviation of a fluid from the ideal gas conditions are estimated using the departure functions. In general, departure functions are defined for extensive thermodynamic property like internal energy U, enthalpy H, entropy S, Gibbs energy G and specific heat at constant pressure C_P and volume C_V. At zero pressure or infinite volume, the value of these functions is zero. They are defined in terms of enthalpy, entropy and isobaric specific heat as

$$H^d = H - H^{ig}, \qquad S^d = S - S^{ig} \qquad \text{and} \qquad C_P^d = C_P - C_P^{ig} \quad (2\text{-}36)$$

In Equation 2-36, H^{ig}, S^{ig} and C_P^{ig} refer to the ideal gas part of enthalpy, entropy and isobaric specific heat while H, S and C_P refer to the total properties including the real gas effects i.e. the specific heats are no longer a single constant value but functions of temperature. The general expressions for computing the departure functions from experimental data or from EoS are given below [22].

$$\frac{H^{ig} - H}{RT} = \int_V^{\infty} \left[T \left(\frac{\partial Z}{\partial T} \right)_V \right] \frac{dV}{V} + 1 - Z \tag{2-37}$$

$$\frac{S^{ig} - S}{RT} = \int_V^{\infty} \left[T \left(\frac{\partial Z}{\partial T} \right)_V - 1 + Z \right] \frac{dV}{V} - lnZ \tag{2-38}$$

$$\frac{C_P}{R} = \frac{C_P^{ig}}{R} - 1 - T \int_V^{\infty} \left[T \left(\frac{\partial^2 P}{\partial T^2} \right)_V \right]_T dV - T \left(\frac{\partial P}{\partial T} \right)_V^2 \Big/ \left(\frac{\partial P}{\partial V} \right)_T \tag{2-39}$$

Equations 2-37 - 2-39, provide analytical expressions for calculating the extent of deviation of a fluid from the ideal gas law. They are commonly used when the EoS is expressed in terms of Z as a function of temperature and volume at a constant composition.

Figure 2-7 illustrates an example of the real gas effects on the computed thermodynamic properties with the operational points of the ORCHID set-up (See Ref. [1]) indicated. The compressibility factor at the throat is 0.69 which indicates that the flow within the nozzle operates in the real gas region. The variation of the isobaric specific heat with the reduced pressure for MM (hexamethyldisiloxane, $C_6H_{18}OSi_2$) computed using the iPRSV EoS under isentropic conditions is shown. For reduced pressure up to 0.8, the change in C_P is less as compared to the higher values. At low values of the reduced pressure the fluid is in the ideal gas region where the gradients in the properties do not change abruptly and hence the value of the differential terms in Equation 2-39 are invariant. As the fluid approaches the critical conditions and enters the dense gas region, the variation of the properties is non-linear which leads to large changes in the differential term. In Figure 2-7, a significant increase in the specific heat is observed close to reduced pressure of 1 which is caused due to the large variation in the last term in Equation 2-39 i.e. $(\partial P/\partial V)_T$. Close to the critical point this term approaches zero thus causing a significant rise in the isobaric heat capacity. Similar behaviour can be observed for other properties as they depart from the ideal gas region.

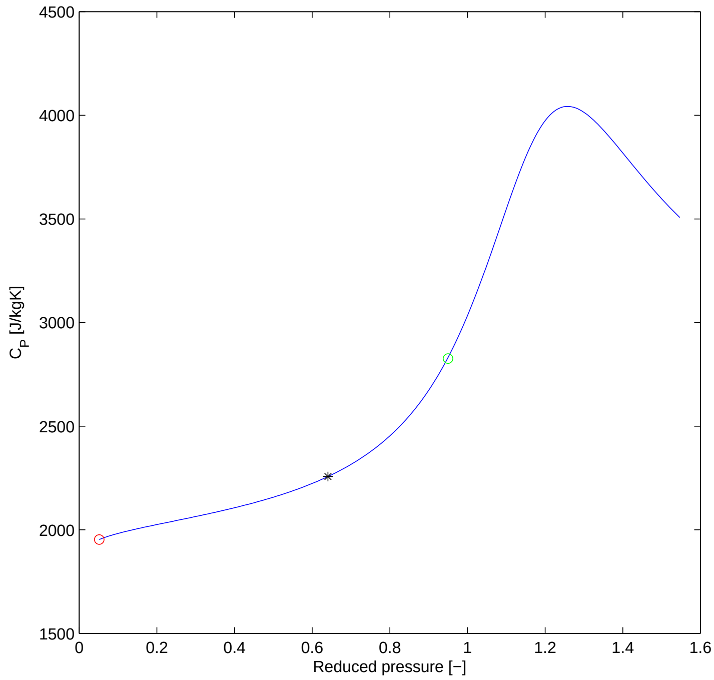

Figure 2-7: Variation of the isobaric specific heat with reduced pressure at a constant entropy of MM. The green and red circles indicate the inlet and exit conditions of the nozzle respectively obtained from Ref. [1]. The asterisk denotes the conditions at the throat of the nozzle.

Figure 2-8 shows the deviation in $\theta - \beta - M$ diagram computed using two different thermodynamic models. The curves are plotted for MM using the StanMix model which implements the iPRSV EoS and the GasMix model which uses the ideal gas law to compute the thermodynamic properties. As seen from the figure, the GasMix model significantly under estimates the shock wave angles because the real gas effects are neglected. Thus the departure functions are important and should be taken into account to simulate the behaviour of fluids in the dense gas region.

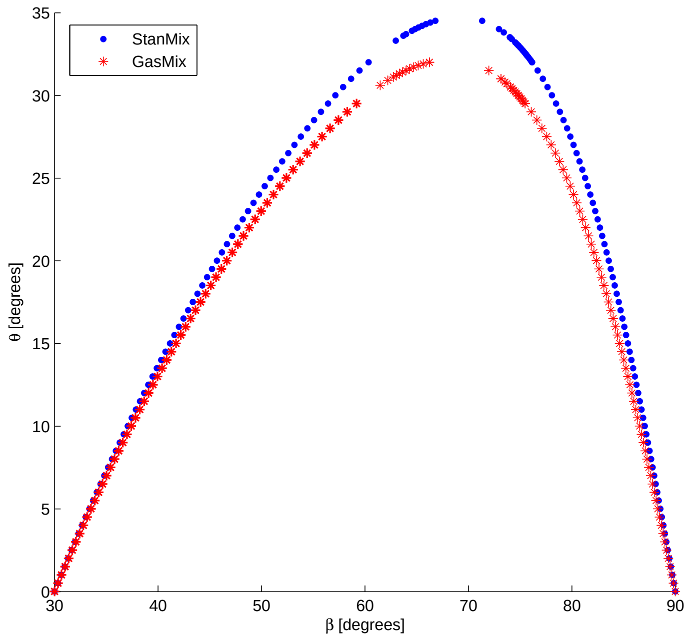

Figure 2-8: $\theta - \beta - M$ diagram plotted for MM at a constant Mach number of 2. The blue curve is plotted using the iPRSV model while the red curve uses the ideal gas model.

2-4 The ORCHID Set-up

The Organic Rankine Cycle Hybrid Integrated Device (ORCHID) is a continuous supersonic vapour tunnel and turbomachinery facility [1]. The purpose of the test set-up is to validate the in-house CFD codes and understand NICF phenomena in dense organic vapours. It is designed to accommodate multiple organic fluids at different operating conditions. In the first stages of the experimental program, studies related to fundamental gas dynamics are conducted in a de-Laval nozzle. Later stages of the program are dedicated to performance analysis of turbomachinery.

Figure 2-9 shows a simplified process flow diagram of the ORCHID facility. The dotted rectangles represent the two test sections - nozzle and turbine. Stations 1-4 represent the expansion in the nozzle and the turbine. From stations 4-5, the hot vapours of the organic fluid are cooled in a regenerator by transferring heat to the high pressure cold fluid leaving the pump. Vapours of the organic fluid are condensed by transferring heat to a cooling water circuit from stations 5-6. The condensed fluid is then pumped to the operating pressure from stations 6-7 and heated to the operating temperature in the primary heat exchanger which is represented by station 7-1.

This work focuses on the study of compressible flow phenomena in the converging - diverging nozzle. Hence a detailed description of the nozzle set up is provided in the following subsection.

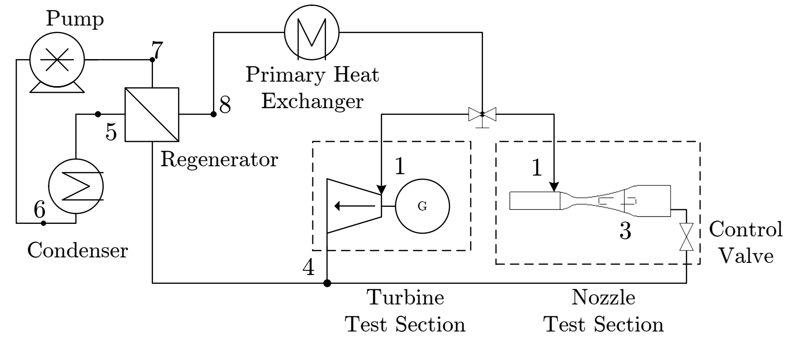

Figure 2-9: Simplified process flow diagram of ORCHID facility [1].

2-4-1 Nozzle Test Section

The nozzle test section is an integral part of the ORCHID set-up. It consists of a settling chamber, converging-diverging nozzle, test section channel, receiver and a valve to control the back pressure of the test section. Figure 2-10 shows all the components with the exception of the receiver and the valve. To meet the power requirements of the set-up and minimize the boundary layer effects, a throat area of 200 mm^2 corresponding to a width of 20 mm and a height of 10 mm [1] is chosen. A detailed description of the sizing and specifications of each component in the nozzle test section is provided in Ref. [23].

The experiments in the nozzle test section would be conducted by progressively inserting a model i.e. a slender pin, diamond or wedge in the diverging section to induce shock waves. As mentioned in Section 2-1-1-2, the Mach number of the flow can be easily determined by placing a slender pin in the flow path and determining the angle of the resulting Mach cone. Figure 2-10 illustrates the real gas region formed at the nozzle throat and Mach waves generated due to supersonic flow over a slender pin. The letters a, b and c denote the Mach waves generated at the tip of the pin, shock waves at the end of the model and the slender pin respectively. The angle μ is used to estimate the Mach number using Equation 2-24. The same principle applies to other geometric objects such as a wedge or a diamond. These would generate an oblique shock wave which can be viewed using Schileren technique to determine the shock wave angle.

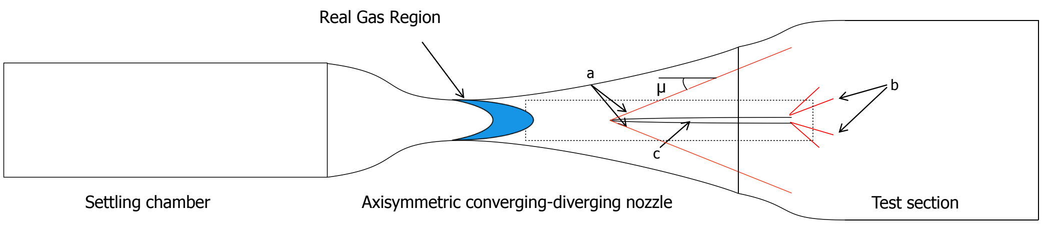

Figure 2-10: 2D outline of de-Laval nozzle used in the ORCHID set-up showing a slender pin used to generate Mach waves [1].

2-4-2 Cycle Specifications

The primary constraint of the ORCHID test set-up is the available thermal power input which is limited to 400 kW due to technical constraints of the laboratory. A minimum Mach number of 2 is maintained at the exit of the nozzle such that the flow in the nozzle resembles the flow downstream of a stator in a typical ORC turbine. In order to achieve the desired Mach number at the exit, a high pressure ratio is maintained across the nozzle. The outlet pressure is fixed to 1 bar which results in a high inlet pressure close to the critical conditions of the fluid. The reduced pressure at the inlet is chosen as 1.1 such that the power and the exit Mach number requirements are met. As the pressure is close to the critical pressure, the fluid expanding through the nozzle is affected by real gas effects as seen from Figure 2-11. As the value of the complement of the compressibility factor increases, the fluid departs from the ideal gas conditions. Thus at the inlet and the throat, the fluid experiences appreciable non-ideal effects. All the design constraints of the ORCHID set-up for studying these NICF phenomena are summarized in Table 2-3.

Table 2-3: ORCHID design constraints for the nozzle experiment [1].

	Variable	**Value**
Nominal thermal power (max)	$\dot{Q}_{in,max}$	370 $\mathrm{kW_{th}}$
Working fluid temperature (max)	$T_{1,\mathrm{max}}$	320 °C
Working fluid pressure (max)	$P_{1,max}$	25 bar
Inlet reduced pressure (min)	$P_{1,R}$	1.1
Nozzle Mach number (out)	M_{min}	2
Condenser pressure	$\mathrm{P_6}$	1.1
Throttling valve pressure drop	δP_{TV}	1 bar
Nozzle discharge pressure	P_3	1 bar
Degree of superheating	ΔT_{sh}	10 °C

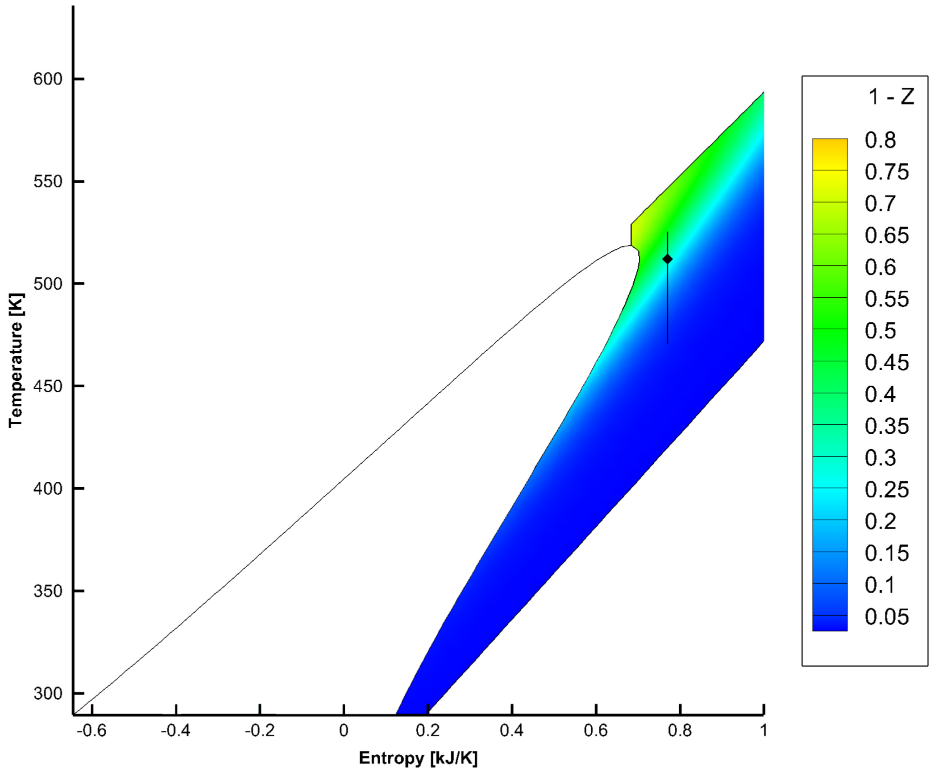

Figure 2-11: T-s diagram of MM showing the nozzle expansion and the complement of the compressibility factor. The diamond symbol located on the isentropic expansion line represents the conditions at the throat.

2-4-3 Selection of the Working Fluid

The design and performance of the nozzle and the turbine depends upon the choice of working fluid. The ORCHID set-up is designed to accommodate several organic fluids. However the choice is limited due to the to the strict requirements on the working fluids and the design constraints of the ORCHID set-up. Any potential working fluid candidate is expected to satisfy the following requirements:

- power required to run the test set-up with the selected working fluid should be less than 370 kW_{th} so as to allow some margin for thermal losses;
- suitable thermodynamic properties within the operational range. This includes the fluid being non-flammable and thermally stable at all operating conditions of the test rig;
- non-corrosive and non-toxic;
- readily available and low cost.

Head et al. performed a thermodynamic analysis of the test facility, the results of which are documented in Ref. [1]. Among the fluids that were tested the ones which could potentially be used are MM, MDM (octamethyltrisiloxane, $C_8H_{24}O_2Si_3$), D_4 (octamethylcyclotetrasiloxane, $C_8H_{24}O_4Si_4$), PP2 (perfluoromethylcyclohexane, $C_6F_{11}CF_3$), PP80 (perfluoro-2-methyl-3-ethylpentane, C_8F_{18}) and PP90 (perfluoro-2,4-dimethyl-3-ethylpentane, C_9F_{20}). The properties, operating conditions and power requirement for all the fluids are given in the table below.

Table 2-4: Properties and operating conditions of working fluid candidates [1].

Fluid	T_{CR} [°C]	P_{CR} [bar]	T_1 [°C]	P_1 [bar]	$\dot{m}$ [kg/s]	$\dot{Q}_{in}$ [kW_{th}]
MM	245.6	19.4	252	18.4	1.55	352
MDM	290.9	14.2	299	15.6	1.5	291
D_4	313.3	13.3	320	14.6	1.6	260
PP2	212.9	20.2	219	22.7	3	302
PP80	233.97	16.85	241	18.5	2.6	238
PP90	256.85	16	264	17.6	2.6	235

MM is one of the most promising fluids for ORC technology owing to its suitable thermodynamic properties and low cost. At reduced pressures above 1 bar, the power requirement of the test set-up operating with MM exceeds the maximum allowable limit of 370 kW_{th}. Hence to accommodate MM, an exception is made on the minimum reduced pressure criterion. The nozzle inlet pressure for MM is decreased below its critical value resulting in reduced inlet pressure of 0.95 so that it operates in sub-critical conditions thus fulfilling the constraint of maximum available thermal power. All other fluids are operated in super-critical conditions. Table 2-4 shows that MM and PP90 have the maximum and minimum power requirement respectively. Hence a further analysis is performed on these fluids. Figure 2-12 shows the variation of the compressibility factor with the logarithm of pressure for MM and PP90. The compressibility factor is calculated for a pressure range of 1 bar to 300 bar at a constant operational temperature of the fluid i.e 252 °C for MM and 264 °C for PP90. At the exit of the nozzle, the pressures are low. The intermolecular forces in the fluid are negligible and hence the fluid is assumed to be ideal as the compressibility factor is close to 1. As the fluid expands in a nozzle from the inlet and close to the throat, the pressure and the density is high. The fluid is in the so called dense gas region which is close to the critical conditions of the fluid. At these conditions the intermolecular forces cannot be neglected and the fluid shows significant deviations from the ideal gas behaviour. This is seen from the value of Z at the throat which is marked in the plot. In terms of power requirement and magnitude of real gas effects, PP90 seems to be a better choice of working fluid. But the cost of PP90 is much higher than MM and hence MM is chosen as the first fluid to be tested in the ORCHID set-up and is considered for all the analysis in this study. Nevertheless, the methods and tools developed in this study can be easily used and extended to other fluids.

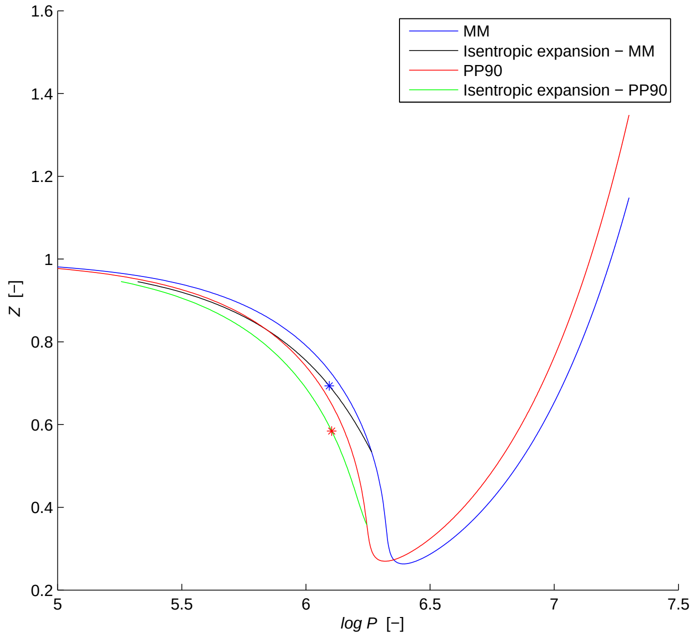

Figure 2-12: Z-log P diagram of MM and PP90 showing the isentropic expansion in the nozzle. The asterisk symbol located on the isentropic expansion line represents the conditions at the throat

2-5 Nozzle Design - Method of Characteristics

The Method of Characteristics (MoC) is the most accurate numerical technique to solve hyperbolic partial differential equations (PDE) [4]. The conservation equations for supersonic flows are hyperbolic and hence the MoC is relevant for such flow fields. The MoC is commonly used in the analysis of flows in nozzles of known shape and in the design of nozzles in supersonic wind tunnels. In this study, the MoC is used in designing the diverging portion of the nozzle. A brief description of the numerical method along with the equations for designing the diverging portion of the de-Laval nozzle are provided in this section.

The hyperbolic system of partial differential equations governing isentropic, irrotational supersonic flows are transformed into a set of characteristic and compatibility equations by performing mathematical operations on the governing equations. Reference [4] provides a detailed description of this procedure. The characteristic and the compatibility equations thus obtained for the flow in consideration are,

Characteristic equation

$$\left(\frac{dy}{dx}\right)_{\pm} = \lambda_{\pm} = tan(\theta \pm \alpha) \tag{2-40}$$

Compatibility equation

$$(u^2 - a^2)du_{\pm} + [2uv - (u^2 - a^2)\lambda_{\pm}]dv_{\pm} - (\delta a^2/y)dx_{\pm} = 0 \tag{2-41}$$

where u and v are the velocities in the x and y direction while a is the speed of sound computed from a thermodynamic model. The angles θ and α are shown in Figure 2-13(a).

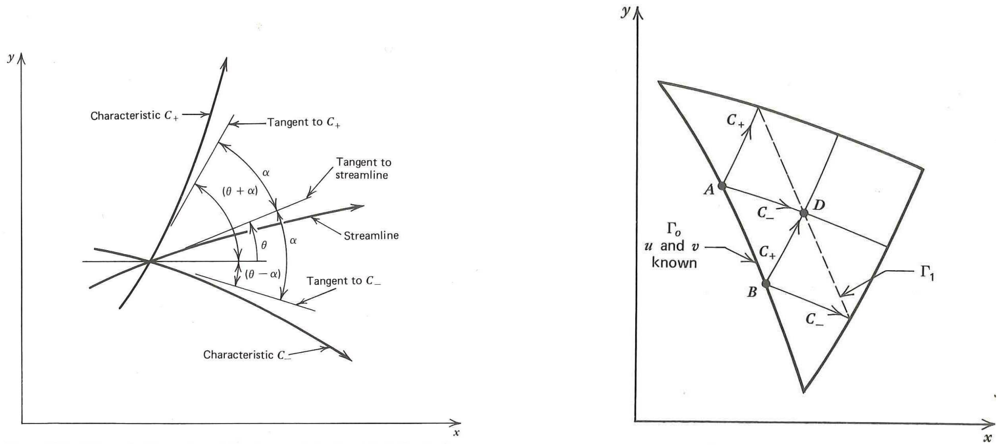

(a) (b)

Figure 2-13: MoC procedure (a) Characteristics and streamline from a point in the flow field [3] (b) Characteristics network generated using the MoC [4].

Equation 2-40 represents the paths along which disturbance in a supersonic flow field would propagate and are termed characteristic curves. Two characteristic curves are obtained and are represented as C_+ called as the right running wave and C_- called as the left running wave corresponding to the positive and the negative sign respectively. Equation 2-41 is the compatibility equation which gives a relationship between du, dv, dx and dy along the C_+ and C_- lines. Figure 2-13(b) illustrates the calculation of flow field properties at an interior point in a flow field. All the flow field properties are known along the initial value line represented by Γ_0. From any point on this line the C_+ and C_- lines can be extended into the flow field. At the intersection of the C_+ and the C_- lines the compatibility equations are solved simultaneously to compute the properties at that point. This procedure is repeated until a new initial value line, Γ_1 is produced. The new line is then used to compute the flow field downstream in the nozzle.

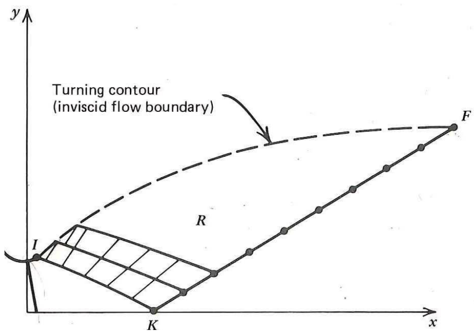

Figure 2-14: Determination of nozzle profile [3].

The procedure described above is used in generating the profile of the diverging section of the nozzle. Figure 2-14 illustrates the method used in determining the nozzle profile and the interior points. The nozzle is designed such that the flow at the exit is uniform and the design Mach number is achieved. The initial value curve is obtained from Sauer's analysis depending on the upstream conditions of the throat [3]. From this curve and the specified radius of curvature of the throat, the initial expansion flow field is determined such that the flow acquires the design Mach number. The region in Figure 2-14 up to curve IK represents this initial flow field. At point K, the Mach number is equal to the design Mach number. From this point, a straight line is generated at an angle of $sin^{-1}(1/M)$ where M is the design Mach number and extended up to F such that the mass flow rate through the initial value curve is equal to the mass flow rate through line KF. All the remaining points in the interior of the nozzle are computed from the curve IK and the line KF as shown in Figure 2-13(b). A point on the nozzle wall is located by carrying out a mass balance along the characteristic lines from an initial point on line KF. This procedure is repeated till the entire nozzle profile is generated.

In the present study, a Fortran executable developed by *Guardone et al.* (see Ref. [15]), that implements the MoC is used to design the nozzle. The nozzle is designed such that the Mach number and the back pressure at the exit of the nozzle are 2.3 and 1 bar respectively. These are in accordance with the operating conditions of the ORCHID facility for MM shown in Table 2-4. All the thermodynamic properties are computed using the iPRSV EoS. Figure 2-15 shows the nozzle profile and the contours of Mach number obtained. This nozzle profile would be used in performing the uncertainty quantification analysis detailed in the next chapter.

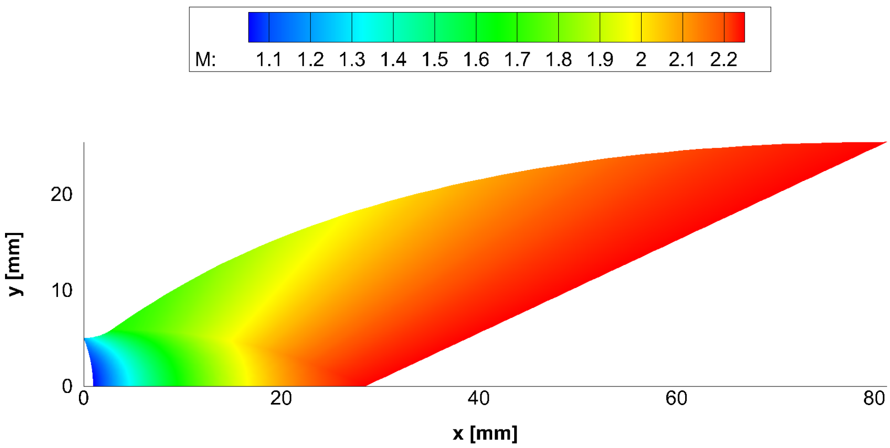

Figure 2-15: Nozzle geometry and Mach number contour plot computed using the MoC.

Chapter 3

Uncertainty Quantification

This chapter presents a detailed explanation of the uncertainty quantification analysis performed. Section 3-1 provides a brief introduction to uncertainty quantification. This is followed by a description of sampling techniques in Section 3-2 and a sensitivity analysis method in Section 3-3. Finally, Section 3-4 provides an extensive description on the UQ analysis implemented in this study. This section includes details about the uncertain parameters considered in this study and presents the results obtained from the simulations performed for different cases.

3-1 Introduction to Uncertainty Quantification

Uncertainty quantification is the process of characterizing input uncertainties, propagating these uncertainties through a computational model and performing a statistical analysis on the results obtained [17]. Uncertainties in a system can be classified into two types - aleatory and epistemic. Aleatory uncertainties are random, irreducible variabilities inherent in nature. As adequate information is available, the distribution of these uncertainties are known and hence common probabilistic methods can be used to determine their effect on the response functions. On the other hand, epistemic uncertainties are reducible uncertainties resulting from a lack of knowledge. They are generally characterized in terms of an interval i.e. by specifying the upper and the lower bounds of the variation [5]. As the available data is limited, sampling based methods are used to ascertain their effect on the response functions.

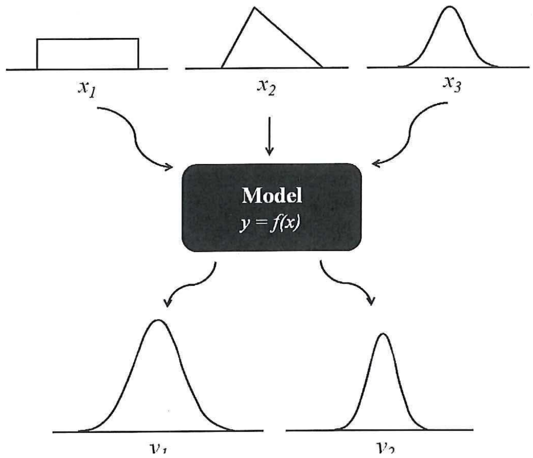

Figure 3-1: Illustration of uncertainty propagation [5].

Following the characterization of the uncertainty, the next step in an UQ analysis is the propagation of this uncertainty through a model, as shown in Figure 3-1, to obtain the statistics of the response function. This may be achieved through uncertainty quantification techniques such as Monte-Carlo simulations. A sensitivity analysis is performed to determine the parameters that contribute the most to the variability of the system. Samples of these parameters are generated within the specified bounds based on their probability density function. Each sample is then propagated through an analysis function or a model which uses the sample as an input and determines a value of the output. This process is repeated for each of the remaining samples and a set of output values are obtained. A statistical analysis of these output values quantifies the deviation in the response function due to the uncertainty in the input parameters.

The following section describes two common sampling methods and a sensitivity analysis technique that are used in the UQ analysis in the present study.

3-2 Sampling Techniques

Sampling based methods are effective and popular for performing uncertainty quantification analysis due to the simplicity in implementing them and their independence from the model used in the analysis [17], [24]. Sampling of the input variables is the first step in performing a UQ analysis. To generate reliable output statistics, efficient sampling of the uncertain input variables is vital. Several sampling techniques have been developed like Monte-Carlo sampling, Latin hypercube sampling, stochastic expansion methods, importance sampling, adaptive sampling, etc. Two of these sampling techniques, namely the Monte-Carlo and Latin hypercube sampling methods are used in this study. These are the relatively simple to implement as compared to other sampling methods and have an added advantage of being independent from the scientific disciplines of the analysis being performed [17]. The results obtained from Monte-Carlo and Latin hypercube sampling could be used as a basis for comparison with other methods. The two sampling methods are described in the following sections.

3-2-1 Monte-Carlo Sampling

Monte-Carlo sampling technique is the simplest procedure of generating stochastic samples from defined input probability density function (PDF) [6]. The method works by first sampling random numbers between 0 to 1 and then using the cumulative distribution function (CDF) of the input variable, the random samples are generated. The Monte-Carlo sampling approach is illustrated by Figure 3-2. Consider the generation of 5 random samples for x = [U,V] where U has a uniform distribution between the bounds 0 to 10 while V has a triangular distribution with a mode of 8 between the same bounds. The sampling for U and V is done by first generating 5 random numbers RU(1),...,RU(5) and RV(1),...,RV(5) between 0 to 1. The CDF of U and V are then used to obtain the values U(1),..,U(5) and V(1),...,V(5) as shown in the figure. From these values, the random samples are generated as,

$$x_i = [U(i), V(i)], \quad i = 1, 2, 3, 4, 5$$

The sampling is done in an analogous way for **x** having dimensions greater than two. Though the Monte-Carlo sampling technique is robust and simple, it could lead to clustering of samples and poor representation of the entire range of the input variables. Also, its application for computationally intensive problems is limited as it has a low convergence rate of the order of $1/\sqrt{N}$,where N is the number of samples, which could result in thousands of simulations to obtain reasonable output statistics [25]. To overcome these problems the Latin hypercube sampling technique was devised.

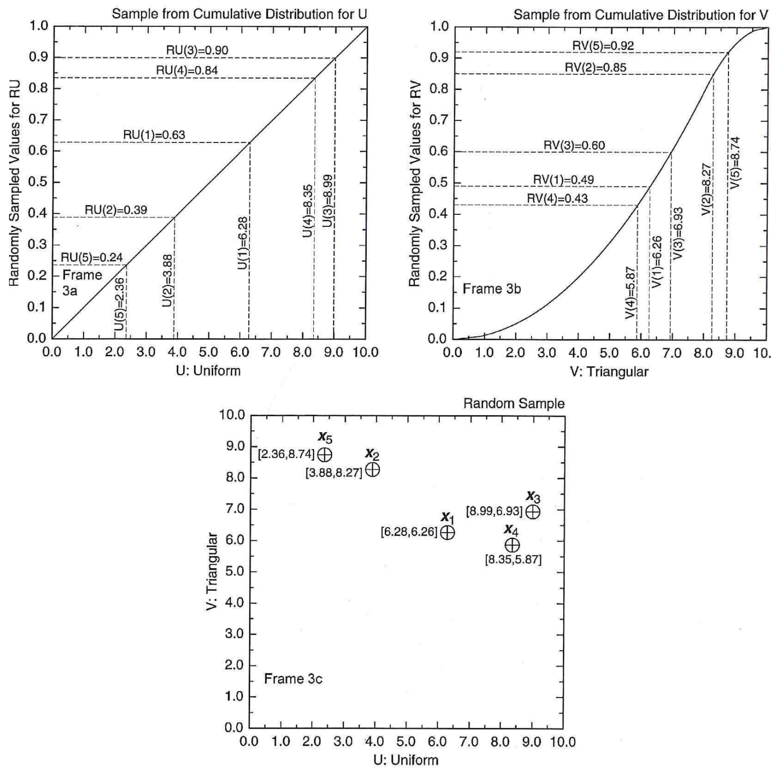

Figure 3-2: Generation of 5 Monte-Carlo samples from x = [U V] with U having a uniform distribution and V having triangular distribution with mode 8 on [0,10] [6].

3-2-2 Latin Hypercube Sampling

The Latin hypercube sampling (LHS) technique is an improved version of the Monte-Carlo sampling approach. In LHS a weight is associated with each sample that ensures that the entire range of uncertain input variables are represented. The technique is similar to the Monte-Carlo approach described in the previous section. Instead of directly generating random samples between the bounds as in Monte-Carlo sampling, the range of the input variables are divided into intervals of equal probability before the samples are generated in LHS. Figure 3-3 illustrates 5 samples generated using the LHS technique. The range of the input variables U and V are first divided into 5 sections of equal probability and then a value of U and V is chosen from each section. Samples are then generated by randomly pairing the values of U and V. Figure 3-3 shows two possibilities of pairing U and V. Thus LHS ensures random sampling and complete representation of the range of the variables. This makes LHS sampling require lesser samples than Monte-Carlo sampling for the same accuracy in the response function statistics.

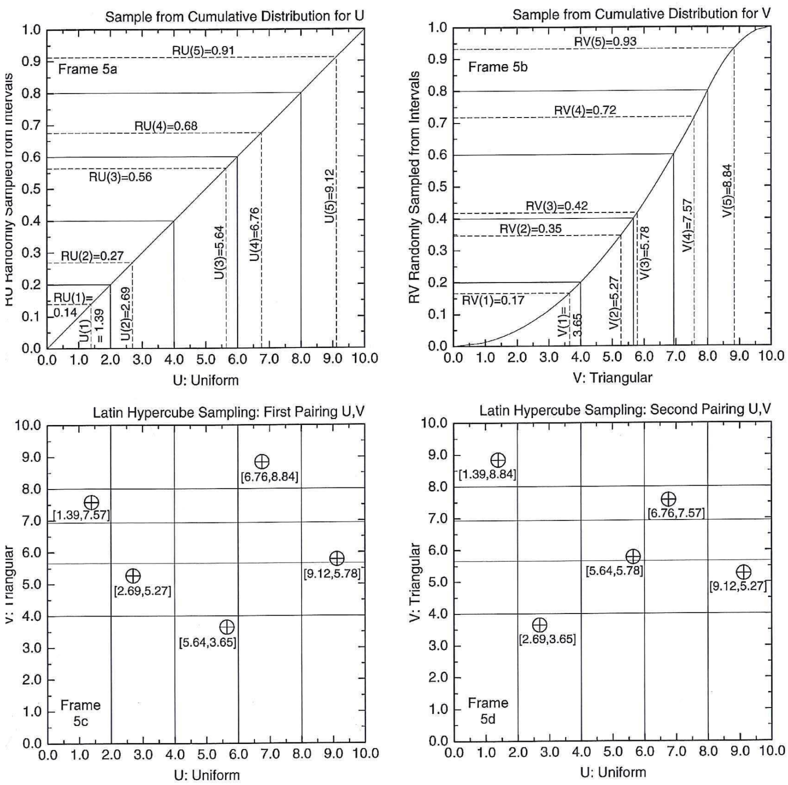

Figure 3-3: Generation of 5 Latin hypercube samples from x = [U V] with U having a uniform distribution and V having triangular distribution with mode 8 on [0,10] [6].

3-3 Sensitivity Analysis

Sensitivity analysis techniques are used in UQ to quantify the influence of each parameter and identify parameters that have the largest influence on the quantity of interest. The results from a sensitivity analysis can be used in optimizing the input parameters to reduce the uncertainty in them and eliminate input parameters that have the least influence on the results to reduce the computation time for performing an UQ study. Sampling based methods for sensitivity analysis are widely used [26]. One such method, the Variance based decomposition is evaluated and discussed in the next subsection.

3-3-1 Variance Based Decomposition

Variance-based Decomposition (VBD) is a global sensitivity method that estimates the influence of each parameter to the total uncertainty of the model. The Analysis of Variance (ANOVA) is a VBD technique. In the ANOVA method, influence of the parameters on the response function is determined by calculating two sensitivity indices, the main effect and the total effect. The main effect index gives the fraction of uncertainty in the model which is caused due to each input parameter. The total effect index corresponds to the fraction of uncertainty in the response function that is attributed to a input parameter and the interaction of this parameter with the other input parameters. The main effect (S_i) and the total effect (T_i) indices are computed from the variance of the quantity of interest as,

$$S_i = \frac{Var_{x_i}[E(Y|x_i)]}{Var(Y)}$$

$$T_i = \frac{Var(Y) - Var[E(Y|x_{-i})]}{Var(Y)}$$

In the above equations, $Y = f(x)$ is the quantity of interest and x_i are the uncertain input parameters. A large value of S_i indicates that the parameter has a large influence on the response function. The sum of the main effect indices can be equal to 1 or less than 1. A value much less than 1 indicates significant higher order interactions that affect the variance [17]. VBD technique is computationally intensive as the samples need to be replicated to calculate the variance and hence the indices. For N samples and I uncertain input parameters, the VBD method requires $N(I+2)$ evaluations. Evaluation of a few hundred or thousand samples gives reasonable output statistics [17].

3-4 Uncertainty Quantification Analysis

3-4-1 Sources of Uncertainty

The equation of states used to describe the behaviour of fluids depend on parameters like the critical temperature and critical pressure. As explained in Section 2-3-3 and shown in Figure 2-7, at high temperatures and pressures close to the critical point, the variation of thermodynamic properties are complex and non-linear. Thus, the determination of these properties experimentally is challenging especially for large molecules (see Ref. [22], [27]) as highly accurate measurement devices are required to capture these non-linear effects and estimate the critical point values. In the absence of experimental data, analytical estimation methods like the group contribution methods (see Ref. [22]) are used. However, these are based on co-relations obtained through regression analysis whose accuracy is limited by approximations made, round off error etc. The acentric factor is defined in terms of the critical point properties as seen in Equation 2-33. Thus, uncertainty in the critical pressure directly influences the accuracy of the acentric factor.

Apart from the thermodynamic parameters, the other uncertain parameters are the flow turning angle and the operating conditions. The model placed in the test set-up as explained in Section 2-4 is manufactured according to the specified dimensions. Manufacturing always introduces an uncertainty which could be attributed to several factors such as errors in the manufacturing tool, wear in the cutting tool, human errors and so on. Manufacturing uncertainties cannot be eliminated [5]. They are taken into account by specifying a tolerance which is the maximum allowable deviation in the dimensions of the manufactured product. The operating conditions i.e. the pressure and temperature at the nozzle inlet depend on the design of the control system and the settling chamber. Any fluctuations in the output of the control system or a poorly designed settling chamber would introduce some uncertainty in the operating conditions of the set-up.

Table 3-1 provides the value of the uncertainty in all the input parameters used in this study. The percentage deviation of the acentric factor and κ_1 terms from the nominal are assumed because no data on their uncertainty could be found. The validity of this assumption is checked by repeating the simulations with a higher value of uncertainty percentage. By observing no significant contribution from these parameters it can be assumed that an uncertainty of 5 % is good enough to obtain reliable output statistics. The coefficients of the ideal gas isobaric heat capacities have large uncertainty values as compared to the other parameters because they are calculated using methods which are not specifically designed for siloxanes [28]. The deviation in the operating conditions is estimated such that the expansion of the fluid does not enter the two phase region and also respects the constraints on the ORCHID test facility.

In addition to the uncertainty values, all parameters are assumed to have a uniform distribution within the limits of the lower and upper bounds. This is chosen due to the lack of information available about the parameter distribution.

Table 3-1: Uncertainty percentage and bounds of fluid dependant parameters, geometric parameter and operating conditions.

Parameter	Uncertainty (%)	Lower bound	Nominal	Upper bound
Critical temperature [°C]*	±3 [29]	238.232	245.600	252.968
Critical pressure [bar]*	±5 [29]	18.424	19.394	20.363
Acentric factor [-]+	±5	0.398	0.419	0.440
κ_1+	±5	-0.055	-0.053	-0.050
Cp_{01}*	±15 [19]	44.110	51.894	59.678
Cp_{02}*	±15 [19]	630.139	741.340	852.541
Cp_{03}*	±15 [19]	-478.515	-416.100	-353.685
Cp_{04}*	±15 [19]	59.500	70.000	80.500
Flow turning angle [°]#	±0.01	19.998	20.000	20.002
Operating temperature [K]#	±1	519.899	525.150	530.402
Operating pressure [bar]#	±0.1	18.382	18.400	18.418

* Experimental + Assumed # Calculated

3-4-2 Results and Discussion

Figure 3-4 gives an overview of the UQ analyses performed. Two different situations are simulated depending on the position of the wedge. In the first situation, the wedge is placed at the exit of the nozzle and in the second situation, close to the throat as shown in Figure 3-5. The method used to determine the position of the wedge within the nozzle is explained in Section 3-4-2-2. Attributed to the position of the wedge the two situations also differ in the thermodynamic region in which the wedge is placed. At the exit of the nozzle the conditions are predominantly ideal whereas close to the throat, the thermodynamic region shows appreciable deviation from the ideal gas law as seen from Figure 2-11. An analysis of these two situations would provide a deeper insight into the influence of real gas effects on shock wave properties.

For each situation, two cases are considered. The first case is simulated by considering the uncertainties in the fluid dependant and the geometric parameters and the second case by considering the uncertainties in all the parameters including the operating temperature and pressure. Additionally all the simulations are performed by maintaining a constant Mach number in front of the shock wave. For the wedge at the exit of the nozzle, this is achieved by using an iterative procedure which varies the back pressure while for the wedge at 7.8 mm from the throat, a constant Mach number is specified such that the shock wave does not detach. Such an analysis is appropriate since the shock wave properties are functions of the upstream Mach number and the parameters listed in Table 3-1. Thus by maintaining a constant Mach number and varying the input parameters, the affect of the uncertainites on the shock wave can be effectively studied. Moreover, this method is suitable for a robust nozzle design as it would clearly indicate the deviation in the nozzle profile due to the uncertain input parameters. In contrast, an analysis with a constant back pressure would be better from an experimental point of view where the nozzle design is fixed. However this is out of scope of this study and is not considered. A description of the method with all the relevant

MATLAB functions used in performing the analysis is provided in Appendix D. The results obtained from the simulations for all the cases are presented and explained in the following section.

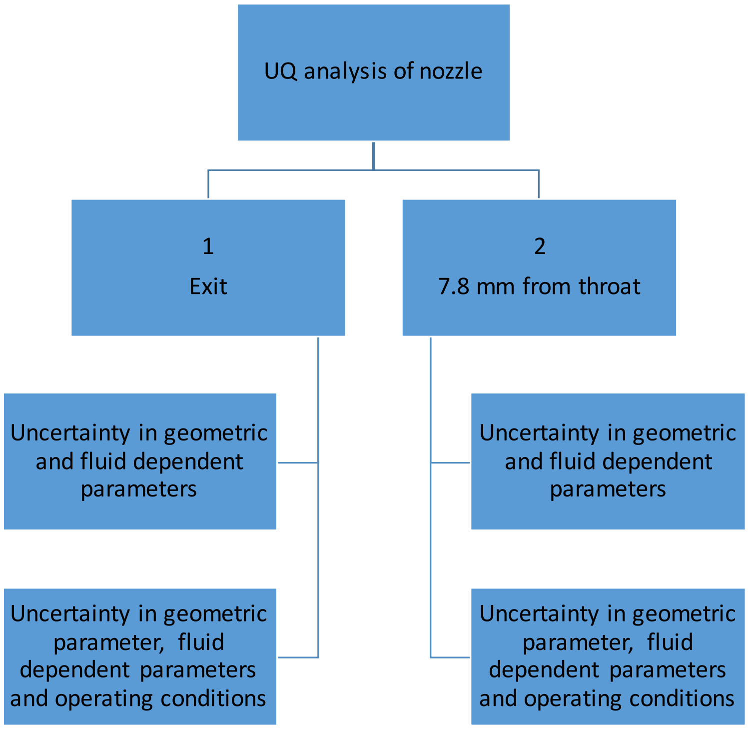

Figure 3-4: Overview of the UQ analysis of the nozzle performed in this study.

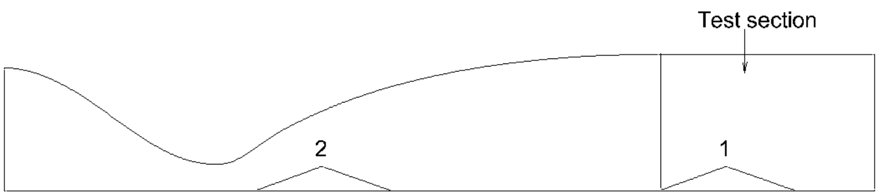

Figure 3-5: Location of the model in the nozzle.

3-4-2-1 Wedge at the Exit of the Nozzle

The Euler shock wave simulator code explained in Section 2-2-1 and Appendix A is coupled with DAKOTA to perform the UQ analysis to study the affect of the uncertainties in the parameters on the shock wave angle and shock wave intensity when the wedge is placed at the exit of the nozzle. Figure 3-6 shows the flow diagram of the method employed which starts from the creation of samples using the Monte-Carlo approach. Random samples of the input parameters are created depending on the uncertainty bounds prescribed. During each iteration, a set of input parameters are copied to a parameter file which is an input to the Euler shock wave simulator code. The simulation results from the code are written to a results text file which are then analysed to check for convergence. If the solution is converged then the results are post processed to obtain the uncertainties in the output values. In case the solution is not converged more samples are created and the process is repeated until convergence is achieved.

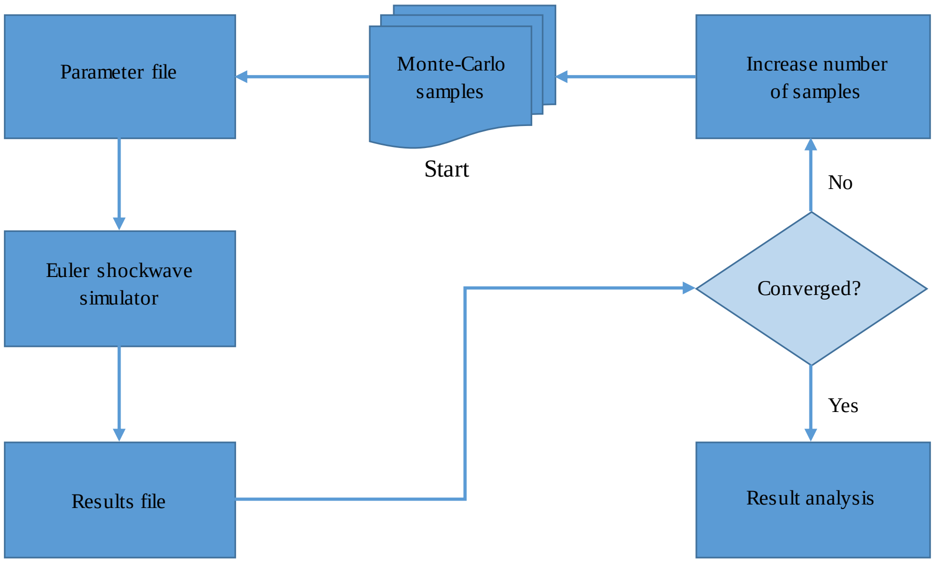

Figure 3-6: Working of the UQ method coupled with the Euler shock wave simulator code.

Case I: UQ analysis with deviation in the fluid dependent parameters and geometric parameter

Convergence Study

A UQ analysis is performed by considering the fluid dependant parameters and the geometric parameter as the uncertain variables. An initial sample size of 20000 is considered for performing the convergence study. The results of the convergence study are shown in Figure 3-7. The variation in the mean and the variance of the shock wave angle and the shock wave intensity is negligible after 15000 samples as seen from the flat profile in the figure. Thus a sample size of 15000 is deemed sufficient for performing further analysis. The value of the variance in the shock wave properties are small as observed from Figure 3-7 (b) and (d). This suggests that the deviation of these properties from the mean is negligible and that the shock wave angle and the shock wave intensity are affected to a lesser extent by the uncertainties in the input parameters.

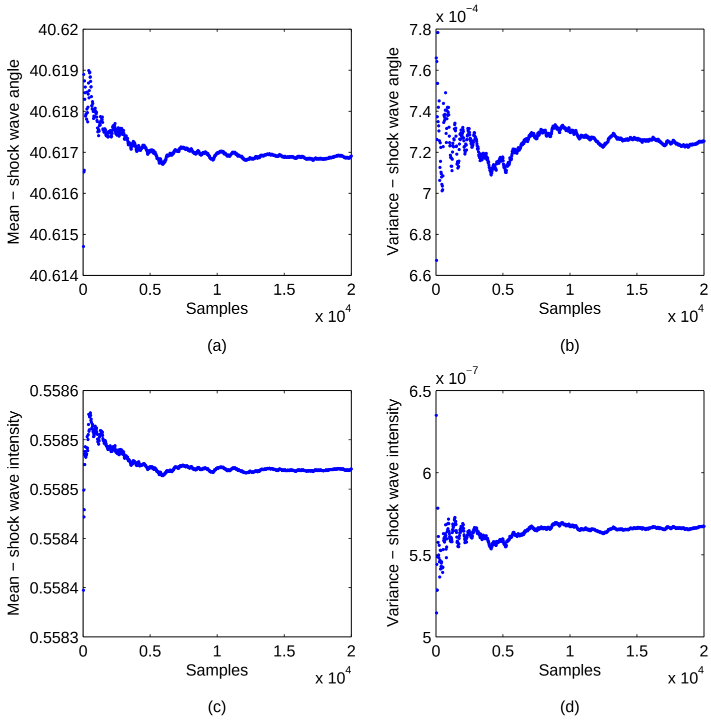

Figure 3-7: Convergence study of the shock wave angle and shock wave intensity due to deviations in the fluid dependant parameters and geometric parameter.

Sensitivity Analysis

A sensitivity analysis is performed to determine the dominant parameters that affect the shock wave angle and the shock wave intensity at the exit of the nozzle. The results from the analysis are presented in the form of a bar graph in Figure 3-8. As mentioned in Section 3-3-1, the variance based decomposition method is computationally intensive. Therefore, performing a sensitivity analysis with 15000 samples would result in a large computation time of about 10 days. Thus to save time, a sample size of 5000 is considered for performing the analysis. This would still result in satisfactory output statistics [17].

The results indicate that the critical temperature and the critical pressure are the most dominant parameters that influence the shock wave angle and the shock wave intensity while the other parameters have a marginal influence. Some of the parameters have a negative influence percentage since the simulations are not converged at 5000 samples. The large influence of the critical point properties is expected since the parameters in the iPRSV EoS as seen from Equations 2-28 and 2-29 depend on these critical properties. On substituting the a and b parameters and expanding Equation 2-27, the critical temperature and the critical pressure are found to have power terms. Therefore even a small variation in these properties affects the EoS to a large extent as compared to the other parameters. In addition, the critical temperature is also used in calculating the reduced temperatures in Equations 2-30 and 2-31. Thus a variation in the critical temperature affects all the parameters of the EoS and hence it is the most dominant parameter.

According to the thermodynamic cycle analysis performed by *Head et. al.* [1], reduced temperature at the inlet of the nozzle is 1.012. Since $T_r > 0.7$, Equations 2-30 and 2-31 reduces to [8]

$$\kappa = \kappa_0$$
$$\alpha = [1 + \kappa_0(1 - \sqrt{T_r})]^2$$

Therefore the κ_1 parameter is excluded from the EoS and hence its effect is negligible. Since the reduced temperatures are close to 1, the influence of the κ_0 term on the α function is minimal. The κ_0 term is a function of the acentric factor as shown in Equation 2-32. Thus the acentric factor has a marginal effect on the α function and hence on the EoS. Thus the acentric factor does not influence the shock wave properties. The variation in θ is small and is found to have negligible influence on the output.

From the sensitivity analysis results, the acentric factor and κ_1 term which are the assumed parameters and the flow turning angle θ are discarded from the final simulation.

The results of the sensitivity analysis performed with 15% variation in the acentric factor and κ_1 parameter are shown in Appendix E.

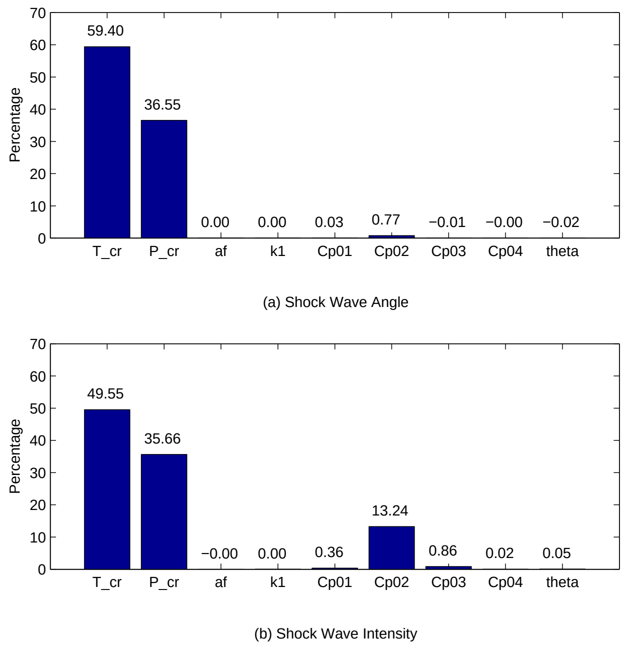

Figure 3-8: ANOVA analysis of the shock wave angle and shock wave intensity due to deviations in the fluid dependant parameters and geometric parameter.

Final Simulation Results

The final simulation is performed for a sample size of 15000. The back pressure varies by ± 0.05 bar due to the constant Mach number at the exit of the nozzle. The deviation in the shock wave angle and the shock wave intensity are depicted by Figures 3-9 and 3-10. As expected from the convergence study plots, the deviation from the mean are small. The shock wave angle deviates by 0.17% while the shock wave intensity by 0.06% from the mean value. These small deviation values indicate that the uncertainty in the input parameters have a negligible effect on the shock wave properties.

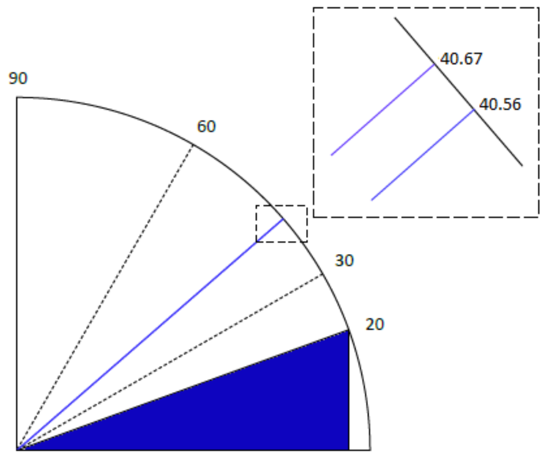

Figure 3-9: Variation in the shock wave angle due to uncertainty in the fluid dependant parameters and geometric parameter. The triangular region up to $20°$ represents the wedge placed at the exit of the nozzle. The dotted 30° and 60° lines are datum lines.

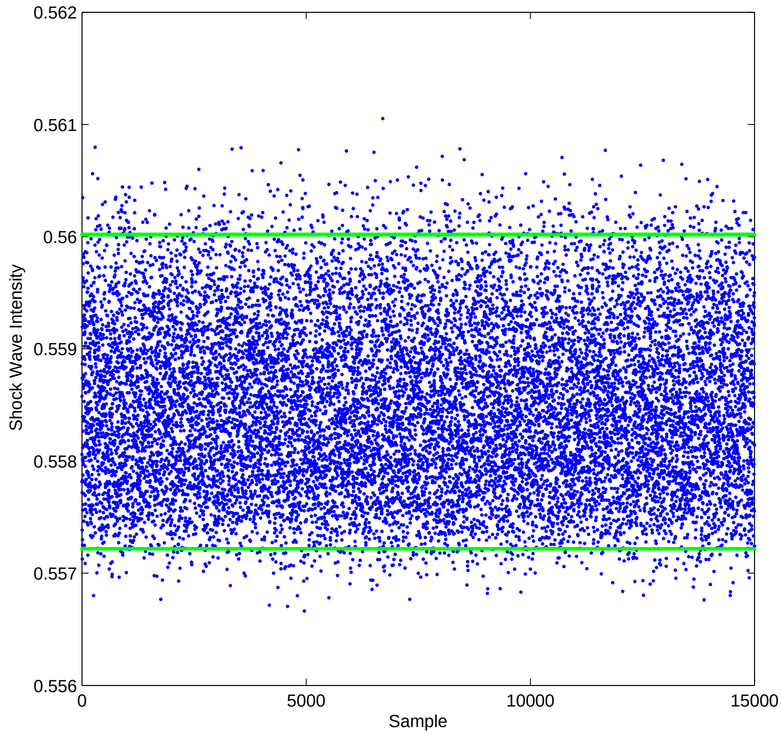

Figure 3-10: Variation in the shock wave intensity due to uncertainty in the fluid dependant parameters and geometric parameter. The green lines represent the bounds of the 95% confidence interval.

Case II: UQ analysis with deviation in the fluid dependant parameters, geometric parameter and operating conditions

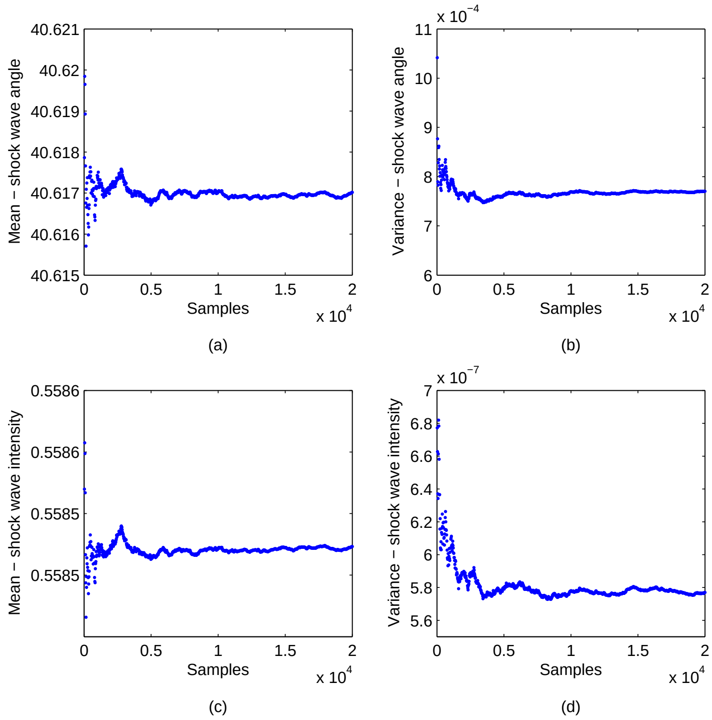

Figure 3-11: Convergence study of the shock wave angle and shock wave intensity due to deviations in the fluid dependant parameters, geometric parameter and operating conditions.

As explained in Section 3-4-1, the operating parameters in a wind tunnel set-up may be uncertain. Hence the UQ analysis is repeated by considering the variations in the operating parameters in addition to the fluid dependant and the geometric parameters. Figure 3-11 shows the results obtained from the convergence study. The mean and the variance of the shock wave angle and the shock wave intensity is plotted against the number of samples for a sample size of 20000. The plots show that the simulation is converged after 15000 samples. The variance in the shock wave angle and intensity are small, similar to the first case. Hence the deviation in the shock wave angle and intensity is expected to be less.

Sensitivity Analysis

Figure 3-12 shows the results obtained from the sensitivity analysis. As seen the second coefficient of the ideal gas isobaric heat capacity, Cp02 has the highest influence. Due to a change in the inlet temperature and pressure the enthalpy of the fluid changes which causes a change in the C_P of the fluid. To check the influence of the variation in the temperature on coefficients of C_P^{ig}, Equation 2-34 is differentiated with respect to the temperature which results in

$$\frac{dC_P^{ig}}{dT} = \underbrace{Cp_{02} * 10^{-3}}_{I} + \underbrace{2T(Cp_{03} * 10^{-6})}_{II} + \underbrace{3T^2(Cp_{04} * 10^{-9})}_{III} \tag{3-1}$$

Table 3-2: Values of the 3 terms of Equation 3-1 for nominal values of the coefficients of the ideal gas isobaric heat capacity and operating temperature.

Term	Value
I	0.741
II	-0.437
III	0.058

On substituting the values of the coefficients and the operating temperatures, it is seen that the first term $Cp_{02} * 10^{-3}$ has the highest value. As an example, Table 3-2 shows the values of the three terms for nominal values of operating temperature and coefficients of C_P^{ig}. Thus Cp_{02} has the highest influence as compared to the other coefficients.

The critical temperature and pressure have considerable affect on the shock wave properties while the acentric factor and κ_1 term have negligible influence as explained in the sensitivity analysis results of the previous case. The variation in the operating pressure as seen from Table 3-1 is less. They are not used in any of the coefficients in the iPRSV EoS and hence their effect is negligible. Temperature T_1 affects the specific heat thus influencing the results. Therefore, the final simulations are performed by considering the coefficients of C_P^{ig}, the critical point parameters T_{CR} and P_{CR} and the operating temperature T_1 as the uncertain inputs.

The results of the sensitivity analysis performed with 15% variation in the acentric factor and κ_1 parameter are shown in Appendix E.

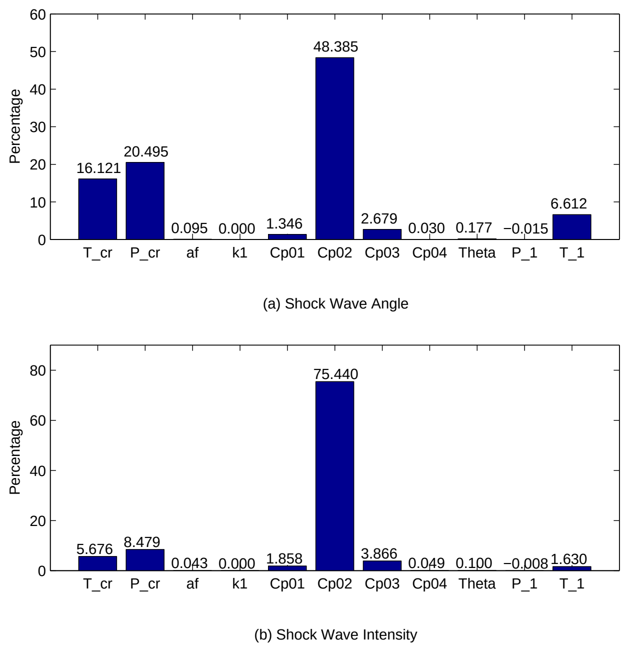

Figure 3-12: ANOVA analysis of the shock wave angle and shock wave intensity due to deviations in the fluid dependant parameters, geometric parameter and operating conditions.

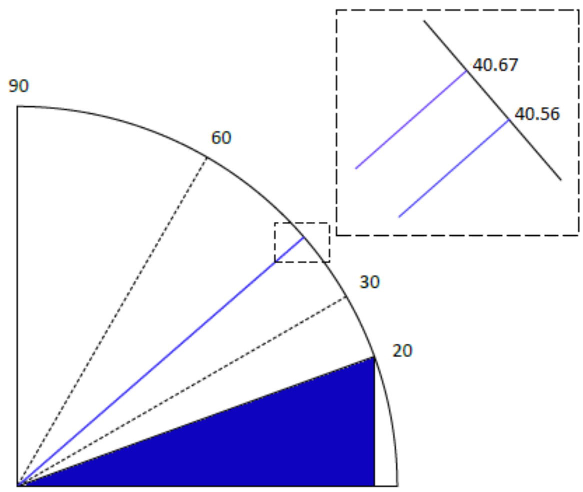

Figure 3-13: Variation in the shock wave angle due to uncertainty in the fluid dependant parameters, geometric parameter and operating conditions. The triangular region up to $20°$ represents the wedge placed at the exit of the nozzle.The dotted 30° and 60° lines are datum lines.

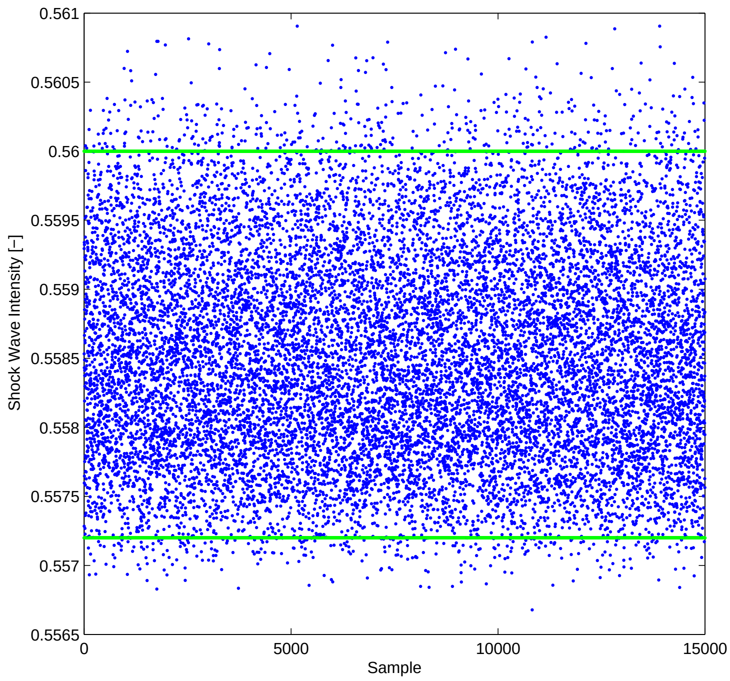

Figure 3-14: Variation in the shock wave intensity due to uncertainty in the fluid dependant parameters, geometric parameter and operating conditions. The green lines represent the bounds of the 95% confidence interval.

Final Simulation Results

Figures 3-13 and 3-14 represent the results obtained form the UQ analysis with the non-influential parameters discarded from the simulations. The deviations observed in the shock wave properties are similar to the ones obtained from the previous case. The shock wave angle varies by $\pm 0.17\%$ and shock wave intensity by $\pm 0.06\%$. Thus by considering the operating conditions, the most influential parameter changes while the deviations in the shock wave properties remain unchanged.

The two cases simulated above show that the uncertainties in the parameters have negligible effect on the on the shock wave properties when the wedge is placed at the exit of the nozzle. This indicates that in the ideal gas region the deviations in the input parameters have a negligible influence on the compressible flow phenomena. The results also demonstrate that the real gas region close to the throat of the nozzle does not influence the shock wave characteristics downstream of the nozzle.

3-4-2-2 Wedge placed at 7.8 mm from the throat

The method of characteristics is used to estimate the deviation in the nozzle profile and compressible flow phenomena when a model is placed close to the throat of the nozzle in a region which shows appreciable real gas effects. A description of the method is provided in Figure 3-15. The procedure is similar to the one explained in Section 3-4-2-1 except for the MoC which is coupled with the Euler shock wave simulator code and the samples created using the LHS approach. The values of the velocity, density and pressure in front of the shock wave are the inputs to the Euler shock wave simulator code as seen from Appendix A. In the region close to the throat of the nozzle, these values are obtained from the MoC and hence its use in the simulations is mandatory.

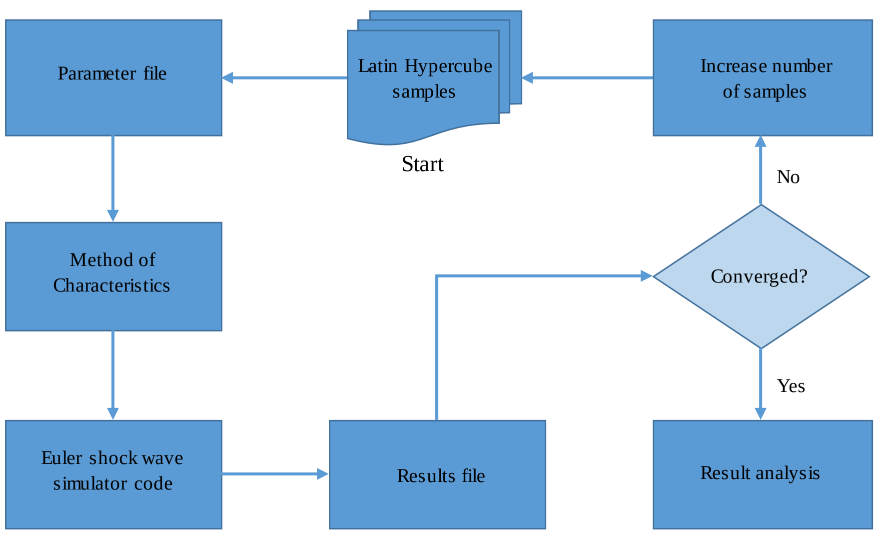

Figure 3-15: Working of the UQ method coupled with MoC and the Euler shock wave simulator code.

The exact position of the wedge is determined by plotting the $\theta - \beta - M$ diagram for three different Mach numbers and finding the Mach number at which the shock wave detaches. Figure 3-16 shows the $\theta - \beta - M$ diagram for the different Mach numbers. From the figure, it is seen that at a Mach number of 1.55, the maximum value of flow turning angle is close to 22°. Some allowance is provided to ensure that the shock wave does not detach on changing the input parameters and hence the Mach number corresponding exactly to the maximum flow turning angle of 20° is not considered. Mach numbers less than 1.55 would lead to a detached shock wave or a bow shock which is undesired for the analysis and any experiments conducted. From this Mach number and the distribution of Mach number along the centreline of the nozzle obtained from the MoC, the exact position of the wedge is determined to be 7.8 mm from the throat and is indicated by the label 2 in Figure 3-5.

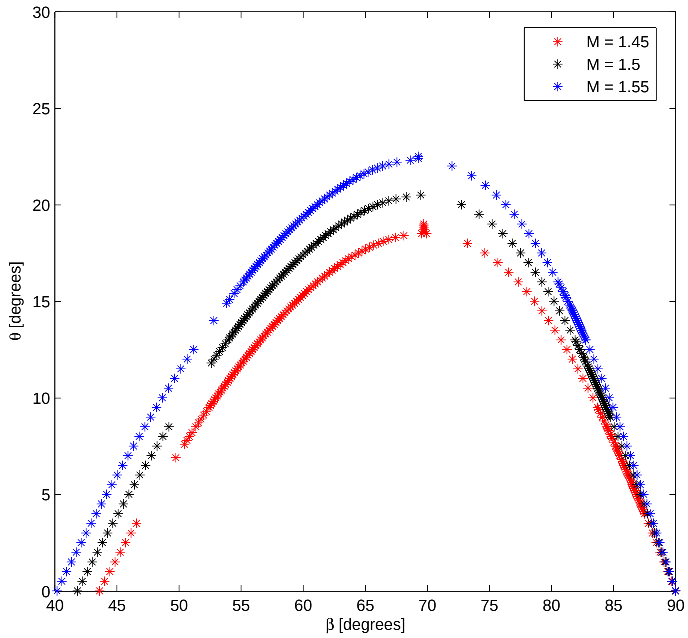

Figure 3-16: $\theta - \beta - M$ diagram for MM for upstream Mach numbers of 1.45, 1.5 and 1.55.

Table 3-3: Method of characteristics computation time and absolute deviation for different number of characteristic lines

Number of characteristic lines	Computation time [s]	Average absolute deviation [%] Pressure	Density	Velocity
50	1150	0	0	0
30	530	0.004	-0.04	0.006
20	200	0.009	-0.091	0.013
10	60	0.039	-0.39	0.055
5	20	0.17	-1.81	0.24

Table 3-3 presents the computation time and deviation of the centreline pressure, density and

Table 3-4: Deviation of the centreline pressure, density and velocity for five characteristics lines using different interpolation schemes with results from 50 characteristics lines as a reference.

Interpolation scheme	Pressure	Density	Velocity
Linear	0.17	-1.81	0.02
Spline	-0.02	0.01	-0.03
Pchip	-0.19	0.59	-0.03

velocity considering the results from 50 characteristics lines as the reference. The deviation is computed by linearly interpolating the values between the node points on the centreline for 5, 10, 20 and 30 characteristics obtained from MoC and comparing the results with the reference i.e 50 characteristics line. Since the MoC function will be executed multiple times to perform the UQ analysis, the main constraint is the computation time. Therefore five characteristic lines are chosen to save time. However this results in a large deviation in the computed properties as seen from Table 3-3. Hence different interpolation schemes are used to reduce these deviations. Three interpolation schemes available in Matlab: linear, spline and pchip are considered. Reference [30] provides details of the interpolation method.

Table 3-4 provides the deviation in the pressure, velocity and density computed along the centreline for 5 characteristics lines using different interpolation schemes. From the values, a linear interpolation scheme for velocity and spline interpolation for pressure and density is selected.

Performing sensitivity analysis using MoC was not feasible as the variance based decomposition method is computationally intensive as explained in Section 3-3-1. The simulation results obtained for the wedge located at 7.8 mm from the throat is discussed in the following section.

3-4-2-3 Case I: UQ analysis with deviation in the fluid dependant parameters and geometric parameter

Convergence Study

The first case is simulated by considering uncertainties only in the fluid dependant and the geometric parameters. Figure 3-17 shows the convergence plots obtained for a sample size of 9000. The flat profile in the statistics of the shock wave angle and the shock wave intensity indicate a converged solution. Larger values of variance in the shock wave angle and shock wave intensity (Figure 3-17 (b) and (d)) as compared to the cases discussed in the previous section indicate a larger deviation from the mean when the wedge is placed closer to the throat.

Final simulation results

The final simulation results are obtained by considering the uncertainty in all the parameters since a sensitivity analysis was not performed. Figures 3-18 and 3-19 show the deviation of the shock wave angle and the shock wave intensity. The mean value of the shock wave angle obtained is higher than that for the case when the wedge is placed at the exit of the nozzle. This is expected and can be seen from the Figure 3-16 that as the wedge is moved closer to the throat, for a flow turning angle of 20°, the shock wave angle increases. Also the deviation

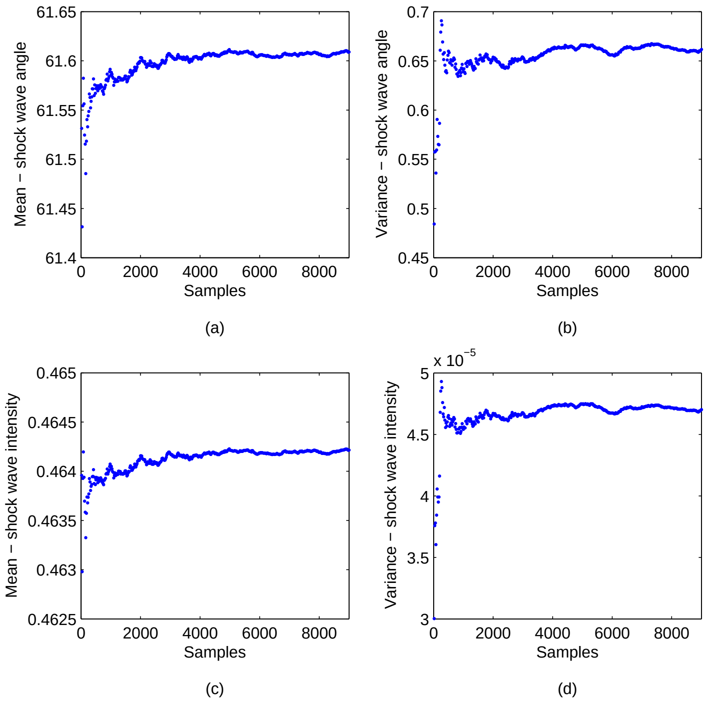

Figure 3-17: Convergence study of the shock wave angle and shock wave intensity due to deviations in the fluid dependant parameters and geometric parameter when the wedge is located a 7.8 mm from the throat of the nozzle.

in the shock wave angle from the mean is 2.2% which is much larger than the case discussed in the previous section. This indicates that as the real gas effect increases the uncertainty in the shock wave properties also increases. This is consistent with the observation made in Ref. [9]. In the real gas region, the effect of the uncertainties in the input parameters is amplified. The real gas region is characterized by high degree of non-linearity. Hence a small change in the parameters of the EoS leads to a large variation in the computed properties.

The mean value of the shock wave intensity is lower than the case when the wedge was placed at the exit of the nozzle. This indicates that the shocks are weaker. This is expected since the Mach number before the shock wave is smaller. Also the deviations in the shock wave intensity are 2.7% which is larger than for the case when the wedge is placed at the exit as explained above.

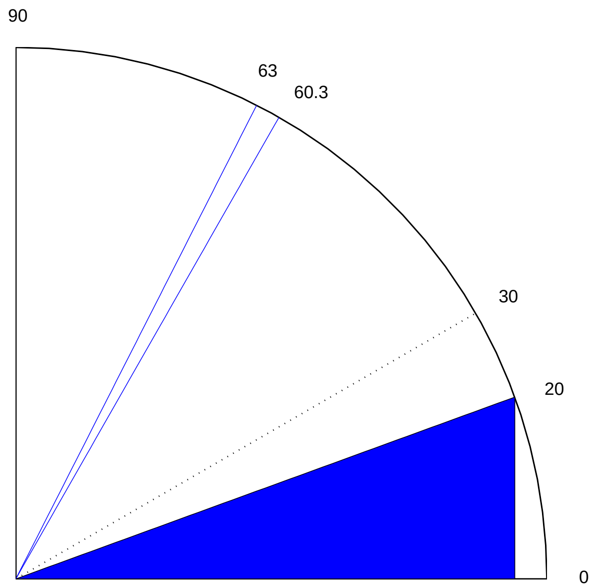

Figure 3-18: Variation in the shock wave angle due to uncertainty in the fluid dependant parameters and geometric parameter. The triangular region up to 20° represents the wedge placed at 7.8 mm from the throat of the nozzle. The dotted 30° line is a datum line.

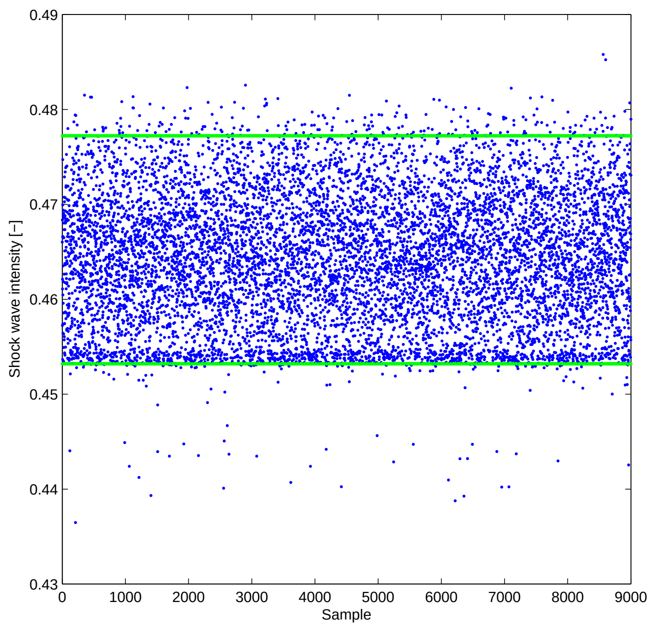

Figure 3-19: Variation in the shock wave intensity due to uncertainty in the fluid dependant parameters and geometric parameter. The green lines represent the bounds of the 95% confidence interval.

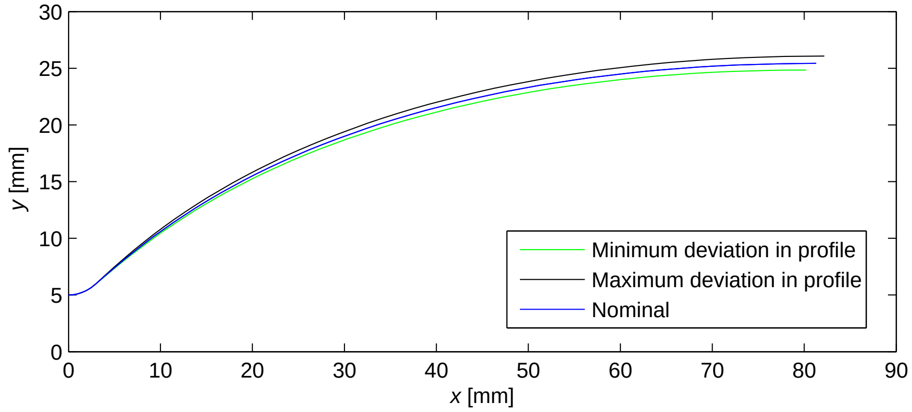

Figure 3-20: Variation in the dimensions of the nozzle due to uncertainty in the fluid dependant parameters and geometric parameter.

Figure 3-20 illustrates the deviation in the nozzle profile due to the uncertain input parameters. The compatibility equation (Equation 2-41) used in MoC depends on the velocity and the speed of sound. A variation in the thermodynamic parameters changes the speed of sound and hence causes a deviation in the computed Mach numbers. As explained in Section 3-4-2-2, the initial expansion flow field depends on the Mach number and determines the length of the nozzle. Thus a change in the input parameters varies this flow field causing a variation in the nozzle profile. Table 3-5 presents the coordinates of the exit of the nozzle and the average deviation in the nozzle height. This is calculated by determining the difference in nozzle height between the nominal and the case (maximum or minimum deviation) at the same x position. This procedure is repeated for several x coordinate values and the mean of all differences gives the average deviation. The deviations reported are substantial considering that the thickness of the boundary layer is around 1 mm [31]. The large deviations may be attributed to the fact that all the calculations are performed using 5 characteristics lines and the values of all properties and the nozzle coordinates are interpolated between them. This reduces the accuracy of the profile generated. Hence to obtain the exact deviations the simulations should be repeated by considering greater number of characteristic lines.

Table 3-5: Coordinates of the last point on the nozzle profile and average deviation of the profile from the nominal due to uncertainty in the fluid dependant parameters and geometric parameter.

Case	X coordinate	Y coordinate	Average deviation from nominal [mm]
Nominal	81.195	25.400	-
Maximum deviation	82.210	26.050	0.3216
Minimum deviation	80.895	24.810	-0.2681

3-4-2-4 Case II: UQ analysis with deviation in the fluid dependant parameters, geometric parameter and operating conditions

The second case is simulated by considering the uncertainties in all the parameters: fluid dependant, geometric and the operating conditions. Figure 3-21 shows the results from the convergence study. An initial arbitrary sample size of 11000 is considered. The plots of the mean and the variance of the shock wave angle and the shock wave intensity indicate that convergence is achieved with the initial sample size. The variance in the shock wave angle and the shock wave intensity is large as compared to the case when the wedge is placed at the exit (Section 3-4-2-1 Case II). This indicates a larger deviation in the shock wave properties.

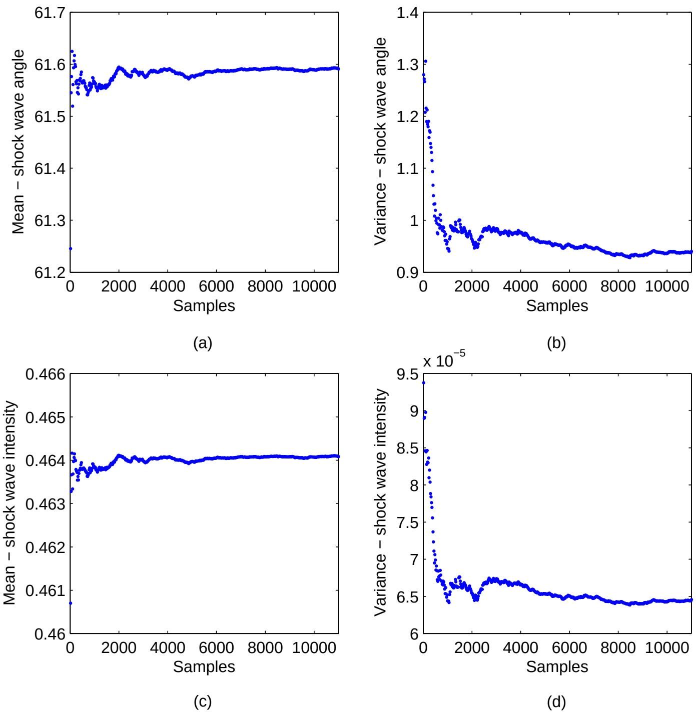

Figure 3-21: Convergence study of the shock wave angle and shock wave intensity due to deviations in the fluid dependant parameters, geometric parameter and operating conditions when the wedge is located a 7.8 mm from the throat of the nozzle.

Final Simulation Results

Figures 3-22 and 3-23 show the deviation in the shock wave angle and shock wave intensity due to variation in the fluid dependent parameters, geometric parameter and the operating conditions. The deviation in the shock wave angle is 2.6% while the shock wave intensity varies by 3.1% from the mean. These values are similar to the ones obtained from the previous case. Since a sensitivity analysis is not performed, the influence of the operating conditions on the results could not be quantified. However as seen from Section 3-4-2-1, the operating conditions could have a significant affect on the C_P of the fluid, since the operating temperatures are varied.

The deviation in the nozzle profile due variation in the input parameters is illustrated in

Figure 3-24. As explained in the previous case a deviation in the properties changes the speed of sound which causes a variation in the Mach number distribution thus causing the profile to deviate from the nominal. Table 3-6 reports the average deviation of the profile from the nominal.

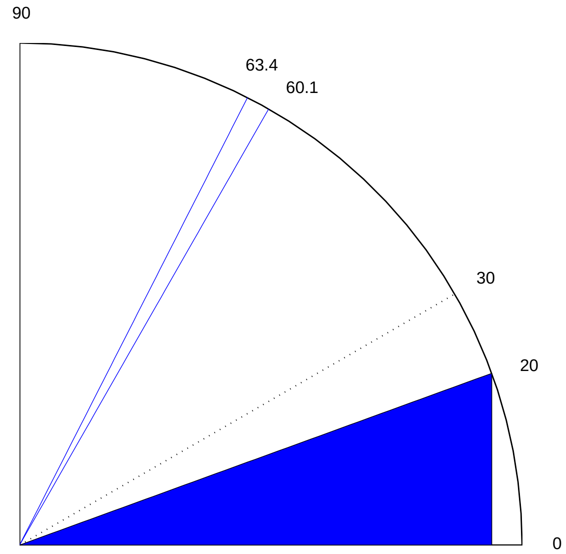

Figure 3-22: Variation in the shock wave angle due to uncertainty in the fluid dependant parameters, geometric parameter and operating conditions. The triangular region up to 20° represents the wedge placed at 7.8 mm from the throat of the nozzle. The dotted 30° line is a datum line.

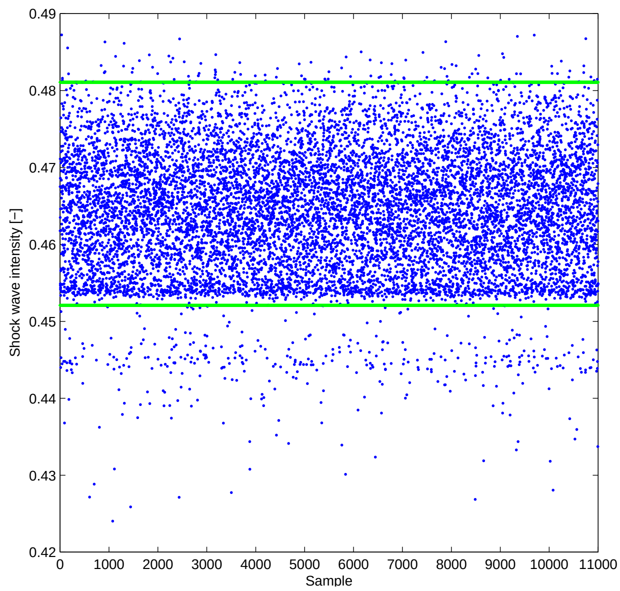

Figure 3-23: Variation in the shock wave intensity due to uncertainty in the fluid dependant parameters, geometric parameter and operating conditions. The green lines represent the bounds of the 95% confidence interval.

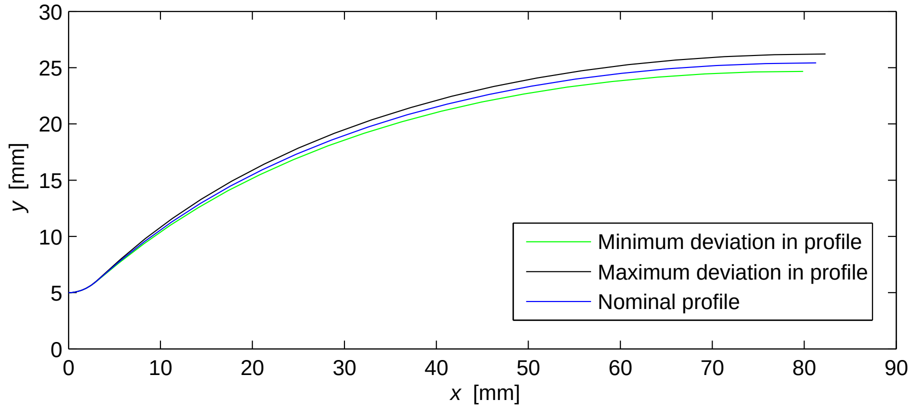

Figure 3-24: Variation in the dimensions of the nozzle due to uncertainty in the fluid dependant parameters, geometric parameter and operating conditions.

Table 3-6: Coordinates of the last point on the nozzle profile and average deviation of the profile from the nominal due to uncertainty in the fluid dependant parameters, geometric parameter and operating conditions.

Case	X coordinate	Y coordinate	Average deviation from nominal [mm]
Nominal	81.28	25.43	-
Maximum deviation	82.33	26.21	0.3115
Minimum deviation	79.89	24.67	-0.2601

Figure 3-25 provides a comparison of the deviations in the shock wave angle and the shock wave intensity obtained when the wedge is placed at locations 1 and 2 illustrated by Figure 3-5 for the cases I and II discussed in Sections 3-4-2-1 and 3-4-2-2. Thus from the results it is evident that in the region where the fluid shows significant deviation from the ideal gas law, the deviation in the shock wave properties is large. At the exit of the nozzle where the fluid is ideal, the deviations are less. This indicates that the real gas region upstream of the shock wave has negligible affect on the downstream properties. The values of the shock wave angle obtained from the UQ analysis are verified by performing CFD simulations which are discussed in the next chapter.

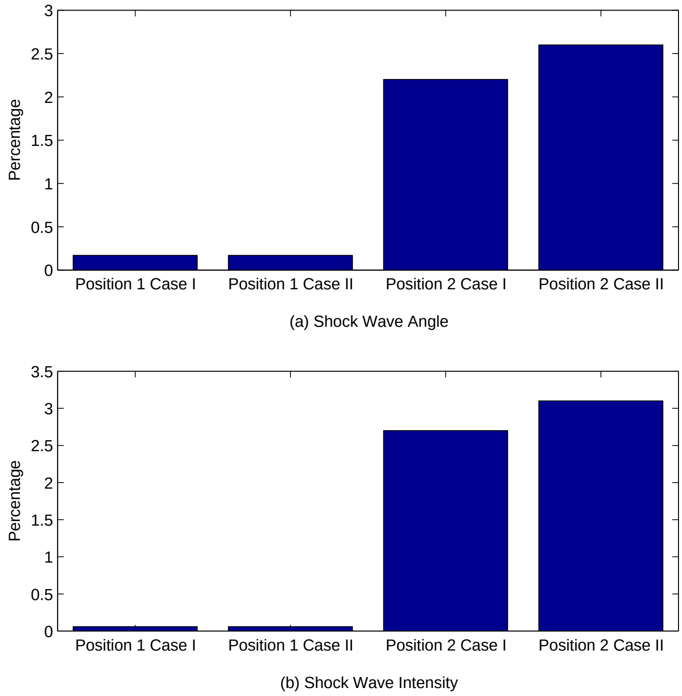

Figure 3-25: Deviation in the shock wave angle and the shock wave intensity when the wedge is placed at position 1 and 2. For case I the fluid dependant parameters and the geometric parameter are uncertain whereas for case II the operating conditions, in addition to the parameters considered in case I are uncertain.

Chapter 4

CFD Analysis

The previous chapter provided an introduction to uncertainty quantification and documented the results obtained from the UQ analysis performed on the nozzle for two different positions of the wedge. The current chapter verifies the result obtained from the low fidelity analysis by performing CFD simulations. Section 4-1 provides a brief introduction to RANS modelling. Section 4-2 discusses the results obtained from the CFD simulations of the nozzle. The present study can be extended to quantifying the influence of variation in the critical point values on the losses in a radial outflow turbine. Further details of this UQ analysis is provided in Section 4-3.

4-1 Reynolds-averaged Navier-Stokes (RANS) Modelling

The motion and properties of a viscous fluid can be completely described by the mass, momentum and energy conservation equations which are together termed as the RANS equations. The class structure of SU2 has been designed to solve partial differential equation systems resulting from the physical modelling of the problem of the form given below [32]:

$$\partial_t U + \nabla \cdot \vec{F}^c - \nabla \cdot \vec{F}^v = Q \tag{4-1}$$

where U represents the vector of state variables, $\vec{F}^c$ and $\vec{F}^v$ represent the convective and viscous fluxes respectively and Q is a generic source term. For transonic and supersonic flows, it is reasonable to assume the flow to be compressible owing to the high mach numbers. For such flows the RANS equations in terms of Equation 4-1 is obtained by replacing U with the vector of conservative variables, i.e $U = (\rho, \rho v_1, \rho v_2, \rho v_3, \rho E)^T$ where ρ is the density of the fluid, E is the total energy per unit mass, and $\vec{V} = (v_1, v_2, v_3)$ is the velocity in the Cartesian coordinate system along the X,Y and Z axis respectively. Using this definition of U, the convective and viscous fluxes are then given by

$$\vec{F}_i^c = \begin{pmatrix} \rho v_1 \\ \rho v_i v_1 + P\delta_{i1} \\ \rho v_i v_2 + P\delta_{i2} \\ \rho v_i v_3 + P\delta_{i3} \\ \rho v_i H \end{pmatrix}, \qquad \vec{F}_i^v = \begin{pmatrix} \cdot \\ \tau_{i1} \\ \tau_{i2} \\ \tau_{i3} \\ v_j \tau_{ij} + \mu_{tot}^* C_p \partial_i T \end{pmatrix}, \qquad i = 1, ..., 3 \tag{4-2}$$

In Equation 4-2, P is the static pressure, δ_{ij} is the Kronecker delta function, H is the fluid enthalpy and τ_{ij} are the viscous stresses given by the relation $\tau_{ij} = \mu_{tot}(\partial_j v_i + \partial_i v_j - \frac{2}{3}\delta_{ij}\nabla \cdot \vec{v})$. The total viscosity term μ_{tot}^* is a summation of dynamic viscosity and turbulent viscosity given as

$$\mu_{tot} = \mu_{dyn} + \mu_{tur}, \qquad \mu_{tot}^* = \frac{\mu_{dyn}}{Pr_d} + \frac{\mu_{tur}}{Pr_t}$$

where Pr_d and Pr_t are dynamic and turbulent Prandtl numbers respectively.

4-2 Nozzle

CFD simulations are carried out to verify the results obtained from the UQ analysis performed using the Euler shock wave simulator code and the MoC. The geometry of the nozzle used in the simulations is obtained from the MoC. The nozzle geometry is meshed using an in-house mesh generator software named UMG2 [33]. The density of the meshes is selected according to the results of a mesh sensitivity study documented in Ref. [31]. The CFD simulations are performed for three different cases. First an empty nozzle is simulated and the Mach numbers along the centreline obtained from MoC and CFD are compared. The other two cases are simulated by placing a wedge at the exit of the nozzle and at 7.8 mm from the throat. The resulting shock wave angles are then compared with the results shown in Section 3-4-2.

The following section gives a detailed description of the CFD simulations performed.

4-2-1 Empty Nozzle

Figure 4-1 shows the geometry along with the boundary conditions and a representation of the mesh for simulating the empty nozzle. The number of nodes and elements for different face spacing is shown in Table 4-1. The face spacing represents the distance between two successive nodes on the boundary of the geometry. As expected the number of nodes and elements increases as the mesh is made denser by decreasing the face spacing. From the results of the mesh study, a fine mesh is chosen having a face spacing of 0.3 to accurately simulate the flow in the empty nozzle.

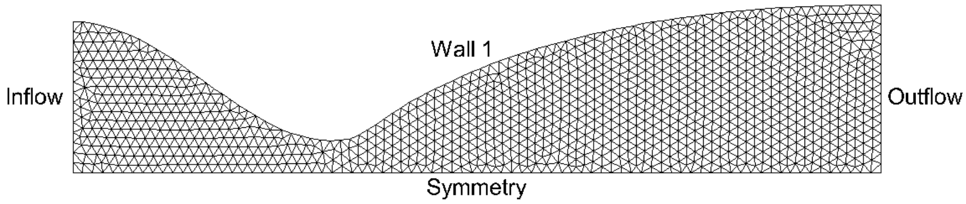

Figure 4-1: Mesh generated for an empty nozzle with mesh spacing of 1.5 along with the defined boundary conditions.

Table 4-1: Number of nodes and elements for meshes with varying face spacing.

Face spacing	Number of nodes	Number of elements
1.5	1202	2202
1.0	2653	5003
0.5	10469	20334
0.3	28970	56935

The initial conditions, boundary conditions and the solver settings are presented in Table 4-2. A steady state, Euler simulation is performed using the software SU2. The StanMix gas model is used to compute the thermodynamic properties of MM. The boundary conditions are in accordance with the operating conditions of the ORCHID set-up. Converged solutions are achieved with a CFL number of 1 and second order spatial discretisation.

Table 4-2: Initial and boundary conditions for simulating the flow in the empty nozzle .

Initial conditions	
Mach number	0.1
Freestream pressure [bar]	1500000.0
Freestream temperature [K]	525.15
Gas model	StanMix
Boundary conditions	
Inlet total pressure [bar]	18.4
Inlet total temperature [K]	525.15
Outlet static pressure [bar]	1
Solver settings	
CFL number	1
Spatial numerical order integration	Second order limiter
Time discretisation	Euler implicit

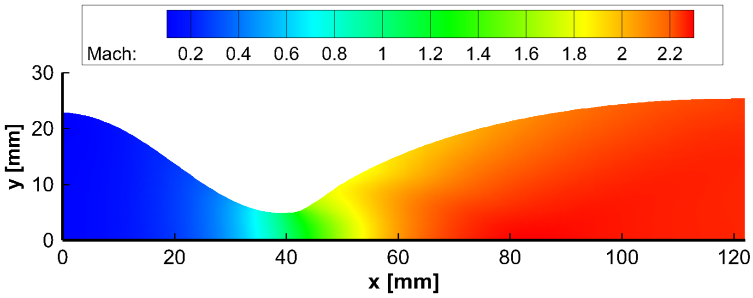

Figure 4-2: Contours of Mach number for the empty nozzle.

Figure 4-2 shows the contours of Mach number obtained from the simulation. The pressure differential across the nozzle drives the flow. As expected the Mach number of the flow in the nozzle increase along the nozzle length. The flow is initially subsonic with a Mach number 0.1 at the inlet. Sonic conditions are achieved at the throat and supersonic flow is induced in the diverging section of the nozzle. The average Mach number at the exit is 2.27 which is close to the design Mach number of the nozzle. A comparison is made between the centreline Mach numbers obtained from MoC with 50 characteristic lines and CFD. The results are presented in Figure 4-3. At lower Mach numbers the results from MoC and CFD are in good agreement. This verifies the use of MoC for performing analysis close to the throat where the real gas effects are appreciable. At the exit of the nozzle, CFD predicts a lower Mach number as compared to MoC. This could be due to insufficient number of characteristic lines used in MoC which leads to lesser number of nodes. The distribution of node points in MoC is much denser close to the throat as compared to the exit. This could lead to less accurate solutions predicted by the MoC at the exit.

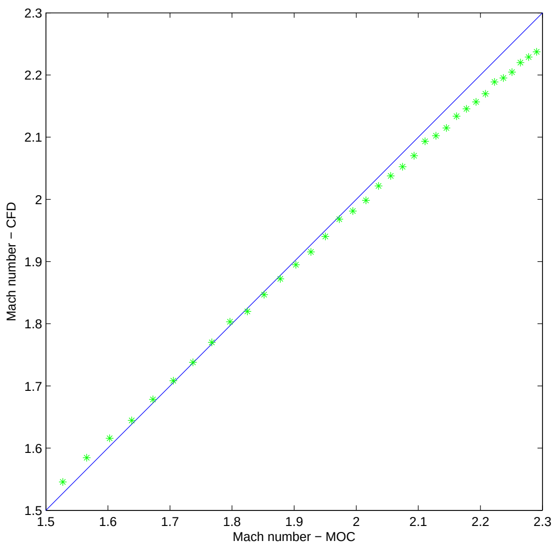

Figure 4-3: Comparison of Mach numbers along the nozzle mid line obtained from MoC and CFD for an empty nozzle.

4-2-2 Nozzle with Wedge at the Exit

CFD simulations are performed with the wedge placed at the exit of the nozzle. Three different cases are simulated by varying the parameters used in the iPRSV EoS. The first case is with the nominal values of all the fluid dependant parameters. The second and the third cases correspond to the maximum and minimum uncertainty in the shock wave angle obtained form the 1-D analysis. The fluid dependant parameters which lead to the maximum and minimum deviations are used and the resulting shock wave angles are determined. The results obtained from the 1-D analysis are verified by comparing them with the angles computed from the CFD results.

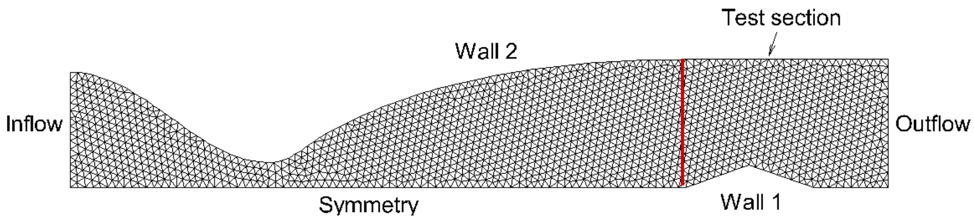

Figure 4-4: Mesh generated for a nozzle with the wedge at the exit with a mesh spacing of 1.5 along with the defined boundary conditions.

Figure 4-4 shows the geometry, boundary conditions and a representation of the mesh used. To determine the shock wave angle, a fine mesh is required so that a well defined oblique shock wave is generated from the tip of the wedge. The results from a mesh sensitivity study performed and documented in Ref. [31] indicates that a spacing of 0.35 or less leads to accurate solutions. Hence a mesh with a minimum possible spacing of 0.28 is chosen which results in 95057 elements and 48213 nodes. Except for the CFL number which is assigned a value of 0.5, the same initial conditions, boundary conditions and solver settings presented in Table 4-2 are used. Table 4-3 lists the values of the fluid dependant parameters used in simulating the maximum and the minimum deviation cases.

Table 4-3: Value of parameters used in simulating the maximum and minimum uncertainty case.

Parameter	Maximum uncertainty case	Minimum uncertainty case
Critical temperature [°C]	244.7332	247.7190
Critical pressure [bar]	20.1096	18.6770
Cp_{01}	45.4936	55.3631
Cp_{02}	645.8727	819.6586
Cp_{03}	-388.6682	-361.9593
Cp_{04}	74.8733	66.4481

Figure 4-5 shows the contours of Mach number with the attached oblique shock wave at the tip of the wedge for nominal values of the fluid dependant parameters. To determine the shock wave angle, a Matlab script is employed which locates the position of the jump in pressure on the nozzle wall and uses it to geometrically compute the angle. Figure 4-6 shows the variation of the pressure along the nozzle wall. The jump in the pressure indicates the location where the shock wave hits the nozzle wall. The coordinates of this point along with the coordinates of the tip of the wedge are used in determining the shock wave angle. The details of the Matlab function is provided in Appendix D. The contours for the cases with maximum and minimum deviation are similar to Figure 4-5 and hence are not shown. Table 4-4 shows the value of shock wave angle obtained from the different cases and their deviation from the Euler shock wave simulator results. As seen all the cases lead to a same value of shock wave angle. This indicates that the deviation in the shock wave angles are less and a finer mesh is required to capture these small deviations. Due to limitations of the mesh generator, generating a finer mesh than the one used could not be accomplished. Thus CFD verifies that the deviation in the shock wave angles are insignificant when the wedge is placed at the exit of the nozzle.

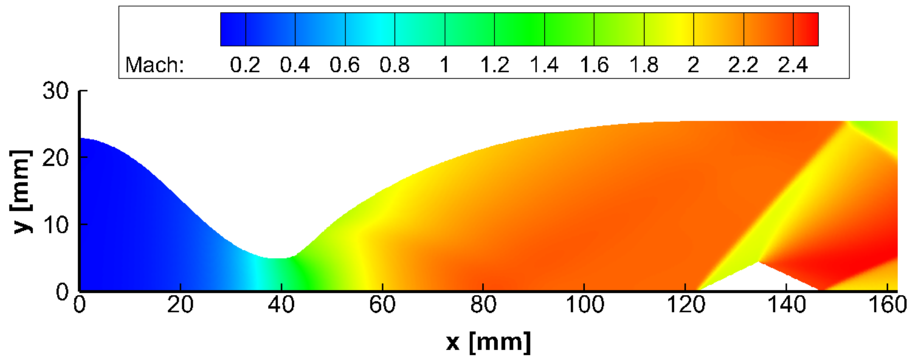

Figure 4-5: Mach number contour in a nozzle showing the shock wave generated at the tip of the diamond.

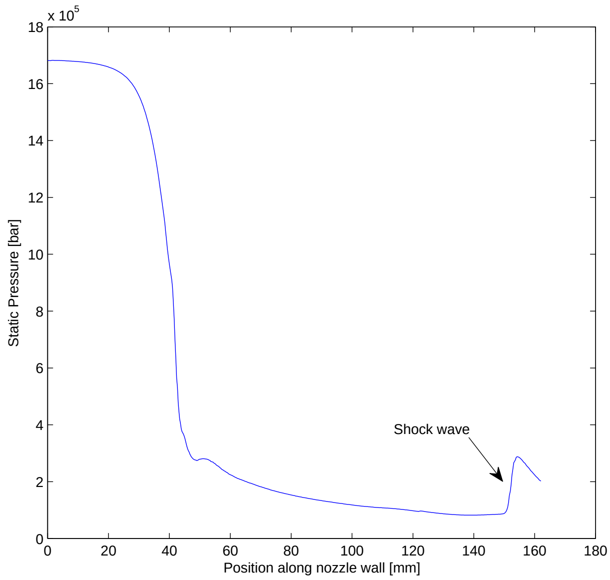

Figure 4-6: Variation of static pressure along the nozzle wall with the shock wave indicated for the case when the wedge is placed at the exit of the nozzle.

Table 4-4: Verification of results obtained from the Euler shock wave simulator for the nominal case and cases with maximum and minimum deviation in the shock wave angle.

Case	Euler shock wave simulator	CFD	Deviation [%]
Nominal	40.62	40.75	0.32
Maximum variation	40.67	40.75	0.2
Minimum variation	40.56	40.75	0.47

4-2-3 Nozzle with Wedge at 7.8 mm from the Throat

To verify the results presented in Section 3-4-2-2, three CFD simulations are performed corresponding to nominal, maximum and minimum deviation in the shock wave angle respectively. Figure 4-7 shows the geometry, with the boundary conditions and a representation of the mesh generated. As explained in the previous subsection, a fine mesh is required to accurately compute the shock wave angle from the CFD results. Hence a fine mesh is generated with a face spacing of 0.27 which divides the computational domain into 95063 elements having 48216 nodes. In addition, the simulations are performed by defining the same initial and boundary conditions as well as the solver settings as that of the previous case. Table 4-5 lists the values of the fluid dependant parameters used in simulating the maximum and minimum deviation cases. Variation of all parameters are considered since a sensitivity analysis was not performed for this case.

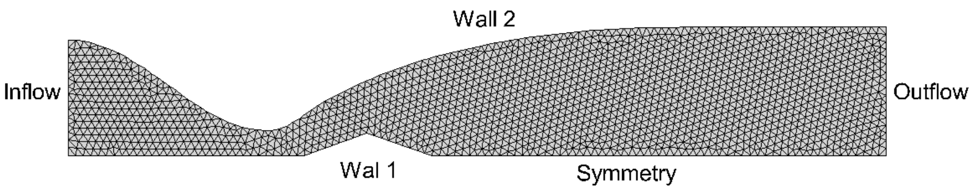

Figure 4-7: Mesh generated for a nozzle with the wedge located at 7.8 mm from the throat with a mesh spacing of 1.5 along with the defined boundary conditions.

Table 4-5: Value of parameters used in simulating the maximum and minimum uncertainty case.

Parameter	Maximum uncertainty case	Minimum uncertainty case
Critical temperature [°C]	240.6792	250.1165
Critical pressure [bar]	20.0449	18.8922
Acentric factor	0.4117	0.4173
κ_1	-0.0512	-0.0549
Cp_{01}	58.3148	58.0110
Cp_{02}	664.2128	659.75820
Cp_{03}	-395.1426	-457.3552
Cp_{04}	70.2411	70.4556

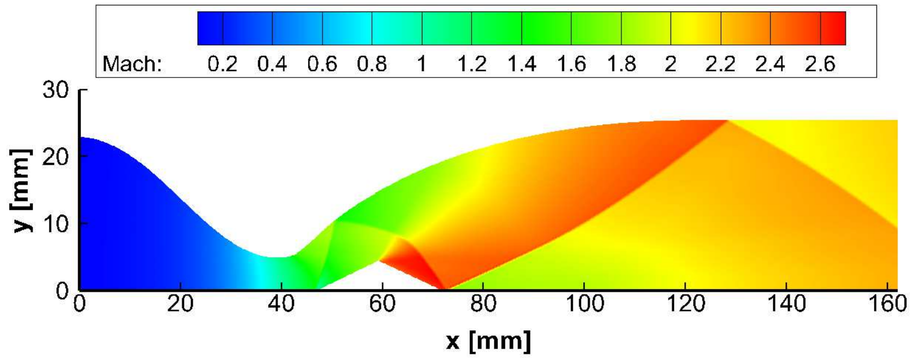

Figure 4-8: Mach number contour showing the shock wave generated at the tip of a wedge placed inside a nozzle.

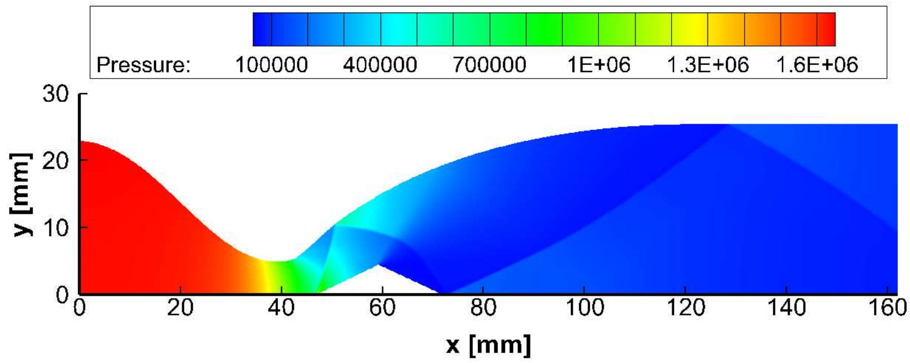

Figure 4-9: Static pressure contour showing the shock wave generated at the tip of a wedge placed inside a nozzle.

Figures 4-8 and 4-9 show the contours of Mach number and static pressure in the nozzle with the shock wave generated at the tip of the wedge. The shock wave bends slightly in the upstream direction due to its reflection from the nozzle wall [34]. Curved shock waves are generally formed when the Mach number in front of the shock wave is slightly greater than the minimum Mach number to have an attached shock wave [35]. From the contours, the shock wave angle is determined by constructing a tangent to the shock wave at the tip of the wedge. Figure 4-10 shows the variation of static pressure along the nozzle wall. A substantial rise in the pressure is observed at a distance of 50 mm on the nozzle wall which indicates the location where the shock wave hits the nozzle wall. A second oblique shock wave is generated from the trailing vertex of the wedge. The small jump in the pressure at a distance of 127 mm along the nozzle wall corresponds to the this shock wave impinging the nozzle wall.

Table 4-6 presents the comparison of the shock wave angles obtained from the UQ analysis performed using the MoC coupled with the Euler shock wave simulator and CFD. The results show an average deviation of 1.4% from the UQ analysis performed. This deviation is within permissible limits and hence verifies the results presented in Section 3-4-2-2.

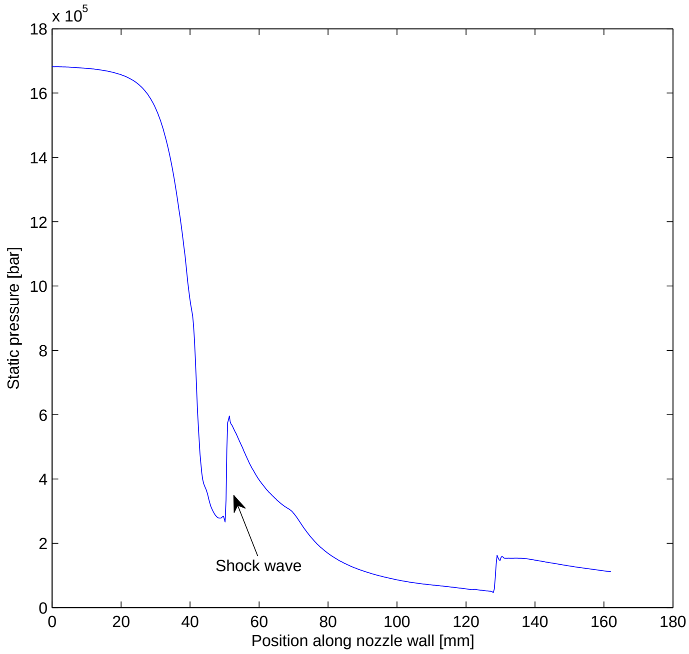

Figure 4-10: Variation of static pressure along the nozzle wall with the shock wave indicated for the case when the wedge is placed at 7.8 mm from the throat.

Table 4-6: Verification of results obtained from UQ analysis performed using the MoC and Euler shock wave simulator for the nominal case and cases with maximum and minimum deviation in the shock wave angle for the wedge at 7.8 mm from the throat of the nozzle.

Case	MoC and Euler shock wave simulator	CFD	Deviation [%]
Nominal	61.65	62.5	1.4
Maximum variation	63	64	1.6
Minimum variation	60.3	61	1.2

4-3 Turbomachinery

Turbomachines are devices that transfer energy to or from a continuously flowing fluid by the dynamic action of a set of moving blades [36]. Compressors, turbines, fans, pumps, etc. are examples of turbomachines. They can be broadly divided into two main categories: first, those that expand fluid to a low pressure to produce power (turbines) ; secondly, those that increase the fluid pressure by absorbing power (compressors, pumps). Turbomachines can also be categorised according to the flow path through the rotor as axial or radial. When the flow through the rotor is mainly along the axis, the machine is called as an axial flow turbomachine whereas when the flow is in a direction perpendicular to the axis i.e in the radial direction, the device is termed as a radial flow turbomachine.

In this study, a radial outflow turbine or centrifugal turbine is considered for the analysis. Radial outflow turbines are less popular as compared to radial inflow turbines primarily due to their less specific work output. However, for turbines working with organic fluids they have proven to be a viable technology [7], [20], [37]. A detailed description of the flow characteristics of a radial outflow turbine is provided in the next subsection.

4-3-1 Radial Outflow Turbine for ORC Applications

Expansion of organic fluids are characterized by high volumetric flow rates. In addition, the specific enthalpy drop of the fluids along the expansion line is less as they have high molecular weight. This would imply the use of axial or centripetal turbines having one or two stages to generate the power required [38]. However, the converging - diverging blade passages in these turbines combined with the low speed of sound of organic fluids leads to strong shocks at the blade outlet region affecting the performance of these machines. Moreover, ORC turbines often operate close to the critical point. These regions are characterized by complex thermodynamic behaviour further complicating the design of these systems. To overcome these difficulties, centrifugal or radial outflow turbines are used.

Figure 4-11 represents a schematic of a centrifugal turbine. The fluid enters the turbine close to the rotational axis and flows outward in a radial direction as shown in the figure. Such a configuration is advantageous since the flow path has a natural increase in area which can accommodate the rise in the volumetric flow rate. In addition, multi-stage arrangements of these turbines can be easily achieved [7]. Moreover, the low enthalpy drop of ORC turbines leads to low peripheral speeds which are generally within the mechanical stress limits [37]. Due to these reasons radial outflow turbines are considered as a viable option for use in ORC power systems.

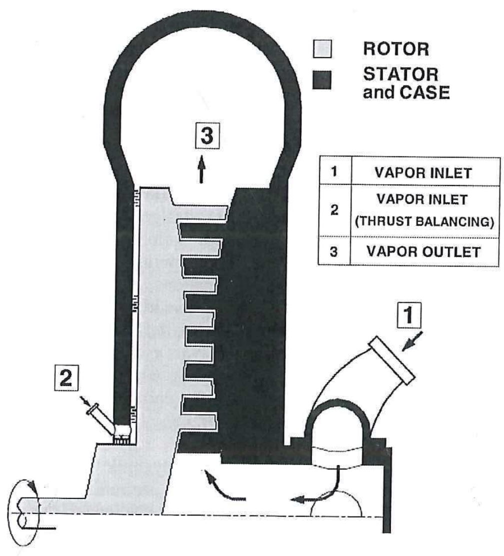

Figure 4-11: Centrifugal turbine schematic [7].

4-4 Effect of Uncertainty on Critical Pressure and Temperature in a Centrifugal Turbine

As seen from the analysis of flow in a nozzle in Section 3-4, the critical point properties have a significant influence on the shock wave properties. The analysis performed is extended in quantifying the losses in a radial outflow turbine. Losses occur in a turbine blade passage due to blade loading effects, leakage between the shroud and moving blade tip, boundary layer effects and for transonic blades, shock waves in the blade passages and tip of the trailing edge. These losses can be expressed in terms of the static enthalpy loss and is given by Equation 4-3. It is defined as the difference in the static enthalpy between the actual process and an isentropic process with the same pressure ratio, non-dimensionalized by a velocity term [39].

$$\zeta = \frac{h_2 - h_{2s}}{\frac{1}{2}W_{2s}^2} \tag{4-3}$$

where, h and W represent the specific enthalpy and the relative velocity respectively. The value of isentropic relative velocity at the exit is computed from the rothalpy as shown in Equation 4-4.

$$W_{2s} = \sqrt{2(h_1 + 0.5 * W_1^2 - h_{2s} + 0.5 * (U_2^2 - U_1^2))} \tag{4-4}$$

In the above equation, U refers to the local blade speed of the turbine.

To quantify the losses, the flow of MM in a turbine with an inlet pressure of 18.4 bar which is close to the critical pressure is simulated. At this pressure the flow in the turbine would be influenced by real gas effects. Nine cases depending on the variation in the critical pressure and temperature are considered and are shown in Table 4-7.

Table 4-7: The nine cases considered to study the influence of deviation in the critical pressure and temperature on static enthalpy loss.

Sr. No.	Deviation	
	Critical temperature	Critical pressure
1	Nominal	Nominal
2	Nominal	Maximum
3	Nominal	Minimum
4	Maximum	Nominal
5	Minimum	Nominal
6	Maximum	Maximum
7	Maximum	Minimum
8	Minimum	Maximum
9	Minimum	Minimum

The nominal, maximum and minimum deviation in the critical temperature and pressure are shown in Table 3-1 and repeated here for the convenience of the reader.

Table 4-8: Uncertainty percentage and deviation in the critical temperature and pressure of MM.

Parameter	Uncertainty [%]	Minimum deviation	Nominal	Maximum deviation
Critical temperature [°C]	±3	238.232	245.600	252.968
Critical pressure [bar]	±5	18.424	19.394	20.363

Figure 4-12 shows the 2D CFD domain with the boundary conditions for simulating the flow over a centrifugal turbine blade. The mesh generated using UMG2 is illustrated by Figure 4-13. The density of the mesh is controlled by specifying the spacing value. A dense mesh is generated at the leading edge and the trailing edge where shock waves are expected. A coarse mesh is generated in all other parts of the domain so that the shock waves are smoothed out by numerical diffusion [40]. For viscous simulations, a hybrid mesh is required containing dense, structured mesh at the boundary layer. The mesh generated over the blade in Figure 4-13 represents the boundary layer mesh. A close-up view of the mesh at the trailing edge is shown in Figure 4-14. Table 4-9 presents the boundary conditions for simulating the flow. All simulations are performed using the $k-\omega-SST$ turbulence model. This is a hybrid model which uses the $k-\omega$ model in the near wall region whereas in all other regions it employs the standard $k-\epsilon$ formulation [41].

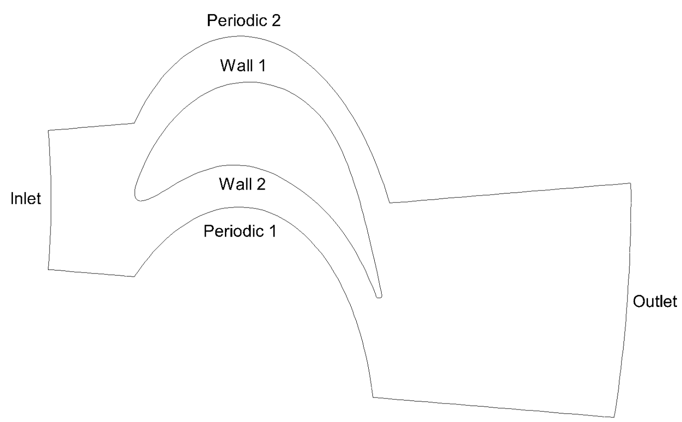

Figure 4-12: CFD domain for a centrifugal blade.

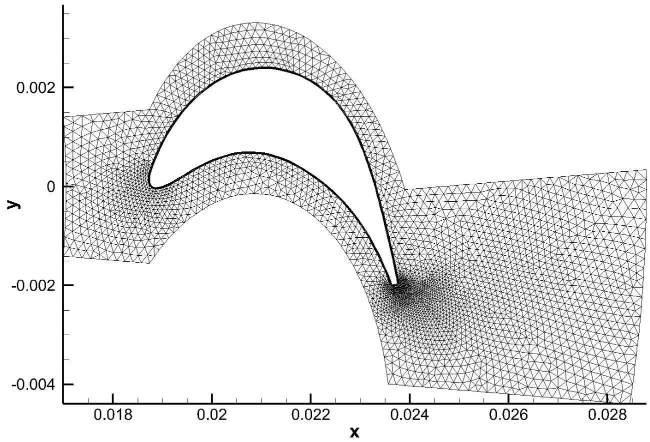

Figure 4-13: Mesh generated for the turbine blade.

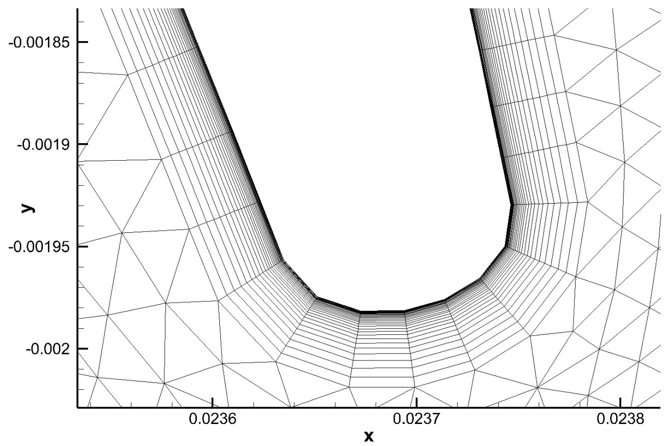

Figure 4-14: Close-up of the boundary layer mesh generated at the trailing edge of the blade.

Table 4-9: Boundary conditions for simulating flow over a centrifugal turbine blade.

Input	
Fluid	MM
Gas model	StanMix
Inlet total pressure [bar]	18.4
Inlet total temperature [K]	525.15
Outlet static pressure [bar]	6.6
$\beta_{flow,in}[^\circ]$	75
Rotational speed [rpm]	43400

4-4-1 Analysis of Dense Gas Flows in the Turbine

Figure 4-15 shows the contours of the compressibility factor. The prescribed inlet conditions are close to the critical point values which leads to significant deviation of the fluid from the ideal gas behaviour as seen from the values of Z. The lowest values of Z are obtained as the fluid expands through the turbine blades. This is similar to the expansion of MM through a de-Laval nozzle as shown in Figure 2-11. Figure 4-16 shows the contours of the relative Mach number of the flow for nominal conditions of critical temperature and pressure. Shock waves are generated at the trailing edge of the blades as seen from the discontinuities in the flow field. Two shock waves are generated on the suction side of different intensities. The first shock occurs due to the interaction of the suction flow with the expansion fan impinging on the suction side. As the flow accelerates along the suction side and reaches supersonic speeds, a second shock wave is generated as seen from the figure. The relative Mach number contours for the other cases are presented in Appendix E.

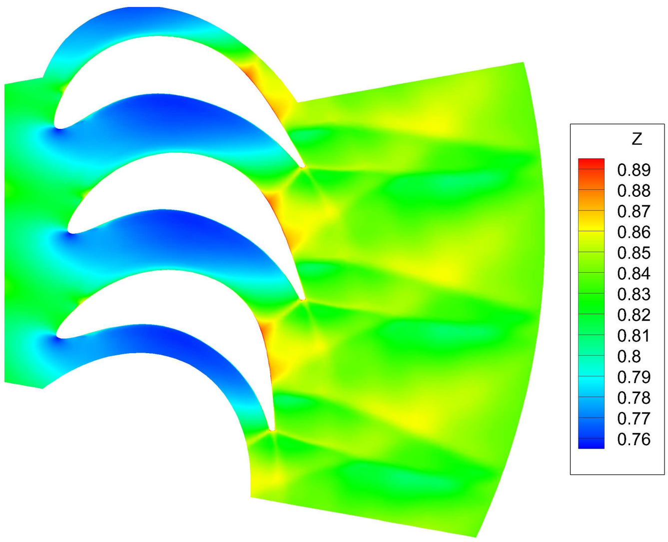

Figure 4-15: Contours of compressibility factor for nominal critical temperature and critical pressure.

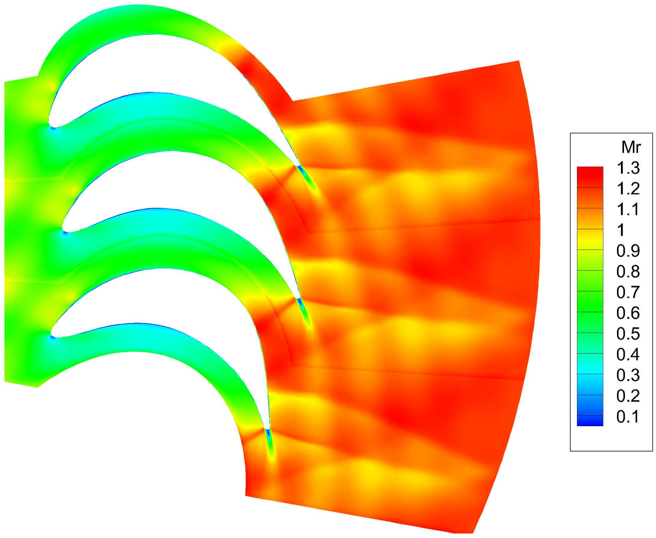

Figure 4-16: Contours of relative Mach number for nominal critical temperature and critical pressure.

Table 4-10: Flow dynamic losses due to variation in the critical point values of MM in a centrifugal turbine.

Case		Values		Loss [%]
$\mathbf{T_{CR}}$	$\mathbf{P_{CR}}$	$\mathbf{T_{CR}}$	$\mathbf{P_{CR}}$	
Nominal	Nominal	245.6	18.424	13.45
Maximum	Maximum	252.968	20.363	17.63
Maximum	Minimum	252.968	18.424	13.21
Maximum	Nominal	252.968	19.394	16.28
Nominal	Maximum	245.6	20.363	17.13
Nominal	Minimum	245.6	18.424	15.61
Minimum	Nominal	238.232	19.394	17.62
Minimum	Maximum	238.232	20.363	22.97
Minimum	Minimum	238.232	18.424	11.53

Table 4-10 reports the static enthalpy loss for each of the nine cases considered. The steps followed to estimate the loss from the CFD results along with the locations at which the properties of the flow are extracted are documented in Appendix F. The values of the properties are extracted from the same location for all the cases. The values of variables at the inlet of the rotor i.e. temperature (T_1), pressure (p_1), enthalpy (h_1), relative velocity (W_1) and radius (r_1) are estimated by averaging the quantities along two lines at the inlet as shown in Figure F-1. The radius is used to compute the local blade speed at the inlet of the turbine as $U_1 = \Omega r_1$ with Ω being the rotational speed in rad/s. The temperature and pressure are used to compute the entropy from the iPRSV EoS as $s_1 = f(p_1, T_1)$. Similarly the properties at the outlet i.e. the enthalpy (h_2), density (ρ_2) and the radius (r_2) are estimated by averaging them along three lines at the exit of the turbine. The isentropic enthalpy (h_{2s}) is then determined from the iPRSV EoS using the relation $h_{2s} = f(\rho_2, s_1)$ while the local blade speed at the outlet of the rotor is computed using the relation $U_2 = \Omega r_2$. Substituting these values in Equations 4-3 and 4-4, the static enthalpy loss is computed. A Matlab function is used which follows the above procedure to compute the losses and is documented in Appendix D.

The values of the losses presented in Table 4-10 show significant variation as the critical properties vary. These results are preliminary and indicate the high variability of the losses against the uncertain variables. Nine samples are too less to obtain a reliable output statistics and hence larger number of samples should be considered.

Figure 4-17(a)-(c) show the contours of the relative Mach number of the flow for the nominal case and the cases that lead to maximum and minimum static enthalpy loss. For the case with minimum deviation in critical temperature and pressure the shock waves are weaker as seen from the change in the relative Mach number. In contrast, for the case represented by Figure 4-17(c), the shock waves generated on the suction side are much stronger and hence the static enthalpy losses are greater. From Table 4-10, it can be deduced that the values of the losses follow the trend of the critical pressure. The losses are the largest when the critical pressure has its maximum value and vice versa. Also the large deviation in losses is expected as the shock wave properties are affected by the changes in critical point values as seen from the analysis of the nozzle performed in Section 3-4-2-2. However, the nozzle analysis was limited to inviscid simulations while the flow considered here is viscous and hence a thorough analysis including the deviation in the boundary layer effects needs to be performed to obtain a better understanding of the variation in these losses.

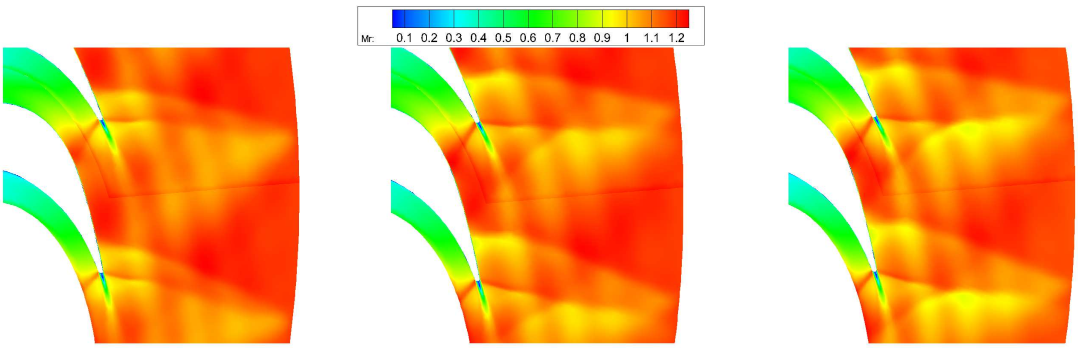

(a) (b) (c)

Figure 4-17: Relative Mach number contours (a) Minimum deviation in critical pressure and temperature (b) Nominal critical temperature and pressure (c) Minimum deviation in critical temperature and maximum deviation in critical pressure.

Chapter 5

Conclusion

The objective of this thesis was to study the influence of thermodynamic property perturbations on NICF phenomena and nozzle design. In order to achieve this objective, the following questions were posed:

- How do the uncertainties in the fluid dependant thermodynamic parameters, geometric parameter and operating conditions affect the compressible flow phenomena in a de-Laval nozzle?
- What are the profile variations in the de-Laval nozzle due to uncertainties in the fluid dependant thermodynamic parameters and operating conditions?
- Does the uncertainty in the critical properties of the fluid affect the flow dynamic losses in a radial outflow turbine?

To find answers to these questions, an uncertainty quantification analysis was performed. The first case simulated was with the wedge placed at the exit of the nozzle so that it lies in a region which shows predominantly ideal gas behaviour. This case was further subdivided into two set of simulations: the first set of simulations were performed by considering the fluid dependant parameters and the geometric parameter to be uncertain while for the second set, in addition to the fluid dependant and geometric parameters, the operational conditions was also considered to be uncertain. The results of the first set of simulations showed that the critical point properties are the most dominant parameters which affect the shock wave characteristics. However the deviation in the angle and intensity of the shock wave was negligible indicating that in the ideal gas region, the uncertainites in the parameters do not affect the compressible flow phenomena. The second set of simulations with the wedge at the same location indicated that with a change in the operating conditions, the energy in the fluid changes thus leading to the ideal gas isobaric heat capacity to be the most dominant parameter. However the deviation in the shock wave properties were again found to be negligible. From the two sets of simulations it was concluded that the real gas region present near the throat has hardly any influence on the downstream shock wave properties.

The second case simulated was with the wedge placed at 7.8 mm from the throat where the thermodynamic properties show significant deviation from the ideal gas behaviour. The same set of simulations as in the first case were performed. The MoC was coupled with the Euler shock wave simulator code to compute the shock wave angle and intensity as well as the deviation in the nozzle profile. Since the MoC is computationally intensive, a sensitivity analysis could not be performed. The results from both the simulation cases show an appreciable deviation in the shock wave characteristics. Considering the fluid dependant parameters and the geometric parameter as the uncertain input variables leads to a deviation of 2.2% and 2.7% in the shock wave angle and the shock wave intensity respectively. On including the operational conditions, the deviation computed was 2.6% and 3.1% in the angle and intensity of the shock waves respectively. These values are much larger in comparison to the first case. Thus it could be concluded that in the real gas region the effect of the uncertainties in the input parameters on the shock wave properties is amplified. The two set of simulations also lead to average deviation of 0.29 mm in the nozzle profile generated. The deviations reported are found by considering five characteristics lines in the MoC. To obtain more reliable values the simulations should be repeated considering greater number of characteristics lines. The deviation in the shock wave angles obtained were verified by performing CFD simulations in SU2. These simulations are limited to only the cases which yield maximum and minimum deviation in the shock wave angle. The results obtained from the UQ analysis compare well with the CFD results thus verifying the low fidelity analysis performed.

The UQ analysis performed for the nozzle is extended to a radial outflow turbine to estimate the deviation in the static enthalpy loss due to variation in the critical point values of MM. Nine cases were considered by varying the critical pressure and temperature. The results from the simulations indicated a large deviation in the computed losses. The large deviations obtained are in accordance with the nozzle simulations with the wedge located at 7.8 mm from the throat in the dense gas region which also showed a large deviation in the shock wave properties. Initial analysis of the results show that the critical pressure could have a greater influence on the losses as compared to the critical temperature. A more rigorous analysis including the uncertainties in the transport properties would offer a better insight into these losses.

Thus, in conclusion, the analysis performed answers all the questions posed. The effect of the thermodynamic uncertainties on the behaviour of shock waves and nozzle profile was quantified. The effect of variation in the critical point values on the losses in a radial outflow turbine were reported by performing CFD simulations. This study thus provides a better understanding of the influence of thermodynamic perturbations on the non-ideal compressible flow phenomena. However, the analysis performed is preliminary and worth to be extended in the future. Suggestions for future work are listed in the next chapter.

Chapter 6

Recommendations for Future Work

The following recommendations are suggested for future work:

- The analysis done in this study is limited to one fluid: MM. Other fluids such as PP90 should be considered. A comparison of the deviation in the shock wave properties obtained from different fluids would help to conclude if a larger real gas region upstream of a shock wave affects the downstream properties.
- The accuracy of the results obtained in this study is limited due to the simplifications made to reduce the computation time. The methods developed could be improved by adopting parallel computing techniques. Multiple fluid files (for example MM1, MM2,..) could be created and a method could be devised which uses these files to perform multiple iterations at the same time.
- The use of different sampling techniques to generate samples of the uncertain input parameters should be investigated. The results obtained from different sampling techniques could be compared with the results presented in this study to select the technique which leads to least computation time to achieve convergence.
- The analysis done with the nozzle was limited to inviscid flows while the analysis for the turbine was done with viscous flows. Thus including the boundary layer in the nozzle simulations would have helped to better understand the effect of changing the input parameters on the transport properties such as viscosity which could have significant effect on the compressible flow phenomena.
- The turbine simulations should be performed with different UQ methods and turbulence models. Also the uncertainty in the parameters of the turbulence models should be taken into account.

Appendix A

Iterative Procedure for Shock Phenomena Calculations

In this chapter the iterative procedure used to calculate the shock wave angle from the mach number and wedge angle(θ) for real gases is detailed [42].

Step 1: Starting with V_1, p_1, ρ_1 and θ calculate $h_1 = h(p_1, \rho_1)$ from a curve fit or equilibrium composition.
Step 2: Guess a value of ν, where $\nu = \rho_1/\rho_2$.
Step 3: Solve for β corresponding to the guessed value of ν using Equation 2-22. Then $V_{N1} = V_1 sin\beta$.
Step 4: From equation 2-10 - 2-12, $V_{N2} = V_{N1}\nu$, $p_2 = p_1 + \rho_1 V_{N1}^2(1-\nu)$ and $h_2 = h_1 + (V_{N1}^2/2)(1-\nu^2)$.
Step 5: Determine the enthalpy $\tilde{h}$ from the equation of state such that $\tilde{h}_2 = h(p_2, \rho_2)$.
Step 6: Is $h_2 = \tilde{h}_2$. If not, modify the value of ν using a root finding procedure and continue from step 3.

Appendix B

Steps to Run Uncertainty Quantification Analysis using DAKOTA

Step 1: Create a wrapper function which links DAKOTA and MATLAB. The wrapper function is a MATLAB function which includes the code to edit the FluidProp file and the main analysis function. The parameters file and the results file are passed on as arguments to the wrapper function.
Step 2: Modify the analysis function *Analysis_ShockWaveIntensity.m* such that it returns the value of the quantities of interest in the form of an array. These values will be written in the results text file.
Step 3: Create a visual basic script file (*.vbs* file) to call the MATLAB command window and the wrapper function.
Step 4: Create the DAKOTA input file by defining the sampling procedure, number of samples, distribution of samples, the number of variables, the range of each variable and the number of response functions. Include the name of the visual basic script file under the interface section in the input file. Save all the files, i.e., the MATLAB wrapper function, visual basic script file, DAKOTA input file and any other files required for performing the UQ analysis in the same folder.
Step 5: Open a command prompt window and run the command: *set path="Path of DAKOTA bin folder";"Path of the folder where all the files are saved";%path%*. Do not include the " " while specifying the path.
Step 6: Change the working directory to the folder in which all the required files are stored.
Step 7: Run the command: *dakota -i Input_file.in -o Output_file.out* to start the analysis.
Step 8: In case the analysis stops use the restart file to continue the simulations from the last saved result. To restart the analysis, run the command: *dakota -i Input_file.in -o Output_file.out -r dakota.rst*. By default the DAKOTA restart file is named as *dakota.rst*.
Step 9: Run the command: *dakota_restart_util to_tabular dakota.rst Output_file.txt* to obtain the results in a tabular form. The results are written in a text file saved under the

name *Output_file.txt*.
Step 10: Run a matlab function which uses the *Output_file.txt* as an argument to post process the results.

Example input file used for performing convergence study. Results obtained from the analysis are documented in Section 3-4-2-1.

```
# Monte-Carlo UQ analysis for 1-D compressible flow

environment
        tabular_graphics_data
                tabular_graphics_file = 'ShockWaveUQ_final.dat'

method
      sampling
                sample_type random
                distribution cumulative
                samples 20000
                seed 125000

variables
uniform_uncertain = 11
lower_bounds = 238.232 18.42392 0.39805 -0.0554945 44.1099
630.139 -478.515 59.5 19.998 1838160 519.8985
upper_bounds = 252.968 20.36328 0.43995 -0.0502093 59.6781
852.541 -353.685 80.5 20.002 1841840 530.4015
descriptors = 'tcr' 'pcr' 'af' 'k1' 'cp01' 'cp02' 'cp03' 'cp04'
'thetalist' 'P_1' 'T_1'

interface
  fork
    analysis_driver = 'cscript matlab_ShockWave_simulator.vbs'
    parameters_file = 'params.in'
    results_file    = 'results.out'
    #file_tag
    #file_save
    #work_directory directory_tag
    #copy_files = 'templatedir/*'
    #named 'workdir' file_save directory_save
    #aprepro

responses
    response_functions = 5
    no_gradients
    no_hessians
```

Appendix C

Steps to Generate Mesh using UMG2 and Run SU2

Step 1: Enter the number of surfaces and coordinates of the model in the *geomerty.dia* file.
Step 2: Enter the number of boundary layers in the *options* file.
Step 3: Specify the thickness of the boundary layer and the size of each boundary condition in the *spacingcontrol.dia* file. To generate a dense mesh, decrease the value of grid spacing.
Step 4: Specify the boundary condition type and the number of zones in the *topology.dia* file.
Step 5: Open a command prompt window and change the working directory to the folder in which the above files are stored.
Step 6: Run ..\MCURVE.exe
Step 7: Run ..\BGRID.exe
Step 8: Run ..\UMG2D.exe
Step 9: If boundary layer mesh is to be generated then run ..\HYB2D.exe
Step 10: To run simulations using SU2, copy the *su2mesh.su2* file and the configuration file to a folder.
Step 11: Open a new terminal on cygwin and change the working directory to the folder in which the configuration and the mesh file are stored.
Step 12: To perform the simulations in parallel, run *parrallel_configuration -f 'config_file'.cfg - n* where 'config_file.cfg' represents the configuration file and n stands for the number of processors. For serial simulations, run the command *SU2_CFD.exe 'config_file'.cfg*
Step 13: Run the command *SU2_SOL.exe 'config_file'.cfg* to obtain the solutions files.
Step 14: To view and post process the solution, open the *flow.dat* file in Tecplot. To view the solutions along a particular surface specified in the configuration file, open the *surface_flow.dat* file in Tecplot.

UMG2 Input files

The following files were used to create the unstructured mesh for the nozzle with the wedge at 7.8 mm from the throat. The mesh generated is shown in Section 4-2-3.

Geometry file
The geometry file is used to define the coordinates, set the number of boundaries and label them.

```
  Number of surfaces
                8
 INLET
              ' S '
               dim                   np
                 2                   2
                 x                   y
-63.4583349      14.823611780
-63.4583349      -8.062401282
 SYMM
              ' S '
               dim                   np
                 2                   2
                 x                   y
-63.4583349      -8.062401282
-16.6683349      -8.062401282
DIAMOND FRONT
              ' S '
               dim                   np
                 2                   2
                 x                   y
-16.6683349      -8.062401282
-4.30468652      -3.562401282
DIAMOND BACK
              ' S '
               dim                   np
                 2                   2
                 x                   y
-4.30468652      -3.562401282
8.536006692      -8.062401282
SYM2
              ' S '
               dim                   np
                 2                   2
                 x                   y
8.536006692      -8.062401282
98.58745510      -8.062401282
 OUT
              ' S '
```

```
                 dim                  np
                   2                  2
                   x                  y
98.58745510        -8.062401282
98.58745510        17.362536780
 TESTCASE TOP
                ' S '
                 dim                  np
                   2                  2
                   x                  y
98.58745510        17.362536780
58.58745510        17.362536780
 TOP
                ' S '
                 dim                  np
                   2                 102
                   x                   y
-63.4583349         14.823611780       0
-62.16395946        14.77055005        0
-60.88182728        14.61788525        0
-59.6142715         14.375602          0
-58.36330041        14.05378365        0
-57.1306871         13.66241594        0
-55.91809244        13.21127729        0
-54.72673998        12.70969779        0
-53.55504856        12.16525168        0
-52.40312676        11.57939592        0
-51.27195059        10.9531607         0
-50.1594678         10.29332731        0
-49.06358693        9.606083466        0
-47.98225024        8.897106895        0
-46.91266015        8.171097906        0
-45.85188063        7.432209937        0
-44.79719924        6.684405659        0
-43.7460136         5.931493465        0
-42.69578736        5.177197294        0
-41.64400133        4.425216298        0
-40.58775202        3.679035655        0
-39.5244763         2.942545632        0
-38.45190906        2.220088242        0
-37.36761316        1.516211017        0
-36.26894059        0.835746732        0
-35.15301105        0.183923495        0
-34.01629344        -0.433712172       0
-32.85640708        -1.010185307       0
-31.67367237        -1.536628398       0
-30.46842012        -2.003994545       0
```

```
-29.24095612    -2.403163745    0
-27.99160344    -2.725018627    0
-26.72118014    -2.960471429    0
-25.43599974    -3.100400025    0
-24.14412763    -3.137949723    0
-22.85304527    -3.069280049    0
-21.57487656    -2.880580487    0
-20.37452427    -2.411819514    0
-19.25367541    -1.767698203    0
-18.15660788    -1.084754531    0
-17.08568983    -0.360287569    0
-16.02794331    0.383881839     0
-14.96953418    1.126654328     0
-13.89609298    1.847345395     0
-12.79876509    2.530495664     0
-11.6799039     3.177792656     0
-10.54382812    3.793862064     0
-9.393807162    4.383923125     0
-8.232925774    4.953225027     0
-7.064146752    5.506912396     0
-5.889164055    6.047364776     0
-4.708243854    6.573859474     0
-3.521002985    7.085771531     0
-2.327278763    7.582375996     0
-1.127009631    8.062911589     0
0.079838398     8.526625517     0
1.293091634     8.973272103     0
2.512299988     9.403433378     0
3.736962331     9.817756286     0
4.966645374     10.21690911     0
6.200964274     10.60157125     0
7.439540496     10.97241837     0
8.682010221     11.33008922     0
9.928090114     11.6749345      0
11.17753165     12.0071611      0
12.43014653     12.32699366     0
13.68578167     12.6346665      0
14.94428463     12.93041383     0
16.20550346     13.21446969     0
17.46928684     13.48706685     0
18.73548583     13.74842784     0
20.00395243     13.99877011     0
21.27453834     14.23831124     0
22.54709502     14.46726908     0
23.82147369     14.68586166     0
25.09752533     14.89430725     0
26.37510256     15.09282476     0
```

27.65410786	15.28165741	0
28.93445144	15.461081	0
30.21603595	15.63137406	0
31.49876849	15.79281608	0
32.78256027	15.94568728	0
34.06732636	16.09026844	0
35.35298532	16.22684072	0
36.63945905	16.35568368	0
37.92668649	16.47691359	0
39.21463215	16.59035583	0
40.5032561	16.69580483	0
41.79251002	16.7930541	0
43.08232243	16.88189551	0
44.37262132	16.96212143	0
45.66342293	17.03352934	0
46.95472527	17.09591399	0
48.24649028	17.14920556	0
49.53862794	17.19414673	0
50.83104781	17.23177883	0
52.12366976	17.26314508	0
53.41642176	17.28928957	0
54.70923783	17.31125674	0
56.00205579	17.330091	0
57.29481518	17.34683647	0
58.5874551	17.36253678	0

Options file

The options file contains a summary of the settings of the mesh generator.

```
fmt      name
'grd'    'dia'
optimization
1
max element deformation
1.
layer of the background grid
0
Periodic geometry
.false.
number of boundary layers
0
Graph for hybrid mesh construction
.false.
Kind of radial basis function (1-10)
11
Support radius for compact basis functins
10.0
```

Topology

The topology file defines the zones within the domain and type of each curve.

```
           curve type     periodic curve    Modifiable curve
                   1                  0                   0
                   2                  0                   0
                   8                  0                   0
                   8                  0                   0
                   2                  0                   0
                   3                  0                   0
                   9                  0                   0
                   9                  0                   0
Number of ZONE
1
ZONE 1
 1
 2
 3
 4
 5
 6
 7
-8
1  far-field/inflow
2  symmetry
3  outflow
4  periodic1
5  periodic2
8  wall1
9  wall2
10 wall3
11 wall4
12 wall5
13 wall6
```

Spacing control

The spacing control file sets the maximum and minimum mesh spacing at each edge and has options to include the boundary layer mesh.

```
    thk_bl      n BC      GEOM        CV
    0.025        5        axl         0

         PITCH              xc              yc
       1.5000000            1.0             1.0

 1  INFLOW        h_min     h_max  Nd RdCRv
```

```
                 1.5       1.5       5.
 2  SYM          h_min     h_max  Nd RdCRv
                 1.5       1.5       5.
 3  OUT          h_min     h_max  Nd RdCRv
                 1.5       1.5       5.
 8   DIA WALL    h min     h max  Nd RdCRv
                 1.5       1.5       15.
 9   TOP WALL    h min     h max  Nd RdCRv
                 1.5       1.5       15.

  NZONES
       1
    RADIUS        XC        YC         h
      150.   -45.000       0.0       2.5
    RADIUS        XC        YC         h
       60.   150.000       0.0       1.5
```

SU2 Input file

The following file is a SU2 input file to simulate the flow through a nozzle with the model located at 7.8 mm from the throat. The results of the simulation are documented in Section 4-2-3.

```
%%%%%%%%%%%%%%%%%%%%%%%%%%%%%%%%%%%%%%%%%%%%%%%%%%%%%%%%%%%%%%%%%%%%%%%%%%%%%%%%
%                                                                              %
% Stanford University Unstructured (SU2) configuration file                    %
% Case description: 3D nozzle without needle                                   %
% Author: Matteo Pini, S. Vitale                                               %
% Institution: Delft University of Technology                                  %
% Date: 2014.04.02                                                             %
%                                                                              %
%%%%%%%%%%%%%%%%%%%%%%%%%%%%%%%%%%%%%%%%%%%%%%%%%%%%%%%%%%%%%%%%%%%%%%%%%%%%%%%%

% ------------- DIRECT, ADJOINT, AND LINEARIZED PROBLEM DEFINITION ------------%
%
% Physical governing equations (EULER, NAVIER_STOKES, NS_PLASMA)
%
PHYSICAL_PROBLEM= EULER
%
% Specify turbulent model (NONE, SA, SST)
KIND_TURB_MODEL= SST
%
% Mathematical problem (DIRECT, ADJOINT, LINEARIZED)
MATH_PROBLEM= DIRECT
```

```
%
% Restart solution (NO, YES)
RESTART_SOL= NO
%
% Reference pressure (101325.0 N/m^2 by default)
%REF_PRESSURE= 1500000.0
%
% Reference temperatre (273.15 K by default)
%REF_TEMPERATURE= 518.75
%
% Reference density (1.2886 Kg/m^3 (air), 998.2 Kg/m^3 (water))
%REF_DENSITY= 633.77
%
% Reference element length for computing the slope limiter epsilon
REF_ELEM_LENGTH= 0.1

% --------- COMPRESSIBLE AND INCOMPRESSIBLE FREE-STREAM DEFINITION --------%
%
% Mach number (non-dimensional, based on the free-stream values)
MACH_NUMBER= 0.1
%
% Angle of attack (degrees)
AoA= 0.0
%
% Side-slip angle (degrees, only for compressible flows)
%SIDESLIP_ANGLE= -70.0
%
% Free-stream pressure (101325.0 N/m^2 by default, only Euler flows)
FREESTREAM_PRESSURE= 1500000.0
%
% Free-stream temperature (273.15 K by default)
FREESTREAM_TEMPERATURE= 525.15
%

% Free-stream temperature (1.2886 Kg/m3 by default)
FREESTREAM_DENSITY= 1.2886
%
% Free-stream option
FREESTREAM_OPTION= TEMPERATURE_FS
%
% Free-stream Turbulence Intensity
FREESTREAM_TURBULENCEINTENSITY = 0.001
%
% Free-stream Turbulent to Laminar viscosity ratio
FREESTREAM_TURB2LAMVISCRATIO = 100.0
%
% Reynolds number (non-dimensional, based on the free-stream values)
```

```
REYNOLDS_NUMBER= 6.0E6
%

% -------------- GAS MODEL --------------%
%
% Different gas model (IDEAL_GAS, VW_GAS,...)
%FLUID_MODEL = PR_GAS
FLUID_MODEL= FLUIDPROP
FLUID_SUBLIBRARY= Stanmix
FLUID_N_COMPONENTS= 1
FLUID_COMPONENTS= (MM)
FLUID_MOLE_FRACS= (1.00)
FLUID_SINGLE_PHASE_ONLY= YES
%

%----------------- VW and PR  GAS CONSTANTs-----------------%
%
% Critical Temperature (273.15 K by default)
CRITICAL_TEMPERATURE= 518.75
% Critical Pressure (101325.0 N/m^2 by default)
CRITICAL_PRESSURE= 1939360.0
% Critical Density (1.2886 Kg/m3 by default)
CRITICAL_DENSITY= 633.77

%-----------------POLYTROPIC IDEAL GAS, VW and PR CONSTANTs-----------------%

% Ratio of specific heats (1.4 (air), only for compressible flows)
GAMMA_VALUE= 1.1158
%
% Specific gas constant (287.87 J/kg*K (air), only for compressible flows)
GAS_CONSTANT= 51.2040

%----------------- PR GAS CONSTANT-----------------%
% Acentri factor ( 0.035 (air) )
ACENTRIC_FACTOR= 0.419

% --------------------------- VISCOSITY MODEL -------------------------------%

% Viscosity model (SUTHERLAND, CONSTANT_VISCOSITY).
%VISCOSITY_MODEL= CONSTANT_VISCOSITY
%
% Molecular Viscosity that would be constant (1.716E-5 by default)
%MU_CONSTANT= 2.4087E-5
%
% Sutherland Viscosity Ref (1.716E-5 default value for AIR SI)
%MU_REF= 1.716E-5
%
```

```
% Sutherland Temperature Ref (273.15 K default value for AIR SI)
%MU_T_REF= 273.15
%
% Sutherland constant (110.4 default value for AIR SI)
%SUTHERLAND_CONSTANT= 110.4

% --------------------------- THERMAL CONDUCTIVITY MODEL --------------------%
%
% Conductivity model (CONSTANT_CONDUCTIVITY, CONSTANT_PRANDTL).
%CONDUCTIVITY_MODEL= CONSTANT_CONDUCTIVITY
%
% Molecular Thermal Conductivity that would be constant (0.0257 by default)
%KT_CONSTANT= 0.0260

% -------------------- BOUNDARY CONDITION DEFINITION ------------------------%
%
% Euler wall boundary marker(s) (NONE = no marker)
MARKER_EULER= (wall1, wall2)
%
% Inlet boundary marker(s) (NONE = no marker)
% Format: ( inlet marker, total temperature, total pressure, flow_direction_x,
%           flow_direction_y, flow_direction_z, ... ) where flow_direction is
%           a unit vector.
%MARKER_INLET= ( inflow, 545.17, 800000.0, 1.0, 0.0, 0.0 )
MARKER_RIEMANN= (inflow, TOTAL_CONDITIONS_PT, 1840000.0, 525.15, 0.0, 0., 0.0,
                outflow, STATIC_PRESSURE, 100000, 0.0, 0.0, 0.0, 0.0)
%
% Outlet boundary marker(s) (NONE = no marker)
% Format: ( outlet marker, back pressure (static), ... )
%MARKER_OUTLET= ( outflow, 100000.0 )
%
% Symmetry boundary marker(s) (NONE = no marker)
% Format: ( symmetry marker )
MARKER_SYM= ( symmetry )

% --------------------- SURFACES IDENTIFICATION -----------------------------%
%
% Marker(s) of the surface to be plotted or designed
MARKER_PLOTTING= ( wall2 )
%
% Marker(s) of the surface where the functional (Cd,Cl,etc.) will be evaluated
MARKER_MONITORING= ( wall2 )

% ------------- COMMON PARAMETERS DEFINING THE NUMERICAL METHOD -------------%
%
% Numerical method for spatial gradients (GREEN_GAUSS, WEIGHTED_LEAST_SQUARES)
NUM_METHOD_GRAD= GREEN_GAUSS
```

```
%
% Courant-Friedrichs-Lewy condition of the finest grid
CFL_NUMBER= 1
%
% CFL ramp (factor, number of iterations, CFL limit)
%CFL_RAMP= ( 1.1, 100, 10 )
%
% Runge-Kutta alpha coefficients
RK_ALPHA_COEFF= ( 0.66667, 0.66667, 1.000000 )
%
% Number of total iterations
EXT_ITER= 200000

% ------------------------ LINEAR SOLVER DEFINITION -------------------------%
%
% Linear solver for implicit formulations (BCGSTAB, FGMRES)
LINEAR_SOLVER= FGMRES
%
% Preconditioner of the Krylov linear solver (JACOBI, LINELET, LU_SGS)
LINEAR_SOLVER_PREC= LU_SGS
%
% Minimum error of the linear solver for implicit formulations
LINEAR_SOLVER_ERROR= 1E-4
%
% Max number of iterations of the linear solver for the implicit formulation
LINEAR_SOLVER_ITER= 100
%
% Relaxation coefficient
%LINEAR_SOLVER_RELAX= 1.0

% -------------------------- MULTIGRID PARAMETERS ---------------------------%
%
% Multi-Grid Levels (0 = no multi-grid)
MGLEVEL= 0
%
% Multi-Grid Cycle (0 = V cycle, 1 = W Cycle)
%MGCYCLE= 0
%
% Maximum number of children in the agglomeration stage
%MAX_CHILDREN= 250
%
% Maximum length of an agglomerated element (relative to the domain)
%MAX_DIMENSION= 0.1
%
% Multigrid pre-smoothing level
MG_PRE_SMOOTH= ( 1, 2, 3, 3 )
%
```

```
% Multigrid post-smoothing level
MG_POST_SMOOTH= ( 0, 0, 0, 0 )
%
% Jacobi implicit smoothing of the correction
MG_CORRECTION_SMOOTH= ( 0, 0, 0, 0 )
%
% Damping factor for the residual restriction
MG_DAMP_RESTRICTION= 0.9
%
% Damping factor for the correction prolongation
MG_DAMP_PROLONGATION= 0.9
%
% Full Multigrid (NO, YES)
%FULLMG= NO
%
% Start up iterations using the fine grid
START_UP_ITER= 0

% -------------------- FLOW NUMERICAL METHOD DEFINITION ---------------------%
%
% Convective numerical method (JST, LAX-FRIEDRICH, CUSP, ROE, AUSM, HLLC,
%                               TURKEL_PREC, MSW)
CONV_NUM_METHOD_FLOW= ROE
%
% Spatial numerical order integration (1ST_ORDER,2ND_ORDER,2ND_ORDER_LIMITER)
%
SPATIAL_ORDER_FLOW= 1ST_ORDER
%SPATIAL_ORDER_FLOW= 2ND_ORDER
%SPATIAL_ORDER_FLOW= 2ND_ORDER_LIMITER
%
% Slope limiter (VENKATAKRISHNAN, MINMOD)
SLOPE_LIMITER_FLOW= VENKATAKRISHNAN
%
% Coefficient for the limiter
LIMITER_COEFF= 0.5
%
% 1st, 2nd and 4th order artificial dissipation coefficients
AD_COEFF_FLOW= ( 0.15, 0.5, 0.02 )
%
% Time discretization (RUNGE-KUTTA_EXPLICIT, EULER_IMPLICIT, EULER_EXPLICIT)
TIME_DISCRE_FLOW= EULER_IMPLICIT

% -------------------- TURBULENT NUMERICAL METHOD DEFINITION ----------------%
%
% Convective numerical method (SCALAR_UPWIND)
CONV_NUM_METHOD_TURB= SCALAR_UPWIND
%
```

```
% Spatial numerical order integration (1ST_ORDER,2ND_ORDER,2ND_ORDER_LIMITER)
%
SPATIAL_ORDER_TURB= 1ST_ORDER
%
% Slope limiter (VENKATAKRISHNAN, MINMOD)
SLOPE_LIMITER_TURB= VENKATAKRISHNAN
%
% Time discretization (EULER_IMPLICIT)
TIME_DISCRE_TURB= EULER_IMPLICIT
%
% Reduction factor of the CFL coefficient in the turbulence problem
CFL_REDUCTION_TURB= 1.0

% --------------------------- PARTITIONING STRATEGY -------------------------%
% Write a tecplot/paraview file for each partition (NO, YES)
%VISUALIZE_PART= NO

% --------------------------- CONVERGENCE PARAMETERS ------------------------%
%
% Convergence criteria (CAUCHY, RESIDUAL)
%
CONV_CRITERIA= RESIDUAL
%
% Residual reduction (order of magnitude with respect to the initial value)
RESIDUAL_REDUCTION= 12
%
% Min value of the residual (log10 of the residual)
RESIDUAL_MINVAL= -8
%
% Start convergence criteria at iteration number
STARTCONV_ITER= 10
%
% Number of elements to apply the criteria
CAUCHY_ELEMS= 100
%
% Epsilon to control the series convergence
CAUCHY_EPS= 1E-10
%
% Function to apply the criteria (LIFT, DRAG, NEARFIELD_PRESS, SENS_GEOMETRY,
%                                           SENS_MACH, DELTA_LIFT, DELTA_DRAG)
CAUCHY_FUNC_FLOW= DRAG
CAUCHY_FUNC_LIN= DELTA_DRAG
%
% Epsilon for full multigrid method evaluation
%FULLMG_CAUCHY_EPS= 1E-4

% ------------------------- INPUT/OUTPUT INFORMATION ------------------------%
```

```
%
% Mesh input file
%MESH_FILENAME= PP90half.cgns
MESH_FILENAME= su2mesh.su2
%
% Mesh input file format (SU2, CGNS, NETCDF_ASCII)
MESH_FORMAT= SU2
%
% Divide rectangles into triangles (NO, YES)
%DIVIDE_ELEMENTS= NO
%
% Convert a CGNS mesh to SU2 format (YES, NO)
%CGNS_TO_SU2= YES
%
% Mesh output file
MESH_OUT_FILENAME= mesh_out.su2
%
% Restart flow input file
SOLUTION_FLOW_FILENAME= restart_flow.dat
%
% Restart linear flow input file
SOLUTION_LIN_FILENAME= solution_lin.dat
%
% Restart adjoint input file
SOLUTION_ADJ_FILENAME= solution_adj.dat
%
% Output file format (PARAVIEW, TECPLOT, STL)
OUTPUT_FORMAT= TECPLOT
%
% Output file convergence history (w/o extension)
CONV_FILENAME= history
%
% Output file restart flow
RESTART_FLOW_FILENAME= restart_flow.dat
%
% Output file restart adjoint
RESTART_ADJ_FILENAME= restart_adj.dat
%
% Output file linear flow
RESTART_LIN_FILENAME= restart_lin.dat
%
% Output file flow (w/o extension) variables
VOLUME_FLOW_FILENAME= flow
%
% Output file adjoint (w/o extension) variables
VOLUME_ADJ_FILENAME= adjoint
%
```

```
% Output file linearized (w/o extension) variables
VOLUME_LIN_FILENAME= linearized
%
% Output objective function gradient (using continuous adjoint)
GRAD_OBJFUNC_FILENAME= of_grad.dat
%
% Output file surface flow coefficient (w/o extension)
SURFACE_FLOW_FILENAME= surface_flow
%
% Output file surface adjoint coefficient (w/o extension)
SURFACE_ADJ_FILENAME= surface_adjoint
%
% Output file surface linear coefficient (w/o extension)
SURFACE_LIN_FILENAME= surface_linear
%
% Writing solution file frequency
WRT_SOL_FREQ= 250
%
% Writing convergence history frequency
WRT_CON_FREQ= 1
```

Appendix D

MATLAB Function Documentation

This appendix provides a brief description of the main Matlab functions used in this study.

Section 2-2-1

Analysis_ShockWaveIntensityAIR.m

- Code to plot the $\theta - \beta - M$ diagram for air.
- Calls the *AIRShockWaveIntensity.m* function.

AIRShockWaveIntensity.m

- Implements the iterative procedure of the Euler shock wave simulator documented in Appendix A.
- Main inputs to the function are the fluid, temperature at the inlet of the nozzle (*T_1*), inlet pressure (*P_1*), throat area (*A_throat*) and the back pressure (*P_bvalve*)

CalcAnalyticalThetaAir.m

- Code to plot the $\theta - \beta - M$ diagram for air.
- Uses the $\theta - \beta - M$ relation shown in Equation 2-21.
- Specify the value of the upstream Mach number, $M1$ in the code to plot the corresponding $\theta - \beta - M$ diagram.

Section 2-3-3

Analysis_ShockWaveIntensity.m

- Code used to plot the $\theta - \beta - M$ diagram for MM.
- Calls the *RealShockWaveIntensityv1.m* function.

- Implements the iterative procedure of the Euler shock wave simulator documented in Appendix A.
- Specify the temperature, pressure and the upstream Mach number to plot the diagram.

Section 3-4-2-1 Case I
Wrapper_ShockwaveIntensity.m

- This function is executed for each sample created by DAKOTA.
- Edits the FluidProp file, *MM.smx* with the values obtained from DAKOTA for each iteration.
- Calls the *Analysis_ShockWaveIntensitySC.m* function which computes the shock wave angle and the shock wave intensity.
- Writes the solutions to a results file.

Analysis_ShockWaveIntensitySC.m

- Main analysis function which computes the shock wave angle and intensity.
- Calls the *RealShockWaveIntensitySC.m* function.
- Runs the iterative procedure to maintain a constant Mach number in front of the shock wave.

Section 4-2-2
findbetafromCFD.m

- Code to compute the shock wave angle from SU2 results.
- Reads the *surface_flow.dat* file to estimate the coordinate of the point at which the shock wave hits the nozzle wall.
- From the coordinates of the above mentioned point and the fixed coordinates of the apex of the wedge, the shock wave angle is computed.

Section 4-4-1
readtecplotfile.m

- Code to compute the static enthalpy loss.
- Reads the five *dat* files (two from the inlet and three form the outlet of the rotor) which contains the values of the flow properties extracted along the lines shown in Figure F-1.
- Values of the average temperature (T_1), pressure (p_1), enthalpy (h_1), relative velocity (W_1) and radius (r_1) are computed from the values extracted from the lines in the inlet region of the turbine.

- From T_1 and p_1, the entropy is computed from the iPRSV EoS as $s_1 = f(p_1, T_1)$.
- Local blade speed at the inlet of the rotor, U_1 is computed as $U_1 = r_1\Omega$ where Ω is the rotational speed of the turbine in rad/s.
- Values of the average density (ρ_2), enthalpy (h_2), and radius (r_2) are computed from the values extracted from the lines at outlet of the rotor. Local blade speed at the outlet is computed using the relation $U_2 = r_2\Omega$.
- Isentropic enthalpy at the exit is computed from the iPRSV EoS as $h_{2s} = f(\rho_2, s_1)$.
- From the values of h_1, W_1, U_1, h_{2s} and U_2 and using Equation 4-4, the value of W_{2s} is computed.
- Value of static enthalpy loss is estimated from the values of h_2, h_{2s} and W_{2s} using Equation 4-3.

Appendix E

Additional Results

DAKOTA results

The results of the sensitivity analysis for 15% variation in the acentric factor and κ_1 parameter are presented here.

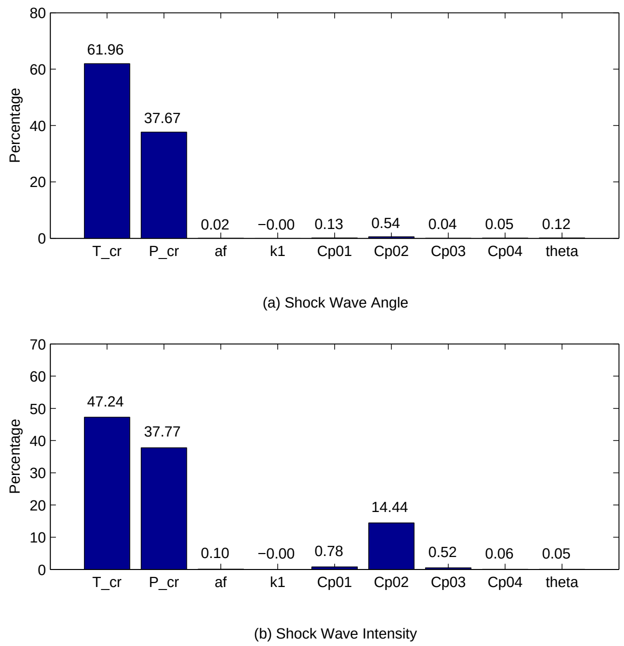

Figure E-1: Sensitivity analysis of the shock wave angle and shock wave intensity due to deviations in the fluid dependant parameters and geometric parameter.

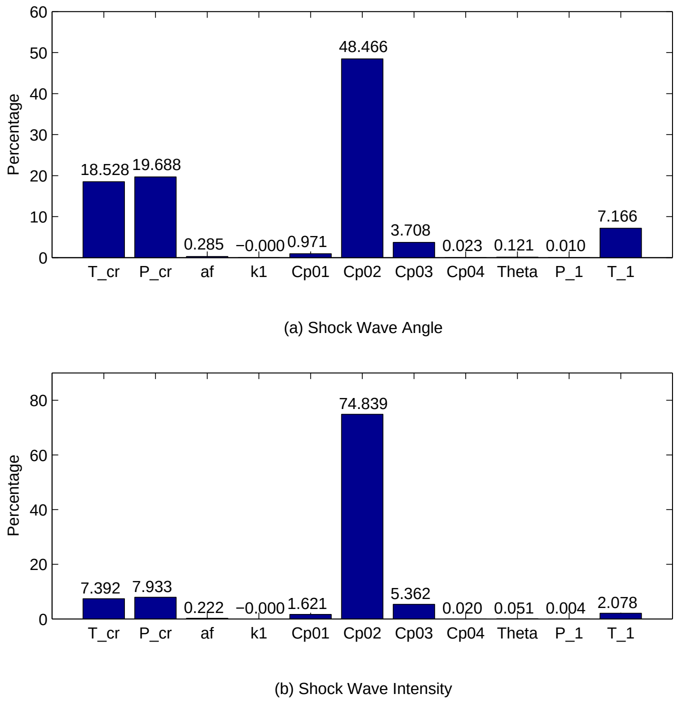

Figure E-2: Sensitivity analysis of the shock wave angle and shock wave intensity due to deviations in the fluid dependant parameters, geometric parameter and operating conditions.

CFD simulation results

This section presents the contours of the relative Mach number for the cases presented in Section 4-4-1.

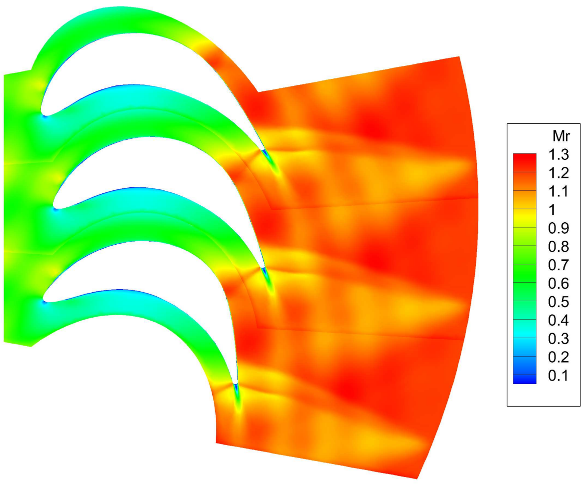

Figure E-3: Contours of relative Mach number for nominal critical temperature and 5% increase in critical pressure.

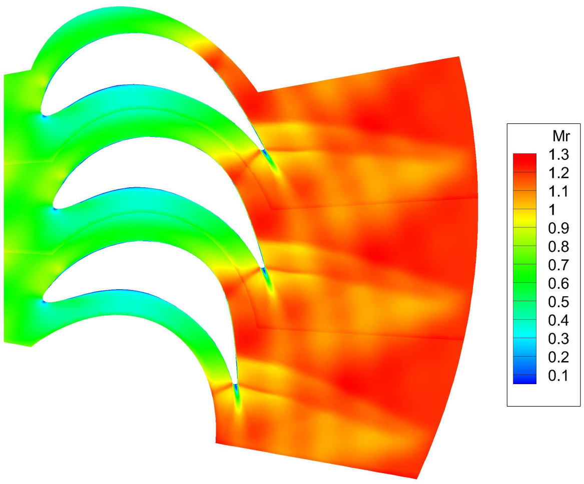

Figure E-4: Contours of relative Mach number for 3% increase in critical temperature and nominal critical pressure.

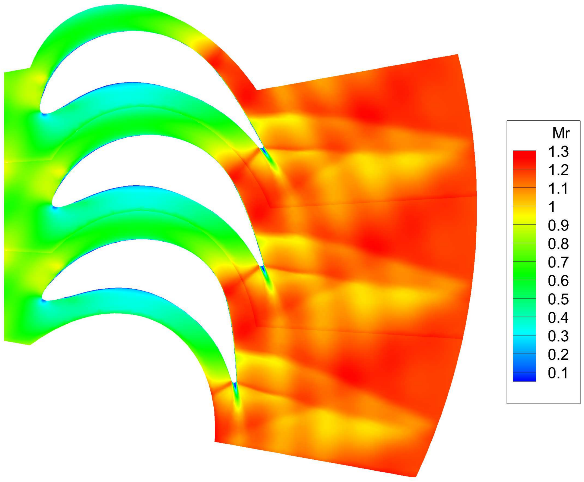

Figure E-5: Contours of relative Mach number for 3% decrease in critical temperature and nominal critical pressure.

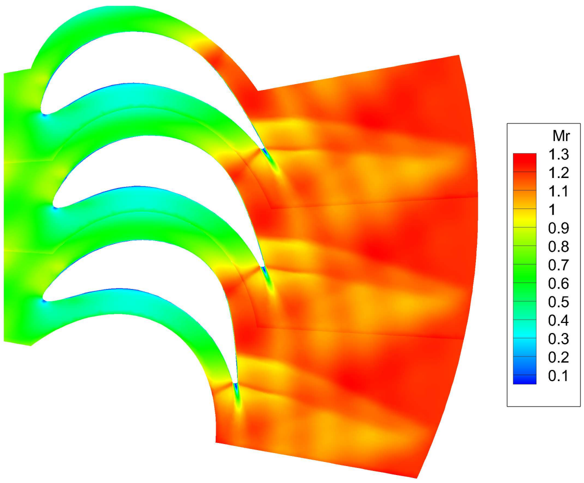

Figure E-6: Contours of relative Mach number for nominal critical temperature and 5% decrease in critical pressure.

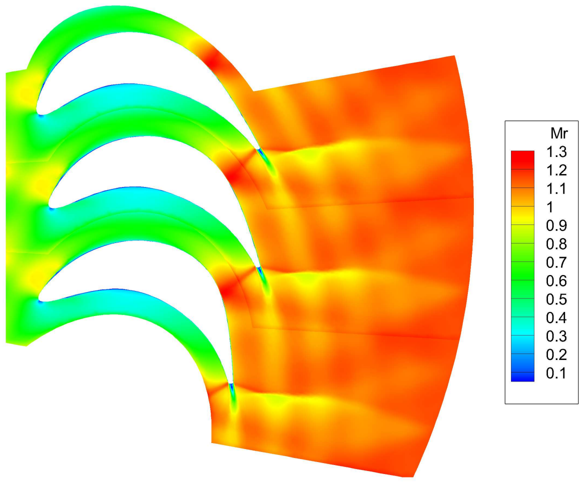

Figure E-7: Contours of relative Mach number for 3% increase in critical temperature and 5% increase in critical pressure.

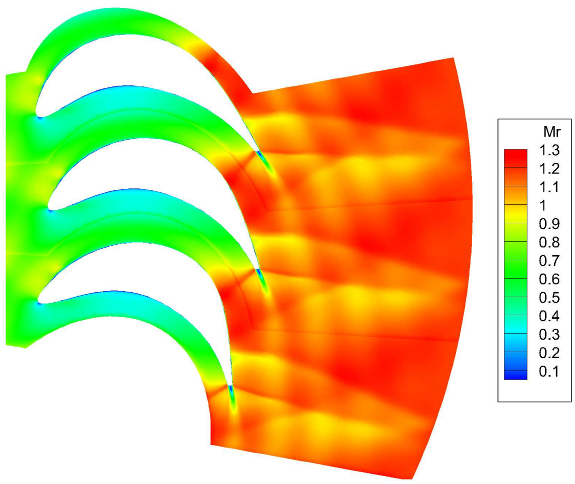

Figure E-8: Contours of relative Mach number 3% increase in critical temperature and 5% decrease in critical pressure.

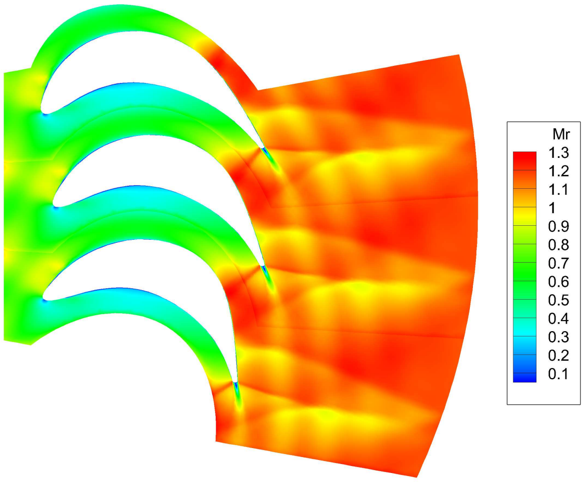

Figure E-9: Contours of relative Mach number for 3% decrease in critical temperature and 5% increase in critical pressure.

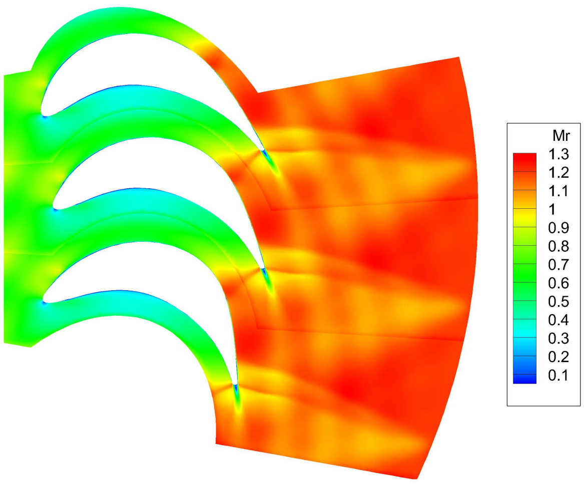

Figure E-10: Contours of relative Mach number for 3% decrease in critical temperature and 5% decrease in critical pressure.

Appendix F

Steps to Estimate the Static Enthalpy Loss in the Radial Outflow Turbine

The following steps are followed to estimate the static enthalpy loss for the nine cases considered in Section 4-4-1.
Step 1: Import the *flow.dat* file to Tecplot 360 2008.
Step 2: Load the equation file: *equation_2008.eqn*.
Step 3: Transform the coordinates from rectangular to polar and plot the contours in the $\theta - R$ plane.
Step 4: Extract the flow properties along two lines at the inlet and three lines at the exit shown in Figure F-1.
Step 5: Run the *readtecplotfile.m* to obtain the value of the static enthalpy loss.
Step 6: Repeat this procedure for each case to obtain the static enthalpy loss.

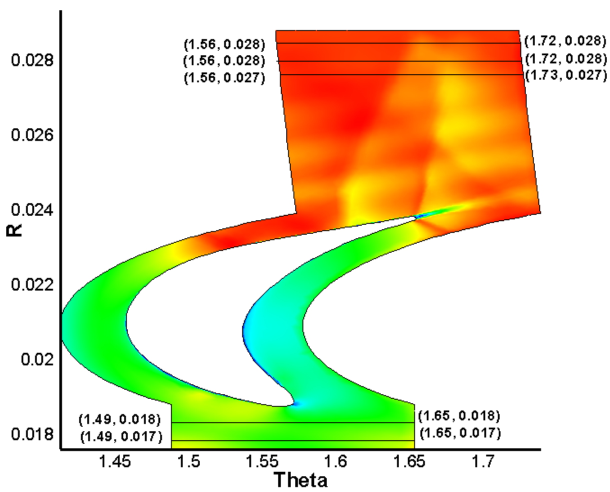

Figure F-1: Coordinates of line along which properties are extracted to estimate the static enthalpy loss.

Bibliography

[1] A. J. Head, C. De Servi, E. Casati, and P. Colonna, "Design specifications and requirements of the ORCHID set-up," tech. rep., Delft University of Technology, 2015.

[2] J. D. Anderson, *Modern Compressible flow - With historical perspective*. McGraw-Hill, 2004.

[3] M. J. Zucrow and J. D. Hoffman, *Gas Dynamics - Multidimensional Flow*, vol. 2. John Wiley and Sons, 1977.

[4] M. J. Zucrow and J. D. Hoffman, *Gas Dynamics*, vol. 1. John Wiley and Sons, 1977.

[5] A. Javed, *Developing Generic Design Expertise for Gas Turbine Engines: Robust Design of a Micro Centrifugal Compressor*. PhD thesis, Delft University of Technology, 2014.

[6] J. C. Helton and F. J. Davis, "Latin hypercube sampling and the propagation of uncertainty in analyses of complex systems," *Reliability Engineering and System Safety*, vol. 81, pp. 23–69, 2003.

[7] E. Casati, S. Vitale, M. Pini, G. Persico, and P. Colonna, "Centrifugal turbines for mini-organic rankine cycle power systems," *Journal of Engineering for Gas Turbines and Power*, vol. 136, p. 122607, 2014.

[8] T. van der Stelt, N. R. Nannan, and P. Colonna, "The iPRSV equation of state," *Fluid Phase Equilibria*, vol. 330, pp. 24–35, 2012.

[9] P. Cinnella, C. P.M, L. Parussini, and V. Pediroda, "Quantification of uncertainties in compressible flows with complex thermodynamic behavior," in *39th AIAA Fluid Dynamic Conference*, 2009.

[10] J. A. S. Witteveen and H. Bijl, "A monomial chaos approach for efficient uncertainty quantification in nonlinear problems," *SIAM Journal on Scientific Computing*, vol. 30, no. 3, pp. 1296–1317, 2008.

[11] S. Vitale, M. Pini, A. Ghidoni, and P. Colonna, “Fluid dynamic design and analysis of a highly loaded centrifugal rotor for mini orc power systems,” *3rd International Seminar on ORC Power Systems*, vol. 125, pp. 1–11, 2015.

[12] S. J. Hercus and P. Cinnella, “Robust shape optimization of uncertain dense gas flows through a plane turbine cascade,” in *ASME-JSME-KSME 2011 Joint Fluids Engineering Conference*, pp. 1739–1749, American Society of Mechanical Engineers, 2011.

[13] G. Gori, A. Guardone, S. Vitale, A. J. Head, M. Pini, and P. Colonna, “Non-ideal compressible-fluid dynamics simulation with su2: Numerical assessment of nozzle and blade flows for organic rankine cycle applications,” in *3rd International Seminar on ORC Power Systems*, pp. 1–11, American Society of Mechanical Engineers, 2015.

[14] A. J. Head and W. P. J. Visser, “Scaling 3-36kw microturbines,” in *ASME Turbo Expo 2012: Turbine Technical Conference and Exposition*, pp. 609–617, American Society of Mechanical Engineers, 2012.

[15] A. Guardone, A. Spinelli, and V. Dossena, “Influence of molecular complexity on nozzle design for an organic vapor wind tunnel,” *Journal of Engineering for Gas Turbines and Power*, vol. 135, p. 042307, 2013.

[16] P. Colonna and T. van der Stelt, “FluidProp: a program for the estimation of thermo physical properties of fluids,” tech. rep., Energy Technology Section, Delft University of Technology, The Netherlands, 2004.

[17] B. M. Adams, M. S. Ebeida, M. S. Eldred, J. D. Jakeman, L. P. Swiler, J. A. Stephens, D. M. Vigil, T. M. Wildey, W. J. Bohnhoff, K. R. Dalbey, J. P. Eddy, K. T. Hu, L. E. Bauman, and P. D. Hough, “DAKOTA, a multilevel parallel object-oriented framework for design optimization, parameter estimation, uncertainty quantification, and sensitivity analysis: Version 6.0 user’s manual,” tech. rep., Sandia Technical Report SAND2014-4633, 2014.

[18] P. Colonna, S. Rebay, J. Harinck, and A. Guardone, “Real-gas effects in orc turbine flow simulations: influence of thermodynamic models on flow fields and performance parameters,” in *ECCOMAS CFD 2006: Proceedings of the European Conference on Computational Fluid Dynamics, Egmond aan Zee, The Netherlands, September 5-8, 2006*, Delft University of Technology; European Community on Computational Methods in Applied Sciences (ECCOMAS), 2006.

[19] P. Colonna, N. R. Nannan, A. Guardone, and E. W. Lemmon, “Multiparameter equations of state for selected siloxanes,” *Fluid Phase Equilibria*, vol. 244, pp. 193–211, 2006.

[20] G. Persico, M. Pini, V. Dossena, and P. Gaetani, “Aerodynamics of centrifugal turbine cascades,” vol. 137, p. 122602, American Society of Mechanical Engineers, 2015.

[21] G. Soave, “Equilibrium constants for a modified redlich-kwong equation of state,” *Chemical Engineering Science*, vol. 27, pp. 1197–1203, 1972.

[22] B. E. Poling, J. M. Prausnitz, and J. P. O’Connell, *The Properties of Gases and Liquids*. McGraw Hill Inc., 2001.

[23] A. J. Head, C. De Servi, E. Casati, and P. Colonna, “Design specifications for the Organic Rankine Cycle Hybrid Integrated Device ORCHID facility for dense gas experiments,” tech. rep., Delft University of Technology, 2015.

[24] J. C. Helton, J. D. Johnson, C. J. Sallaberry, and C. B. Storlie, “Survey of sampling-based methods for uncertainty and senstivity analysis,” *Reliability Engineering and System Safety*, vol. 91, pp. 1175–1209, 2006.

[25] M. Pini and P. Cinnella, “Hybrid adjoint-based robust optimization approach for fluid-dynamic problems,” *15th AIAA Non-Deterministic Approaches Conference*, p. 16, 2012.

[26] J. C. Helton and F. J. Davis, *Sampling-based methods for uncertainty and sensitivity analysis.* Sandia National Laboratories Albuquerque, 2000.

[27] I. A. McLure and E. Dickinson, “Vapour pressure of hexamethyldisiloxane near its critical point: corresponding-states principle for dimethylsiloxanes,” *Journal of Chemical Thermodynamics*, vol. 8, pp. 93–95, 1976.

[28] N. R. Nannan, P. Colonna, C. M. Tracy, R. L. Rowley, and J. J. Hurly, “Ideal-gas heat capacities of dimethylsiloxanes from speed-of-sound measurements and ab initio calculations,” *Fluid Phase Equilibria*, vol. 227, pp. 102–113, 2007.

[29] R. Rowley, W. Wilding, J. Oscarson, Y. Yang, N. Zundel, T. Daubert, and R. Danner, *DIPPR Data compilation of pure chemical properties.* Design Institute for Physical Properties, AIChE, New York, NY, 2004.

[30] C. B. Moler, *Numerical Computing with MATLAB.* Society of Industrial and Applied Mathematics, 2004.

[31] T. Chew, “Design of small-scale shockwave generators for the ORCHID setup,” Master’s thesis, The University of Queensland, Australia, 2015.

[32] F. Palacios, M. R. Colonno, A. C. Aranake, A. Campos, S. R. Copeland, T. D. Economon, A. K. Lonkar, T. W. Lukaczyk, T. W. R. Taylor, and J. J. Alonso, “Stanford University Unstructured (SU^2) : An open-source integrated computational environment for multi-physics simulation and design,” American Institute of Aeronautics and Astronautics, 2013.

[33] A. Ghidoni, “3D anisotropic hybrid grid generation for complex aerospace applications,” tech. rep., Department of Mechanical and Industrial Engineering, University of Brescia, 2014.

[34] M. Hunt, “Mach reflections,” Master’s thesis, University of Manchester, United Kingdom, 2008.

[35] N. J. Mourtos, “Oblique shocks.”

[36] S. L. Dixon, *Fluid Mechanics and Thermodynamics of Turbomachinery.* Elsevier Butterworth-Heinemann, 5 ed., 2005.

[37] M. Pini, G. Persico, E. Casati, and V. Dossena, “Preliminary design of a centrifugal turbine for Organic Rankine Cycle applications,” *Journal of Engineering for Gas Turbines and Power*, vol. 135, p. 042312, 2013.

[38] J. Hoffren, T. Talonpoika, J. Larjola, and T. Siikonen, "Numerical simulation of real-gas flow in a supersonic turbine nozzle ring," *Journal of engineering for gas turbines and power*, vol. 124, no. 2, pp. 395–403, 2002.

[39] A. Whitfield and N. C. Baines, *Design of Radial Turbomachines.* Longman Scientific & Technical, 1990.

[40] Z. Wu, Y. Xu, W. Wang, and R. Hu, "Review of shock wave detection method in cfd post-processing," *Chinese Journal of Aeronautics*, vol. 26, no. 3, pp. 501–513, 2013.

[41] H. K. Versteeg and W. Malalasekera, *An introduction to computational fluid dynamics: the finite volume method.* Pearson Education, 2007.

[42] B. Grossman, "Fundamental concepts of real gasdynamics," tech. rep., Virginaia Polytechnic Institute and State University, 2000.